Surface finishing of Ti6Al4V implants produced by laser powder bed fusion

Moses Mhlanga

Dissertation submitted in fulfilment of the requirements for the degree

MASTER of ENGINEERING in MECHANICAL ENGINEERING

in the Department of Mechanical and Mechatronics Engineering, Faculty of Engineering, Built Environment and Information Technology at Central University of Technology, Free State

Supervisor:	**Prof. Ihar Yadroitsau**
Co-supervisors:	**Prof. Ina Yadroitsava**
	Mr. L.R. Masheane

Bloemfontein

Declaration of independent work

I, Moses Mhlanga, identity number _____________ and student number __________, do hereby declare that this research project submitted to Central University of Technology, Free State, for the Master of Engineering in Mechanical Engineering degree, is my own independent work; and complies with the Code of Academic Integrity, as well as other relevant policies, procedures, rules, and regulations of Central University of Technology, Free State; and has not been submitted previously to any institution by myself or any other person in fulfilment of the requirements for the attainment of any qualification.

	07/04/2025
Signature of student	**Date**

Acknowledgements

First and foremost, I would like to give thanks to God, the ultimate source of wisdom, for his guidance throughout this research.

I am sincerely thankful to my supervisors at Central University of Technology, Prof. Ihar Yadroitsau (Igor Yadroitsev), Prof. Ina Yadroitsava, and Mr. Lebogang Masheane for their steadfast support, patient mentorship, and invaluable assistance during my academic journey. I will always be deeply grateful for their contributions.

I extend my profound thanks to Dr. Dean Kouprianoff from CRPM for your consistent support throughout this study. Most importantly his readiness to assist whenever I faced challenges was invaluable. May you continue to be blessed.

I am grateful to Dr. Gerrit Ter Haar of the University of Stellenbosch for his help with the equipment and materials needed for chemical polishing. I truly appreciate his support in this research. May blessings be upon you.

I also want to acknowledge the love and encouragement I received from the Zitha and Mhlanga families which encompasses the elders, brothers, sisters, nephews and others I will always be indebted to you.

I would like to express my gratitude to the Centre for Rapid Prototyping and Manufacturing for the machining and resources provided during this study.

I gratefully acknowledge the South African Research Chairs Initiative of the National Research Foundation of South Africa (Grant № 97994) and the Collaborative Program in Additive Manufacturing (Contract № CSIR-NLC-CPAM-21-MOA-CUT-03) of the Department of Science and Innovation for the financial aid received.

Abstract

The surface roughness of samples produced by laser powder bed fusion (L-PBF) heat-treated Ti6Al4V ELI for medical implants is described in this study taking into account the samples' location on the build plate. Three different shapes of samples were used, namely horizontal, vertical, and semisphere samples. The surface roughness of the samples in an as-built state, after they were polished by dry electropolishing only and after the combination of dry electropolishing and chemical polishing in HF-HNO_3 solutions, were analyzed. Scanning electron microscopy and a profilometer were used to examine the surface roughness of horizontal, vertical, and semisphere samples. The morphological features of the surfaces are displayed both before and after surface finishing. Top surfaces are formed by overlapped tracks and stripes since single layers are manufactured in a track-by-track manner in stripes, while 3D objects as a whole are made layer-by-layer in L-PBF, and side surfaces are defined by layers. It was demonstrated that while the top and side surfaces of the vertical and horizontal samples had different origins, their roughness values measured by the profilometer were generally similar because the measured roughness was primarily determined by the powder particles sticking to both the samples' upper and side surfaces. The samples with the highest surface roughness were those located farthest from the argon (Ar) input and recoater starting line. The roughness of the semisphere samples is generally similar in all the zones since their roughness is linked to the staircases, powder material sticking, and ripples. After the analysis of the as-built samples, it was concluded that Ti6Al4V medical implant samples produced by L-PBF require post-processing to meet the surface finish expected for medical implants. The 60, 90, and 120 minutes of dry electropolishing made L-PBF surfaces smoother but did not meet international standards for medical implants. A longer time of dry electropolishing and chemical polishing in HF-HNO_3 solution allows the achievement of surface roughness (Ra) of less than 5 μm, but the weight loss increases, which can influence the L-PBF implant dimensions and shape.

Keywords: laser powder bed fusion, medical implants, Ti6Al4V, surface roughness, surface finishing

Table of contents

List of tables

List of figures

Glossary

2D	Two-dimensional
3D	Three-dimensional
AM	Additive manufacturing
BCC	Body-centred cubic
CAD	Computer-aided design
CRPM	Centre of Rapid Prototyping and Manufacturing
CUT	Central University of Technology, Free State
DMLS	Direct metal laser sintering
EBM	Electron beam melting
EDM	Electrical discharge machine
ELI	Extra-low interstitial
EOS	Electro Optical Systems
HCP	Hexagonal close-packed
L-PBF	Laser powder bed fusion
SEM	Scanning electron microscope
SLM	Selective laser melting
UTS	Ultimate tensile strength
YS	Yield strength

CHAPTER 1: INTRODUCTION

1.1. Background

Traditional manufacturing is limited when it comes to creating complex components; however, the objects that are impossible to create using other processes of manufacturing can be produced by additive manufacturing (AM). Laser powder bed fusion (L-PBF) is a technology that produces parts track-by-track and layer-by-layer, where powder is delivered in a thin layer. The powder layer is fused by a laser beam that scans across the powder bed surface. Another thin layer of powder is delivered over the solidified material, and the powder is scanned by the laser beam. The operation is replicated until the required three-dimensional (3D) object is formed. This technology provides an opportunity to create parts with complex shapes and internal features, parts with functional gradients, lattice, and cellular structures directly from digital data.

High residual stress and a specific anisotropic microstructure in L-PBF parts necessitate post-heat treatment, which causes microstructures and mechanical properties to change.

Medical implant surfaces are connected to the human body tissues and specific requirements for the surface quality must considered. Before an implant is placed in a human body, specific surface quality requirements must be met depending on the part of the body where the implant is placed. A further consideration is the material used to manufacture the implant.

Biomaterials are types of material that can be used to replace body tissues. Properties such as corrosion resistance, biocompatibility, non-toxicity and excellent tribological properties must be considered when the choice of biomaterial to be used for implant is made. The most commonly used biomaterial for bone replacement is a titanium alloy (Ti6Al4V) due to its excellent properties such as low density compared to stainless steel (316L) and cobalt chromium (Co–Cr) alloys, enhanced biocompatibility and corrosion resistance.

Regardless of the attractive benefits offered by the L-PBF process, the surface quality of the L-PBF parts is poor and is of concern where good surface quality is required. If this challenge can be resolved, the L-PBF process will be more readily acceptable.

In recent decades much research has been conducted to find suitable methods for surface finishing of Ti6Al4V implants produced by L-PBF. Methods to improve the structure of surface roughness include passivation, anodization, ion implantation, blasting, chemical etching, hydroxyapatite coating, laser etching, micro-arc oxidation, nano-titania coatings, porous surfaces, ion-sputtering coating, anodized surface, and HA coating. The studies have validated that roughness of 0,5 to 2 μm on the surface of a titanium implant can accelerate the osseointegration rate (Wang *et al.*, 2020). However, these methods have their limitations. Studies have confirmed that the roughness on the surface of an implant has a significant effect on the fixation quality with a bone and osseointegration rate, as well as the health of the soft tissues (Wang *et al.*, 2020).

1.2. Problem statement

Despite the many advantages of Laser Powder Bed Fusion (L-PBF) including the ability to produce complex geometries and customized components directly from digital models, the surface quality of L-PBF-fabricated parts remains a significant limitation. The rough and irregular surfaces generated during the L-PBF process are particularly concerning for applications where high surface quality is critical, such as biomedical implants, aerospace components and precision engineering parts. Poor surface finish can negatively impact mechanical performance, fatigue resistance, and, in the case of implants, biological integration with tissues.

Therefore, improving the surface quality of L-PBF parts is essential to fully exploit the potential of this additive manufacturing technology. Addressing this challenge will enhance the reliability, functional performance, and broader industrial acceptance of L-PBF-fabricated components, particularly in applications where surface quality is critical.

1.3. Aim of the study

The main aim of this study is to evaluate the surface roughness of as-built Ti6Al4V samples produced by L-PBF with regard to their positioning on the base plate and after surface finishing by dry electropolishing only, as well as when followed by chemical polishing, with the focus on medical implants.

1.4. Thesis statement

This study assesses the surface roughness of the as-built Ti6Al4V samples produced by L-PBF with regard to their positioning on the base plate and the techniques of polishing their surfaces. The outcomes of the techniques used to achieve the required surface finishing for Ti6Al4V samples are defined.

1.5. Objectives of the study

- To study various types of conventional Ti6Al4V implants and requirements for surface quality and surface texturization.
- To study/perform methods of surface finishing on Ti6Al4V samples build by L-PBF technology.
- To analyze the quality or roughness of the Ti6Al4V samples built by L-PBF technology (as-built and after surface finishing).

1.6. Research methodology

A five-phase approach will be adopted for this project.

Phase 1: Study the L-PBF process, design of experiments, and Ti6Al4V samples.

Phase 2: Manufacturing of L-PBF samples and their characterization. The samples will be manufactured using an EOSINT M290 machine and Ti6Al4V ELI powder, followed by heat treatment.

Phase 3: Quantitative and qualitative surface roughness of as-built samples using Mitutoyo SJ210 and scanning electron microscope (SEM). The quantitative surface roughness of the as-built Ti6Al4V samples will be measured using Mitutoyo Surftest

SJ210, and the qualitative surface roughness of the as-built samples will be analyzed using SEM.

Phase 4: Surface finishing of Ti6Al4V samples. The as-built Ti6Al4V samples will go through surface finishing using dry electropolishing followed by chemical polishing in HF-HNO_3 solution, and results of the modified surfaces and their textures will be analysed.

Phase 5: The conclusion and recommendation will be made regarding the textures after dry electropolishing and chemical polishing of Ti6Al4V and their effects on surface topology.

1.7. Expected outcomes

- Defined surface quality of Ti6Al4V produced by L-PBF technology.
- Defined methods to improve the surface quality of Ti6Al4V parts produced by L-PBF technology.

1.8. Dissertation outline

The first chapter introduces the study and presents the context and motivation, published work, purpose, and goals.

The literature review is presented in the second chapter, beginning with AM, its principles, process parameters, process peculiarities of L-PBF, and the surface roughness of L-PBF parts. Investigations are conducted into the Ti6Al4V biomaterial, mechanical properties and microstructure, residual stress relief, existing surface finishing techniques, and various implant surface quality requirements.

In the third chapter, materials and methods are discussed. The material, methods, tools, and machinery used in this dissertation are presented. The design of the experiment, the samples to be manufactured, post-heat treatment, and the set-up of the investigation are set out.

The fourth chapter analyzes the results obtained in this study. The results and discussion of surface roughness of the as-built and surface-finished Ti6Al4V samples produced by L-PBF are presented as are the quantitative and qualitative results. The as-built surface roughness results, the dry electropolishing results, and the combination of dry electropolishing and chemical polishing in HF and HNO_3 solutions results are presented and discussed in this chapter.

Chapter five describes the outcomes of the study.

The references and Appendices are presented as follows: Appendix 1: Surface roughness parameters, Appendix 2: Surface finishing methods, and Appendix 3: Surface roughness data.

1.9. Publications and presentations

- M. Mhlanga, L. R. Masheane, I. Yadroitsava, and I. Yadroitsev, 2022 Surface roughness of Ti6Al4V samples produced by laser powder bed fusion for bone implants, RAPDASA-RobMech-PRASA-CoSAAMI Conference – Digital Technology in Product Development – The 23rd Annual International RAPDASA Conference joined by RobMech, PRASA and CoSAAMI, MATEC Web Conf., 2022 vol. 370, p. 11001, doi: 10.1051/matecconf/202237011001
- M. Mhlanga, L. R. Masheane, I. Yadroitsava, and I. Yadroitsev, 2024 RAPDASA-RobMech-PRASA-AMI Conference: Unlocking Advanced Manufacturing – The 25th Annual International RAPDASA Conference, joined by RobMech, PRASA and AMI, hosted by Stellenbosch University and Nelson Mandela University, 406, 2024 Vol 406, doi: /10.1051/matecconf/202440609003
- M.Mhlanga, L.R. Masheane, I.Yadroitsava, G. M. Ter Haar, D. Kouprianoff, I. Yadroitsev. Surface finishing of L-PBF Ti6Al4V ELI samples for biomedical applications by dry electro- and chemical polishing. *Extended abstract was submitted to 26th Annual International Conference from 27-30 October 2025 at the CSIR International Convention Centre in Pretoria, South Africa.*

CHAPTER 2: LITERATURE REVIEW

2.1. Introduction

AM is a production method that constructs components incrementally from a three-dimensional computer-aided design (3D-CAD) model in contrast to traditional techniques that involve subtracting material through multiple stages (Collan *et al.,* 2020). AM is a technology that enables the simultaneous production of various distinct and intricately interconnected components that would traditionally be made by joining parts in a conventional manufacturing process. (Ahuja *et al*., 2015). This method offers significant flexibility allowing for the creation of complex geometries that traditional manufacturing techniques cannot achieve, thus making AM a preferred option for production (Rouf *et al.*, 2022). Other advantages of AM also include the flexibility of the system, the short time required for the product to be designed and manufactured, the ability to incorporate design features that would be difficult to achieve through conventional means, and the ability to create new alloys (Mehrpouya *et al.*, 2021). It also enables the production of intricate metal parts, thus enabling the development of special products like biomedical implants (Davoodi *et al.*, 2022). AM is also characterized by reduced waste of material in the process of manufacturing (Javaid *et al.*, 2021).

The PBF process employs either an electron (E-PBF) or a laser beam (L-PBF) as a source of heat to melt the metal powder stack to form metallic objects that have the mechanical properties of wrought materials. However, one of the limitations of the L-PBF process is its surface quality, which creates a problem for end users even though there are many advantages and benefits of using the technique (Zhang *et al.*, 2017). If this limitation is overcome, then L-PBF will be more attractive to industries that are concerned with the quality of surface.

2.2. Principles of L-PBF

In L-PBF, also known as Selective Laser Melting (SLM), Direct Metal Laser Sintering (DMLS), Laser Cusing, and Direct Metal Laser Melting, the powder bed is fused by a laser beam. A focused laser beam scans an operational plane on a powder bed based on CAD information (Trevisan *et al*., 2018) (Lee *et al*., 2020). As shown in Figure 1, the first step in this technique is to create a 3D solid model from CAD. Subsequently, the model is split into two-dimensional sections (3D STL model and 2D slice model) and sent to the AM machine. Inside the AM machine, the powder layer is deposited on the building platform, followed by a focused laser beam melting the powder according to a predetermined geometry, the melt rapidly solidifies, and the first layer is generated. To generate a layer, a complete transformation of phase occurs, causing solid particles of powder to become liquid before cooling/solidifying. The laser beam energy is sufficient to melt a portion of the previously solidified solid structure; thus, this method of complete melting is effective for producing compact, well-bonded structures (Washington *et al.*, 2018), (Abd-Elaziem *et al.*, 2022). After melting and solidification, the building platform is lowered, and the process is repeated. Another powder layer is deposited on the solidified layer, and this process repeats until the predetermined geometry or final product is complete (Subhedar, 2018). The manufacturing process takes place in a compartment containing a protective gas (nitrogen or argon) to avoid oxidation at extreme temperatures and to prevent spattering (Depboylu *et al.*, 2022). Rapid melting and cooling create fine microstructures, enhancing mechanical properties (Han *et al.*, 2023). Residual stresses can develop due to rapid cooling, requiring post-processing heat treatments (Ponnusamy *et al.*, 2021).

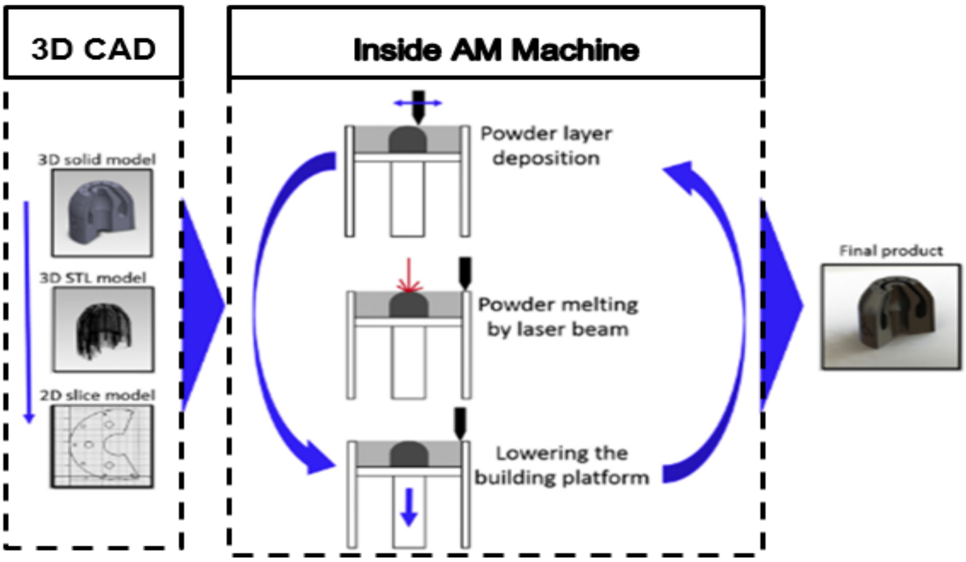

Figure 1: L-PBF process (Mäkinen et al., 2015)

2.3. Parameters governing the L-PBF process

The process parameters of L-PBF technology can be divided into three categories: 1) machine-based, 2) material-based, and 3) process-input parameters, as shown in Figure 2.

- Machine-based input parameters – these parameters have to do with the specifications of the machine equipment (laser wavelength, processing atmosphere, etc.).
- Material-based input parameters – these parameters exist due to the nature and the properties of the material used.
- Process-based input parameters – these are the parameters that are specified by the operator to obtain the required part quality.

The most influential L-PBF parameters are laser power, scanning speed, the thickness of the layer, and hatch distance, as depicted in Figure 3. These parameters are most significant since they have the potential to affect the as-built parts' quality, mechanical characteristics, and functionality of L-PBF products *(*Yadroitsev *et al., 2007*). To produce a fully dense material, the usual approach in L-PBF involves utilizing the correct combination of the aforementioned essential process parameters. To achieve the intended part characteristics, it is essential to tune and optimize these interconnected parameters to ensure accuracy, surface finish, and mechanical strength (Paraschiv *et al.*, 2022).

Laser power: The power of the laser beam is an important factor that determines the energy that is transferred to the powder bed with a view to melting the material. Changes in laser power can affect the surface smoothness of the components. Elevated laser power levels often result in smoother surfaces due to the melting and joining of powder particles. Conversely, excessive energy can cause surface imperfections, including roughness, spattering, and balling (Hao *et al.*, 2023).

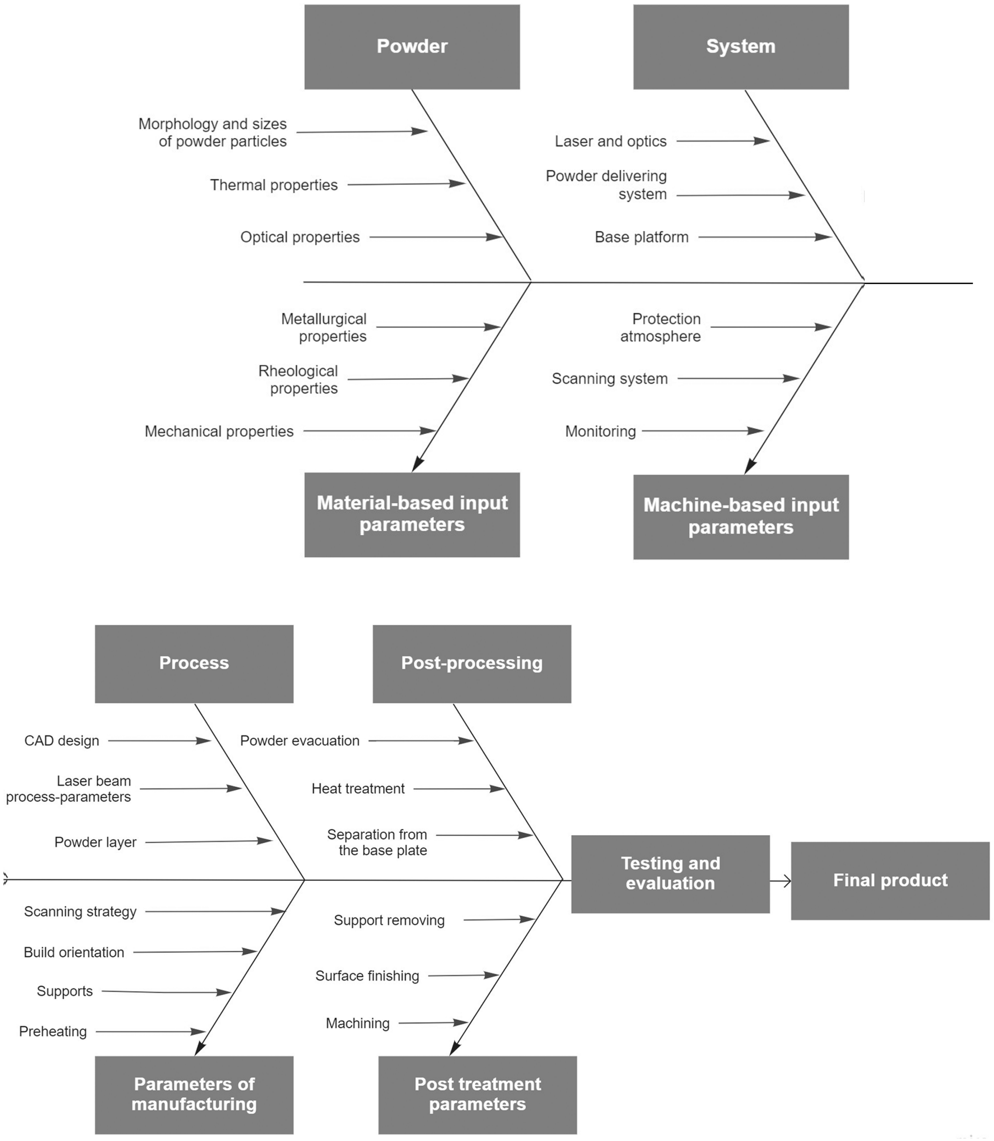

Figure 2: Influencing factors on the L-PBF quality (Yadroitsev et al., 2021)

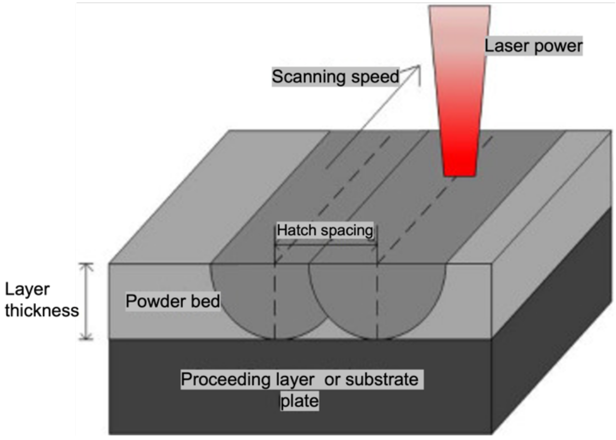

Figure 3: L-PBF process parameters (Chowdhury *et al.*, 2022)

Scanning speed: The rate at which the laser beam moves across the powder bed significantly affects the smoothness of the surface of the finished parts. In general, slow scanning speeds are preferable since they enable the powder particles to fuse and bond well. On the other hand, higher scanning speeds may lead to rough surfaces or defects such as porosity and spattering due to the inability of the powder to melt completely (Islam *et al.*, 2024).

Layer thickness: The thickness of each layer deposited in the course of the L-PBF process is another criterion of interest. The layer thickness deposited also affects the accuracy and smoothness of the produced parts. In general, using thin layers enhances feature resolution and surface finish since it provides accurate geometric representation. However, if the layers are too thin, the processing time will be prolonged and result in increased cost of manufacturing (Goulas *et al.*, 2016).

Hatch spacing: The spacing between the laser scan paths determines the quality of the manufactured parts. Close hatch spacing results in better surfaces since there is proper bonding and melting of the powder particles. On the other hand, wider hatch spacing can lead to poor surfaces since there is a lack of energy to ensure that the powder is fully melted (Elaziem *et al.*, 2022).

The general approach to fabricating a high-quality product is a multi-iteration process. According to Yadroitsev *et al.*, (2014), an algorithm that follows the recommended hierarchical design principles shown in Figure 4 may be used to describe the parameters for high-quality 3D models.

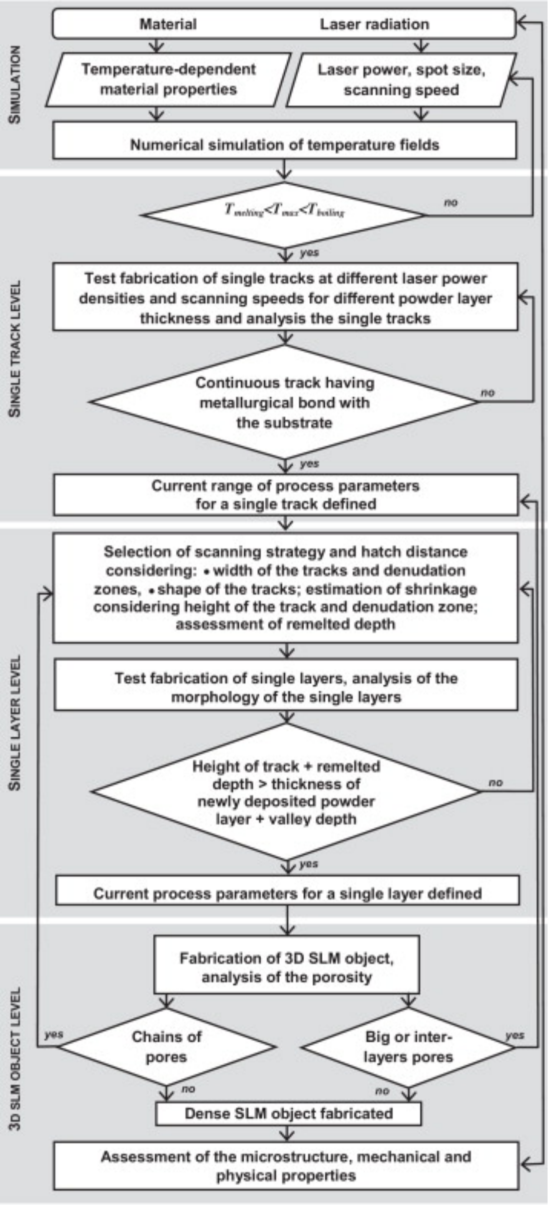

Figure 4: Algorithm for finding the optimal L-PBF process parameter (Yadroitsev et al., 2014)

2.4. Peculiarities of L-PBF manufacturing

L-PBF is a method that uses layers to create objects, where objects are created by laying down successive layers of metal powder. A laser is used in the creation of objects to bond layers of metal powder on the build plate in order to obtain the cross-section of the given object (Khairallah *et al.*, 2016).

The operation of the laser is meticulously controlled to ensure adequate melting of the powder forming the desired part geometry (DebRoy *et al.*, 2018).

The metallic powder used in L-PBF serves dual purposes in the manufacturing process: it acts both as a material for the final product and as a support structure. Furthermore, the powder bed aids in dispersing heat throughout the laser melting process (Rausch *et al.*, 2017).

Various metal alloys, such as titanium, aluminium, stainless steel, and nickel-based alloys, can be used in the L-PBF process. The characteristics of these materials, like the size and shape of the powder particles and its flowability, also affects the printing process as well as the quality of the printed product (Agarwal *et al.*, 2021).

In order to protect the process, gases such as argon (Ar), nitrogen (N2), and helium (He) are commonly employed. This gaseous environment helps restrain the appearance of metal vapours on the surface of the molten pool, which in turn, minimizes spattering (Guo *et al.*, 2018).

2.5. Surface roughness of L-PBF objects

2.5.1. Influence of L-PBF process parameters on surface roughness

The surface finish of an L-PBF part is a result of several process parameters, including laser power, scanning speed, layer thickness, scanning strategies and construction strategies (Martucci *et al*., 2023). By meticulously managing these parameters, manufacturers can improve the surface texture and attain the desired smoothness in L-PBF components (Ahmed *et al.*, 2022). Additional studies have explored specific process-related factors such as the impact of shielding gas flow (Masiagutova *et al.*, 2021).

There are varied findings in the research, with some studies showing that increasing laser scan speed results in increased surface defects (Erinosho *et al*., 2019), while other studies show the converse (Artzt *et al.*, 2020). However, it has been suggested that using smaller powder particles can produce better surface finishes (Balbaa *et al.*, 2021) while this claim is refuted by some researchers (Spierings *et al*., 2010).

Research by Nicolas-Silvente *et al.*, (2020) shows that the design and orientation of the parts to be built affect the surface texture. Changes in laser power, scanning speed, hatch distance, and powder layer thickness can increase energy density and thus lead to improved surface quality. However, it is noted that when certain parameters are exceeded, the surface quality is severely compromised. These findings highlight the fact that to achieve a high-quality finish, various factors need to be well-tuned, as all these factors are interrelated, and they affect multiple characteristics at the same time. This is a concept that is not far-fetched from the idea of Pandora's box, as surface roughness cannot be reduced to the minimum without affecting another significant characteristic. Table 1 show the influence of L-PBF process parameters on surface roughness.

Table 1: Influence of L-PBF process parameter on surface roughness

Process parameter	**Effect on surface roughness and surface quality**	**References**
Laser power (W)	Higher power improves fusion, but excessive power increases spatter and roughness. Reduced power results in poor melting, increasing porosity and rough surfaces.	(Taghian *et al.*, 2023)
Scan speed (mm/s)	High speed can cause incomplete melting, leading to rough, porous surfaces. Low speed results in overheating, causing balling effects and increased roughness.	(Wang *et al.*, 2023)
Layer thickness (µm)	Thicker layers (~50 µm) lead to increased staircase effect, worsening roughness. Thinner layers (~20 µm) improve surface finish but increase build time.	(Cutolo *et al.*, 2018)
Hatch spacing (µm)	Wide spacing (~120 µm) reduces density, increasing roughness. Narrow spacing (~80 µm) improves fusion, but may lead to excessive heat accumulation.	(Shrestha *et al.*, 2022)
Spot size/beam diameter (µm)	Smaller spot sizes (~50 µm) improve resolution and surface finish. Larger spot sizes (~100 µm) increase surface waviness.	(Amann *et al.*, 2024)
Build orientation	Horizontal (0°) surfaces generally have better roughness than vertical ones. Vertical (90°) orientations show higher roughness due to the staircase effect. An inclination of 45° minimizes roughness by balancing layer deposition.	(Torino, 2024) (M. Shange *et al.*, 2019)
Powder particle size (µm)	Smaller powder particle sizes (~15 µm) result in smoother surfaces. Larger powder particle sizes (~45 µm) increase surface roughness.	(Yánez *et al.*, 2022)
Recoating speed (mm/s)	Slower recoating speeds (~80 mm/s) ensure better powder distribution, improving surface quality. Faster speeds (~200 mm/s) may lead to uneven layers and increased roughness.	(Le *et al.*, 2021)

The quality and surface finish of Ti6Al4V parts produced by L-PBF can be improved by optimizing the process parameters (Tian *et al.*, 2024)**.** Table 2 is a summary of the optimum process parameters for producing high-quality implants with low surface roughness, good mechanical properties, and excellent biocompatibility**.**

Table 2: Optimum process parameter for Ti6Al4V parts in L-PBF

Process parameter	**Optimal range for Implants**	**Effect on implant quality**	**References**
Laser power	150–400 W	Higher power improves fusion, but excessive power increases roughness.	(Majumdar et al., 2019)
Scan speed	600–1200 mm/s	Optimized speed ensures uniform melting and prevents defects.	(Gaur et al., 2022)
Layer thickness	20–50 µm	Thinner layers result in smoother surfaces, while thicker layers reduce printing time but increase roughness.	(Majumdar et al., 2019)
Hatch spacing	80–120 µm	Controls density and surface roughness, while smaller spacing improves finish but increases the build time.	(Dong et al., 2018)
Spot size/Beam diameter	50–100 µm	Smaller spot sizes provide higher resolution, improving surface detail.	(Yildiz et al., 2024)
Build orientation	45° to 90° inclination	Angled builds reduce staircase effects and improve mechanical performance.	(Spierings et al, 2010)
Powder particle size	15–75 µm	Smaller particle size improves surface smoothness and density.	(Majumdar et al., 2019)
Recoating speed	80–200 mm/s	Affects powder distribution; slower speeds improve uniformity but increase build time.	(Le et al., 2021)

2.5.2. Powder material

The building platform is covered with a layer of metal powder. In L-PBF, the powder is fused and melted by a high-power laser based on the shape of the object's cross-section. The laser heats up the powder particles to their melting point where they weld together. When the laser traces the shape, the metal melts, and then it solidifies quickly to form a layer of the object. This process is reiterated with the help of layering and subsequent melting of powder until the construction of the object is complete (Rahmani *et al*., 2023).

In L-PBF, it is common for some of the metal powder grains to only partially melt during laser exposure. This can happen due to various factors, such as uneven energy distribution, insufficient energy input, or rapid cooling (Chowdhury *et al.*, 2022). These partially melted grains can stick to the surface of the solidified component, which results in what is called "partially melted particles", as shown in Figure 5. This level of poor fusion of these partially molten particles can lead to defects such as porosity, lack of fusion, and a poor surface finish, hence affecting the quality and performance of the produced part (Pegues *et al.*, 2018).

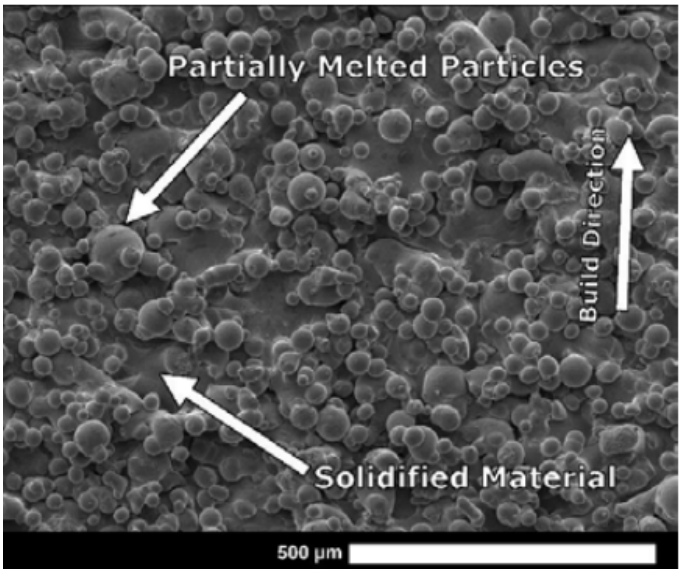

Figure 5: Partially melted powder particles (Fox et al., 2016)

2.5.3. Track-by-track manufacturing

Two adjacent melt tracks have to interact to make a smooth surface. If the distance between the tracks is set wider than required, it leads to the development of gaps, which in turn causes the surface to become uneven with ridges or valleys. Conversely, if the tracks overlap excessively, it may cause the previously solidified material to remelt too much, resulting in surface peaks and valleys from the buildup of material (Feng *et al.*, 2024).

2.5.4. Building orientation

The surface roughness of parts produced in a vertical orientation L-PBF is generally rougher compared to other orientations, largely due to the staircase effect and thermal gradients that occur during the printing process (DebRoy *et al.*, 2018). Table 3 show how vertically oriented parts affect surface roughness in L-PBF parts.

Table 3: Effect of surface roughness on vertically oriented parts

Factor	**Description**	**Effect on surface roughness**	**References**
Staircase effect (Z-axis effect)	Vertical orientation causes a staircase effect, where each printed layer has a visible edge or step.	The surface is rougher due to layer-by-layer deposition and visible steps.	(Kónya et al., 2023)
Thermal gradients	Vertical parts experience greater thermal gradients due to the longer distance between the build plate and the top layers.	This leads to uneven cooling which can cause distortion and surface roughness.	(Vrancken et al., 2012)
Layer bonding	As layers build up vertically, the bonding between layers may result in visible seams or layer lines.	Inconsistent bonding can increase roughness especially if laser parameters or speed are not optimized.	(Ngo et al., 2018)

The surface roughness of horizontal parts produced by L-PBF is generally influenced by several factors, including layer height**,** laser power**,** scan speed, and material type**.** In horizontal orientation, parts often achieve a smoother surface compared to other orientations due to better thermal management and less pronounced staircase effects**.** However, some roughness may still remain depending on process parameters and material (Alfieri *et al*., 2022). Table 4 show how vertically oriented parts affect surface roughness in L-PBF parts.

Table 4: Effect of surface roughness on horizontally oriented parts

Factor	**Effect on surface roughness**	**References**
Layer height	Smaller layer heights (e.g. 20–50 μm) lead to smoother surfaces due to finer layers. Higher layer heights (e.g. 100 μm) may result in rougher surfaces.	(Alfieri *et al*., 2022)
Laser power and speed	Higher laser power and faster scan speeds may cause incomplete melting, leading to a rougher surface.	(Ullah *et al.*, 2022)

As inclined and curved structures are produced based on CAD models, staircases emerge due to the layer-by-layer fabrication nature. In Figure 6a, a CAD model surface profile is illustrated, while Figure 6b depicts a layer-sliced object as L-PBF-constructed elements layer by layer (Abdi *et al.*, 2020). Figure 6c presents an AM manufactured clearly displaying the staircases (Nsengimana, 2015). These staircases in L-PBF-fabricated parts contribute to the overall surface irregularities of the components (Charles *et al.*, 2018). Although decreasing the layer thickness can lead to smoother surfaces in AM, it also increases the time required to produce the component resulting in significantly higher fabrication costs (Shange *et al.*, 2019).

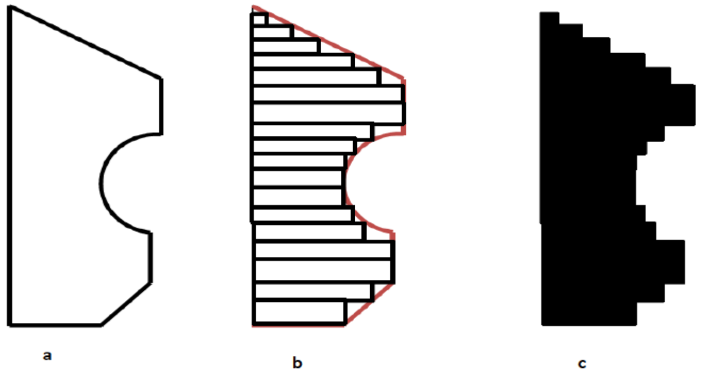

Figure 6: Staircase effect (a) CAD surface profile (b) layer slice (c) additive manufacturing profile (Nsengimana, 2015)

Part orientation optimization in L-PBF is a critical aspect of AM. L-PBF involves using a laser to selectively melt and fuse powdered material layer by layer to create a 3D object. Optimizing the part orientation can significantly impact the quality, mechanical properties, and efficiency of the final product (Chowdhury *et al.*, 2022). Table 5 shows the benefits and challenges of part orientation optimization of L-PBF parts.

Table 5: Part orientation optimization

Orientation Strategy	Benefits	Challenges	References
Horizontal (flat on build plate)	Minimizes warping, better thermal management	Requires more support for overhangs	(Bennett *et al.*, 2017)
Tilted (at ~30–45°)	Minimizes staircase effect and supports self-assembly	May need additional supports	(Shange *et al.*, 2022)
Vertical (standing)	Easier to print tall parts, and faster for simple geometries	Staircase effect, rougher surfaces	(Vukkum *et al*, 2022)

2.5.5. Melting and solidification dynamics

The rippling effect is shown in Figure 7. The development of ripples on the surfaces of single tracks is intricately linked to the dynamics of the melt pool and the subsequent solidification process. Instabilities within the melt pool, including Marangoni convection, the balling effect, and keyhole collapse, can result in the creation of ripples as the molten material solidifies (Wang *et al.*, 2019). The surface irregularities that arise from these periodic fluctuations contribute to an increase in surface roughness (DebRoy *et al.*, 2018).

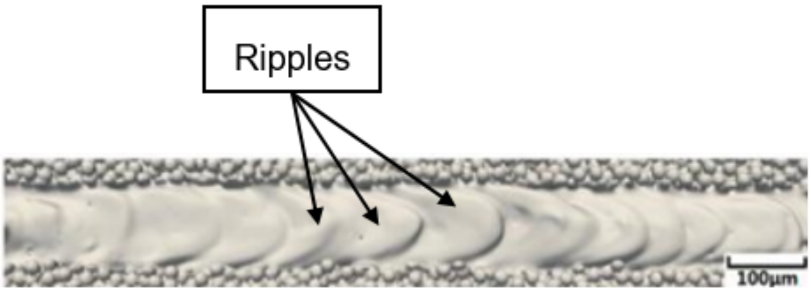

Figure 7: Ripples on the L-PBF track (Wang et al., 2019)

2.5.6. Powder delivery

An additional element influencing the surface quality of L-PBF parts is the behaviour of swaying and rolling that occurs during powder distribution. Swaying is prompted by the interactions among powder particles as they are propelled forward by the force generated by the recoater. The interplay of swaying and rolling effectively filters out smaller and medium-sized particles. This filtration allows the tiny and medium particles to navigate through the gaps between larger particles (Pal *et al.*, 2021). Gravity pulls the smaller and medium-sized particles downward, depicted in Figure 8a. Over time these smaller particles descend while larger ones rise; additionally, the cohesion among smaller particles is stronger than that among larger particles (Pal, *et al.*, 2021).

The frictional force between particles varies with their size. Larger particles having a greater contact area, experience less friction which facilitates their rotation within the powder (Pal *et al.*, 2021). Consequently, most smaller particles initially move downward, assisting other small particles in descending and adhering to one another through Van der Waals and frictional forces. Larger particles are easily removed by scraping, typically settling at the far end of the building tray, as shown in Figure 8b. Ultimately, the overall density of the powder bed is greater in areas with smaller particles compared to regions with larger ones (Ulusoy, 2023).

These processes, particularly the smooth rolling, and descent of spherical particles, result in a faster downward movement, with a majority accumulating at the powder recoater's starting point on the build plate. Conversely, irregularly shaped particles are displaced to the denser regions (Ulusoy, 2023).

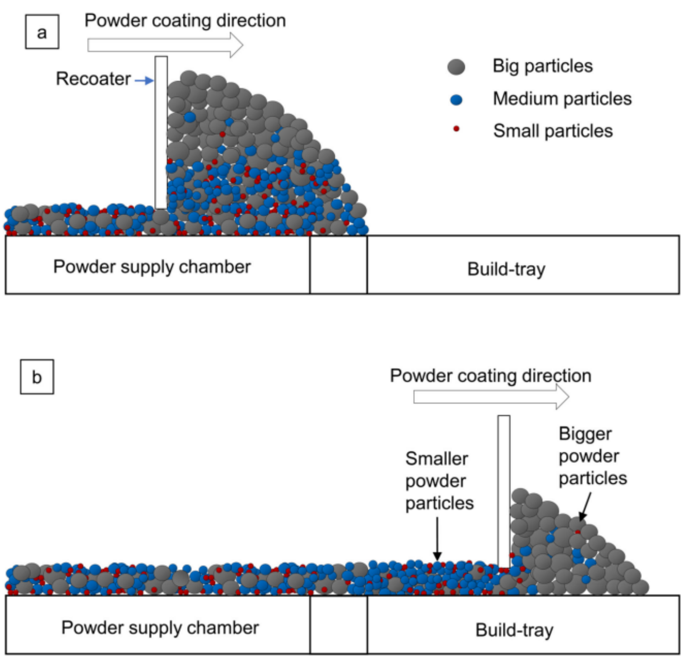

Figure 8: Powder flow arrangement mechanisms during L-PBF powder collection and distribution. The recoater gathers powder from the supply chamber (a) and distributes powder on the fabrication tray (b) (Pal et al., 2021).

2.5.7. Powder supply direction

In L-PBF the direction of the powder supply is crucial for ensuring consistent layer formation, uniform material properties, and overall process stability. Proper powder distribution directly influences the quality and mechanical integrity of the final part. Understanding the impact of the powder supply direction on part quality and process stability is essential for optimizing L-PBF operations. Studies have shown that improper powder distribution can lead to defects such as porosity or uneven surface finishes. Optimizing the direction of the powder supply in L-PBF is essential for achieving uniform powder distribution, controlling powder flow, minimizing segregation, and enhancing powder reuse. These factors collectively contribute to the production of high-quality, reliable parts (Chowdhury *et al.*, 2022).

Uniform powder distribution is essential for a consistent melt pool. If the powder supply is not evenly distributed across the build platform, some regions may receive too much or too little powder. This can lead to inconsistent layer formation, resulting in defects such as porosity or uneven surface finishes (Mahtabi *et al.*, 2024).

During L-PBF powder is typically made up of particles with a range of sizes. If the powder supply direction is not managed properly, smaller particles may segregate and concentrate in certain areas while larger particles may settle in others. This segregation can result in non-uniform material properties across the part and poorer mechanical performance in certain regions (Mussatto *et al.*, 2021).

The direction of powder flow can also affect the cooling rate of the molten material. A well-controlled powder flow helps achieve more consistent cooling across the part, which can influence the solidification behaviour of the material and lead to improved part properties, such as reduced residual stresses and better microstructure (Bennett *et al.*, 2017).

Optimizing the direction of powder supply in L-PBF involves controlling powder distribution, layer thickness, material uniformity and minimizing powder loss and contamination. The direction of the powder supply in L-PBF is crucial to ensure efficient deposition, reduced material waste, and high-quality part production. By controlling factors such as powder flow speed, deposition angle, and alignment with the laser scan path, manufacturers can optimize the process and improve part quality (Vukkum *et al*, 2022). Table 6 show the optimum powder supply direction in L-PBF.

Table 6: Optimum powder supply direction in L-PBF (Vukkum *et al.*, 2022)

Factor	Optimum direction of powder supply	Details
Powder distribution	Even across the entire build platform	The powder should be spread uniformly across the build area to ensure consistent layer thickness and avoid areas with insufficient powder.
Control over powder flow speed	Moderate to high speed, ensuring even deposition	Powder flow speed should be controlled to ensure the particles are evenly deposited without excessive turbulence or loss of material.
Minimizing powder segregation	Ensure uniform powder bed composition	Optimize the flow to avoid segregation of particles by size. Larger particles should not settle in one area, while finer ones accumulate elsewhere.
Powder loss prevention	Flow direction should be controlled to avoid loss	Argon or gas flow should be used to guide powder only to the build platform, ensuring minimal powder loss to the surrounding areas.
Alignment with laser scanning	Powder supply aligned with laser path	Powder deposition direction should complement the laser scanning pattern to ensure even melting and effective fusion of powder particles.
Powder recovery efficiency	Optimize flow to guide unused powder into recovery areas	The flow of unused powder should be directed to recovery zones to improve the reuse efficiency and reduce material waste.
Avoiding powder contamination	Controlled deposition in designated areas	Optimizing powder flow reduces the risk of cross-contamination between different powder types or batches, particularly in multi-material builds.

2.5.8. Protection gas flows

The inlet and outlet flow of argon (Ar) in L-PBF plays a critical role in determining the quality, stability, and efficiency of the printing process. For metals-based L-PBF, the interaction of the laser and powder feedstock creates by-products such as a plume (evaporated metal that condenses into small, suspended nanoparticles), spatter (material ejected from the molten pool), and powder ejecta (gas/vapour-entrained powder not fused to the part) (Shen *et al.*, 2020). L-PBF relies on Ar gas to protect the molten metal from oxidation and contamination and remove process by-products (Traore *et al.*, 2021).

One of the guiding principles for gas flow in L-PBF is uniformity. A non-uniform gas flow across the build area could result in part properties that depend on the build location due to differences in by-product removal (Weaver *et al.,* 2021). Optimizing Ar gas flow within the L-PBF chamber is crucial for determining optimal part placement on the build platform, thereby enhancing the quality and consistency of the manufactured parts. Effective gas flow management ensures the efficient removal of by-products (Ferrar *et al.*, 2012). A study by the National Institute of Standards and Technology (NIST) highlights that non-uniform gas flow can lead to variations in part quality depending on their location on the build platform. Areas with insufficient gas flow may experience increased spatter accumulation, resulting in higher porosity in parts built in those regions. This underscores the importance of careful part placement to ensure adequate exposure to the Ar flow, thereby minimizing defects (Weaver *et al.,* 2021). Table 7 show the impact of Ar gas flow on L-PBF parts quality.

Table 7: Impact of argon flow on L-PBF parts quality (Pauzon *et al.*, 2019) (Yang *et al.*, 2023)

Factor	Effect of Poor Argon Flow	Effect of Optimized Argon Flow
Oxidation	Increased oxidation and defects	Clean, oxidation-free parts
Laser stability	Laser beam distortion due to fumes	Clear beam path, stable melting
Surface finish	Rough surface due to redeposited spatter	Smooth surface, minimal defects
Thermal stresses	Uneven cooling, increased warping	Controlled cooling, reduced residual stress
Recoater issues	Powder bed disturbance, recoater interference	Even powder spreading, smooth layers

Studies have shown that non-uniform gas flow can lead to variations in part quality depending on their location on the build platform. For instance, areas with insufficient gas flow may experience increased spatter accumulation leading to higher porosity in parts built in those regions. This suggests that part placement should be carefully considered to ensure adequate exposure to the Ar flow, thereby minimizing defects (Weaver et al., 2021). Efficient Ar flow helps in clearing spatter and fumes generated during laser-material interaction. If not adequately removed, these by-products can redeposit onto the melt pool leading to surface defects and increased roughness (Yang *et al.*, 2023). A well-designed Ar flow reduces laser plume attenuation, ensuring consistent laser energy delivery to the powder bed. This consistency is vital for achieving a smooth surface finish (Sahaja *et al.*, 2019). Non-uniform or inadequate gas flow can result in inconsistent removal of by-products, leading to variations in surface finish. Studies have shown that optimized Ar flow results in more consistent and smoother surface finishes (Yang *et al.*, 2023). The optimum Ar gas flow is essential for maintaining an inert atmosphere, cooling the melt pool, and removing by-products. Proper gas flow ensures consistent part quality and process stability (Weaver *et al.,* 2021). The exact values for flow rate and other parameters can depend on the specific machine model and material being printed. Table 8 provides general ranges that are commonly used in L-PBF processes.

Table 8: *Optimum gas flow in L-PBF* (Bhadeshia, 2016) (Alquaity, 2025)

Factor	**Optimum Argon Gas Flow**	**Details**
Continuous flow rate	10–150 litres per minute	Maintains the inert atmosphere and removes by-products such as laser plume, powder spatter, and heat during the build process. The flow rate depends on machine size and material.
Gas flow speed	Higher speeds (specific values depend on setup)	Higher flow speeds can improve laser plume removal and prevent interference with the laser path.
Flow direction	Optimal alignment with the laser beam and build platform	Proper alignment ensures effective shielding and improves the mechanical properties of the printed part by controlling cooling rates and preventing contamination.
Chamber pressure	Low, controlled within L-PBF parameters	Controlled gas flow helps maintain stable pressure in the chamber, ensuring proper fusion and minimizing defects. Excessive or insufficient flow can alter chamber conditions.

2.6. Biomedical implants

2.6.1. Different kinds of metal implants

The load-bearing capacity of bone implants is crucial in their functional roles within the body. Metals are commonly preferred for bone replacement due to their favourable mechanical properties (GonzáLez-Carrasco, 2009). Frequently utilized metallic biomaterials for structural applications and bone implantation are Ti6Al4V, stainless steels, and cobalt-chromium (Co-Cr) alloys. These materials are applicable in a variety of contexts, such as the replacement of damaged hip or knee joints, cranial and maxillofacial implants, bone scaffolds, stents and bone plates, as illustrated in Figure 9 (Benčina *et al.*, 2021). Among these options Co-Cr alloys are favoured for their exceptional wear resistance and high stiffness (Ren *et al.*, 2019). Stainless steel is selected for implants due to its corrosion resistance, cost-effectiveness, and significant strength (Eliaz, 2019). Ti6Al4V alloy is preferred for its remarkable mechanical properties which encompass fatigue strength, stiffness, strength, fracture toughness and corrosion resistance along with its superior biomedical attributes such as osteointegration and low toxicity (Li *et al.*, 2014).

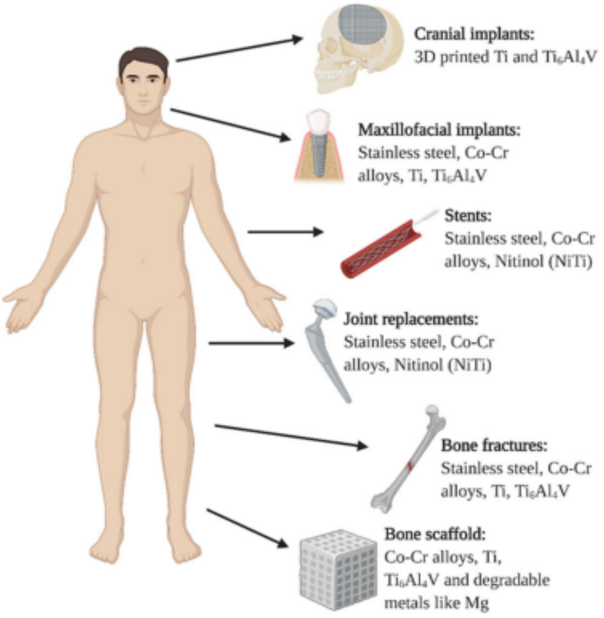

Figure 9: Metal implants used in the human body (Benčina et al., 2021)

Medical implants made of metal, which are used in orthopaedic and dental procedures, must have certain mechanical properties to be effective and last longer. The mechanical properties required differ with the type of material used for the implant, which may include stainless steel, titanium alloys, or Co-Cr alloys. The choice of material depends on a number of factors, such as compatibility, strength, corrosion resistance, and cost (Abd-Elaziem *et al.*, 2024).

Ti6Al4V implants are known for their high strength-to-weight ratio; they offer both strength and light weight. This alloy has high tensile strength and fatigue resistance and is therefore suitable for structural applications of implants like hip stems and bone plates (Tamayo *et al.*, 2021). Also, titanium alloys are valued for their high corrosion resistance especially in the biological environment, since they form a passive oxide layer that prevents further corrosion (Bocchetta *et al.*, 2021). It has been established that they have lower density than stainless steel and Co-Cr alloys, and this is advantageous in the production of lighter implants which, in turn, is useful in reducing the weight that is placed on the patient (Geetha *et al.*, 2009).

Stainless steel implants possess excellent strength, hardness, and ductility; however, it is denser than titanium alloys, and hence, the implants made from them would be heavier. This material is often used in the construction of orthopaedic implants such as bone screws and plates (Barber *et al.*, 2021). Stainless steel has fairly good corrosion resistance, but it can corrode in certain conditions or environments and may even develop localized corrosion, especially in the presence of chlorides (Eliaz, 2019). The greater density and weight of stainless steel implants compared to titanium alloys may be a consideration for weight-sensitive applications (Geetha *et al.*, 2009).

Cobalt-chromium alloy implants are known to possess high strength and hardness, excellent wear and corrosion resistance, and are, therefore, used in orthopaedic and dental implants where there is a need for high wear resistance, such as in hip and knee replacements (Szczęsny *et al.*, 2022). These alloys are also non-toxic and are widely applied in medical implants due to their high biocompatibility. However, there are reports raising the issue of ionization of cobalt (Co) and chromium (Cr) from the implants, which can result in adverse reactions in some patients (Vaicelyte *et al.*, 2020).

- Ti6Al4V is lighter and stronger than both stainless steel and Co-Cr, as seen in the data presented in Table 9.

- Because of its high strength under conditions of repeated loading, Ti6Al4V can be viewed as a material that is better for implants than stainless steel and Co-Cr (Elias *et al.*, 2018).
- Ti6Al4V, on the other hand, has a lower modulus of elasticity than stainless steel and Co-Cr, which means that it generates a lower stress on the bone structure (Table 9).
- Due to the high strength of titanium and its ability to withstand load cycles, it is used in a way that helps deal with strain in internal fixation, something that stainless steel cannot match in terms of yield strength, as detailed in Table 9.

Each of these materials – Ti6Al4V, stainless steel (316L), and Co-Cr alloys – has unique properties that make them suitable for different biomedical implant applications. Table 9 details a comparison of their mechanical, biocompatibility, and corrosion properties. For permanent implants, where bone integration is required, Ti6Al4V is the best. For temporary fixation devices, stainless steel (316L) is commonly used. For wear-resistant applications (joints, articulating surfaces), Co-Cr alloys are the best choice.

Table 9: Properties of Ti6Al4V, stainless steel, and Co-Cr

Property	**Ti6Al4V** (Geetha *et al.*, 2009)	**Stainless Steel (316L)** (AISI Type 316 stainless steel., 2020)	**Co-Cr Alloys** (Hong and Yeoh, 2019)
Density	4.43 g/cm³	8 g/cm³	8.4 g/cm³
Elastic modulus	113.8 GPa	193 GPa	238 GPa
Yield strength	800–900 MPa	200–300 MPa	573 MPa
Ultimate tensile strength	950 MPa	550 MPa	1 092 MPa
Corrosion resistance	Excellent (oxide layer prevents corrosion)	Good (but susceptible to pitting and crevice corrosion)	Excellent (high resistance to corrosion and wear)
Biocompatibility	Very high (excellent for long-term implantation)	Moderate (can release Ni & Cr ions, leading to allergic reactions)	High (widely used in joint replacements, but some ion-release concerns)
Wear resistance	Moderate	Low (prone to wear and fretting corrosion)	Excellent (high hardness and wear resistance)
Osteointegration	High (supports bone growth, especially with surface treatments)	Poor (does not bond well with bone)	Moderate (used in articulating surfaces, but poor bone integration)
Common applications	Bone plates, dental implants, hip and knee implants, spinal implants	Temporary implants (fracture fixation plates, screws, rods, cardiovascular stents)	Hip and knee replacements, dental implants, wear-resistant joint components

Several criteria must be met by the biomaterials being evaluated before an implant is inserted into the body; otherwise, their prolonged use may result in adverse effects (Saini, 2015). The selection of biomaterials for bone implants necessitates fulfilling several crucial criteria, such as biocompatibility, mechanical characteristics, resistance to corrosion, and durability against wear. These factors are vital to ensure the implant's effectiveness, its compatibility with biological systems, and long-term performance. These criteria are influenced by the biological environment, mechanical demands, and intended functions of the implant. If the biomaterial for bone implants does not fulfill these crucial requirements, they can pose health risks and may require surgical intervention (Sansone *et al*., 2013).

Ti6Al4V is the primary choice for bone replacement due to its advantageous characteristics (Sarraf *et al.*, 2022). Titanium alloys such as Ti6Al4V are favoured for use in orthopaedic implants because their elastic modulus of 110–120 GPa is more aligned with that of bone, which ranges from 10 to 30 GPa in contrast to stainless steel or Co-Cr alloys. The elasticity of the materials significantly influences the performance of implants (Heary *et al.*, 2017). When there is a substantial difference in modulus between metallic biomaterials and human bone, the natural bone may undergo resorption, which contributes to implant loosening (Saini, 2015).

2.6.2. Required properties for metal implants

Strength: Metal implants must have adequate strength to endure the loads and stresses within the body without experiencing fractures or deformation. This encompasses both tensile strength, which refers to resistance against stretching or pulling apart, and compressive strength, indicating resistance to squeezing or crushing (Moghadasi *et al.*, 2022).

Hardness: The capacity of a material to withstand deformation, indentation, or scratching. Implants require sufficient hardness to resist wear and abrasion, particularly in applications where they bear weight (Issn *et al.*, 2023).

High fatigue resistance: Essential as implants are subjected to cyclic loading over lengthy periods. If the material lacks the ability to endure repeated stress cycles, fatigue failure may occur. Enhanced fatigue resistance contributes to the durability and dependability of the implant (Wegner *et al.*, 2022).

Corrosion resistance: Crucial since metal implants are frequently exposed to bodily fluids. In the absence of corrosion-resistant materials, these fluids can induce corrosion, potentially undermining the structural integrity of the implant and resulting in failure over time (Kamachi *et al*., 2003).

Ductility: The ability of a material to undergo plastic deformation before breaking. While implants must be robust and hard, they also need a certain level of ductility to prevent brittle failure and allow for some degree of flexibility (Moghadasi *et al.*, 2022).

Toughness: This encompasses both strength and ductility, reflecting the capability of a material to absorb energy prior to fracturing. Implants that demonstrate toughness are less prone to catastrophic failure and can endure sudden impacts or excessive loads (Ahuja *et al.*, 2023).

2.6.3. Surface quality requirement for bone implants

The necessary surface quality is contingent upon the specific application (Saini, 2015) (see Table 10). Implant surfaces can range from smooth to minimally rough, moderately rough, and rough. A smooth surface is particularly critical for preventing premature failures (Rosa *et al.*, 2012). The condition of the surface of the implant has a significant impact on the response of the bone: smooth surfaces ($S_a < 0.5$ µm) and minimally rough surfaces (Ra = 0.5–1 µm) exhibit weaker bone responses compared to rougher surfaces. The moderately rough surfaces (Ra = 1–2 µm) produce better bone integration than the rough surfaces (Ra > 2 µm) as pointed out by Albrektsson *et al*., (2004). For dental implants, the ideal surface roughness is recommended to be between 1–5 µm Ra to ensure osseointegration (Buser *et al.*, 2013). Also, a moderate level of surface roughness of about 1–2 µm Ra on titanium implants has been found to enhance bone integration and better clinical performance (Wennerberg *et al*., 2009). The highest shear strength of the interface was observed on the medium surface roughness of about 1–5 µm (Hansson *et al*., 1999). Optimum results for cellular responses are achieved with surface modifications that fall between 1–5 µm (Le Guéhennec *et al.*, 2007).

The ASTM F1378 standard specifies that the metallic bearing surfaces of shoulder prostheses should have an average Ra that does not exceed 0.10 µm measured using a cut-off length of 0.25 mm. In accordance with ISO 21536, a roughness value of Ra

1.5 µm with a cut-off length of 0.8 mm is considered acceptable for non-articulating areas that may interact with soft tissue.

Additionally, the ISO-7602-2 standard states that the spherical articulating surfaces of metallic components in the femoral head parts of total hip joint prostheses must maintain Ra values of no more than 0.05 µm with a maximum total profile height (Rt) of 1.0 µm measured at a cut-off length of 0.08 mm.

Table 10: Required surface roughness for different kinds of implants

Type of Ti6Al4V implant	Application	Required surface roughness (Ra, µm)	Reason for surface roughness requirement	Surface characterization method	References
Dental implants	Tooth root replacements	1.5–3.0	Enhances osseointegration (bone growth) and mechanical stability.	Scanning Electron Microscopy (SEM), X-ray Diffraction (XRD)	(Le Guéhennec *et al.*, 2007) (Jemat *et al.*, 2015a)
Orthopaedic implants	Hip, knee, shoulder, and spinal implants	2.0–5.0	Promotes better bone-implant integration and reduces implant loosening.	Optical Profilometry, Atomic Force Microscopy (AFM)	(Jemat *et al.*, 2015b)

2.7. Surface roughness and properties of implants

2.7.1. Mechanical stress and fatigue

A defective feature on the surface of an as-fabricated AM component can be associated with a decrease in fatigue performance (Fatemi *et al.*, 2020). The fatigue life of parts that are subjected to tensile, and bending loads is also reduced due to the comparatively high surface roughness of as-built components (Balachandramurthi *et al.*, 2018). This reduction of the fatigue strength can be attributed to the notch effect and stress concentrations due to surface defects (Du Plessis *et al.*, 2020).

In numerous industrial settings, including joint implants, Ti6Al4V processed by L-PBF often faces dynamic loading conditions necessitating an in-depth exploration of its fatigue behaviour and properties to accurately assess its fatigue life (Liverani *et al.*, 2017). Such conditions increase the Ra and hence the localized stresses, leading to reduced fatigue limits and life of L-PBF processed components. Surface texture is one of the most significant factors that define the fatigue behaviour of these products (Uhlmann *et al.*, 2017). High cycle fatigue (HCF) are more sensitive to the roughness of the surface and the defects on it. The HCF performance of L-PBF components can be improved by reducing the roughness of the surface and the defects on the surface (Riemer *et al.*, 2014).

2.7.2. Surface roughness and healing process

For biomedical implants such as hip, knee, and dental implants, high levels of roughness become a barrier to the bonding between the implant and the bone or the surrounding tissues. While a moderate level of roughness may enhance the bonding, too much of it can lead to the development of zones that hinder tissue bonding, thus increasing the chances of implant loosening or rejection. Also, the rough surface can cause inflammation at the implant site, hindering the healing process and the stability of the implant (Hashmi *et al.*, 2023).

It has been noted that bacteria adhere to the rough surfaces of implants, and biofilm is formed, which in turn increases the risk of infection, including peri-implantitis. This poses a challenge because cleaning these rough surfaces during and after implantation is difficult. (Săndulescu *et al.*, 2023).

Excessive or poorly controlled roughness can result in uneven healing or instability of the implant. Furthermore, it may prolong the time required for complete osseointegration, thereby reducing the stability of the implant during the initial stages (Hossain *et al.*, 2023).

2.7.3. Accelerated corrosion and wear

Higher surface roughness increases the surface area of the implant, which can accelerate both corrosion and wear in metallic implants. This leads to the production of wear particles and ions that may induce inflammatory responses or compromise the biocompatibility of the implant (Eliaz, 2019).

2.8. Type of implants produced by L-PBF

L-PBF enables the production of customized, lightweight, and highly durable Ti6Al4V implants with complex geometries and porous structures for enhanced osseointegration and biomechanical performance. These advantages make L-PBF a revolutionary technology for personalized medicine and orthopaedic applications (Benčina *et al.*, 2021). Table 11 show various kinds of Ti6Al4V implants that can be produced by L-PBF.

Table 11: Types of implants produced by L-PBF (Depboylu *et al.*, 2022) (Benčina *et al.*, 2021)

Type of Implant	**Description**	**Application**	**Advantages of L-PBF**
Dental implants	Customized crowns, bridges, and root replacements	Orthodontics, prosthodontics, maxillofacial surgery	High precision, biocompatibility, patient-specific design
Hip implants	Acetabular cups, femoral stems	Hip joint replacement (arthroplasty)	Porous structures for better osseointegration
Knee implants	Femoral and tibial components	Total knee replacement (TKR)	Complex geometries, reduced material waste
Spinal implants	Vertebral cages, rods, and interbody fusion devices	Spinal fusion, scoliosis correction	Lightweight, tailored stiffness, excellent bone integration
Cranial implants	Patient-specific skull plates	Cranioplasty (trauma, deformities, tumour removal)	Custom-made for patient anatomy, improved healing
Maxillofacial implants	Jaw reconstruction plates, mandibular joint prostheses	Facial reconstructive surgery	Custom geometries, high mechanical strength
Shoulder implants	Humeral head, glenoid components	Shoulder arthroplasty (joint replacement)	Improved wear resistance, complex anatomical shapes
Elbow implants	Hinged and unlinked prostheses	Total elbow arthroplasty	Better fit for individual patients, reduced stress shielding
Ankle implants	Tibial and talar components	Ankle joint replacement	Enhanced mechanical properties, tailored pore structures
Hand and wrist implants	Carpal and metacarpal prostheses	Hand and wrist reconstructive surgery	Lightweight, personalized design, reduced surgical time

2.9. Post-processing of L-PBF components

Residual stresses are a result of temperature differences that occur during the manufacturing processes (Mugwagwa *et al.*, 2021). The impact of these residual stresses can be either beneficial or detrimental, depending on their levels (Nasir *et al.*, 2016). A study by Lammi *et al.* (2011) on fracture growth behaviour revealed that the stress intensity factor is related to residual stresses. Temperature factors are known to affect these stresses in one way or the other. Rashid *et al.* (2023) found that increasing the height of the sampling is also followed by an increase in residual tension. These stresses are usually latent and can only be observed in case of failure (van Zyl *et al*., 2016). Residual stress is one of the leading causes of structural failure, as shown in Figure 10 (Chiocca *et al*., 2021).

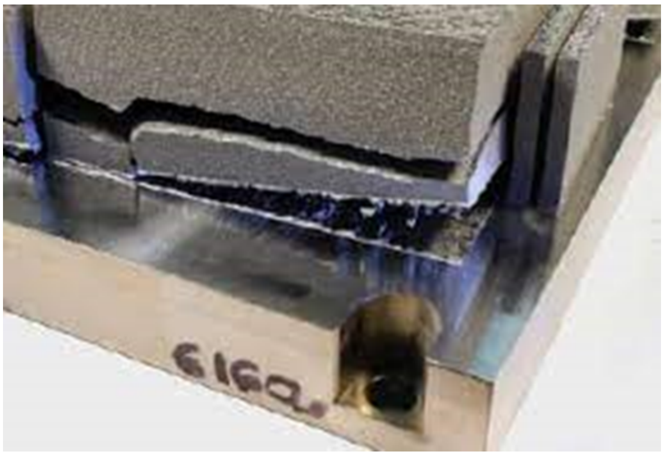

Figure 10: Effect of the presence of a residual stress (Chiocca et al., 2021)

Residual stress is a major concern in Ti6Al4V implants produced by L-PBF because it can lead to cracking, distortion, and reduced fatigue life (Mugwagwa *et al*., 2021). Table 12 summarises the most effective methods for minimizing residual stress in L-PBF-produced Ti6Al4V implants.

Table 12: Optimal residual stress reduction for different Ti6Al4V implants

Type of implant	Common stress issues	Best solutions for residual stress reduction	References
Hip implants (femoral stem, acetabular cup)	Large thermal gradients due to complex geometry. High mechanical loads lead to fatigue failure.	1. Preheating at 300–500 °C to reduce stress during printing. 2. HIP treatment (~920–1 000°C, 100–150 MPa, 2–4 hours) to fully relieve internal stress. 3. Optimized laser scanning strategy (lower power, reduced hatch spacing) for uniform melting. 4. 45° build orientation to reduce warping.	(Vrancken *et al*., 2012) (Murr *et al*., 2009)
Dental implants (screws, abutments, prosthetic structures)	Small, intricate geometries are prone to localized stress concentrations. Surface roughness affects osseointegration.	1. Preheating at 200–300 °C to reduce localized stresses. 2. Stress-relief annealing (~600–750 °C, 1–2 hours) to improve fatigue life. 3. Post-processing with electropolishing or shot peening to remove residual stress and enhance surface quality.	(Jemat *et al*., 2015a) (Albrektsson and Wennerberg, 2004)

Type of implant	Common stress issues	Best solutions for residual stress reduction	References
		4. Controlled cooling to avoid rapid temperature changes.	
Spinal implants (cages, rods, screws)	High residual stress can lead to crack formation. The implant must maintain mechanical integrity for fusion with bone.	1. Preheating at 250-400 °C to prevent warping. 2. Stress-relief annealing (650–750 °C) to reduce built-in stress. 3. Shot peening or laser remelting to improve surface smoothness and reduce stress concentrations. 4. Optimized support structure design to minimize distortions.	(Le Guéhennec *et al.*, 2007) (Niinomi, 2008)

The as-built surface roughness of Ti6Al4V samples produced by L-PBF is often higher than what is acceptable for medical implants or components. As-built Ra for Ti6Al4V produced via L-PBF usually ranges between 5–20 µm for top and side surfaces. The top surface (typically parallel to the build plate) tends to have a smoother finish compared to side surfaces (vertical or inclined to the laser path), which usually exhibit higher roughness due to the step-like features from the layer-by-layer build process (Obeidi *et al.*, 2022).

Before L-PBF components can be utilized in the human body, it is necessary for them to undergo surface refinement to meet the established quality standards. Surface finishing is vital for L-PBF-manufactured parts due to several factors, including mechanical performance, enhanced wear resistance, improved surface integrity, biocompatibility, dimensional accuracy, and aesthetic appeal (Lee *et al.*, 2021).

Research conducted by Wennerberg *et al*, (2009) indicates that the polishing of Ti6Al4V surfaces is linked to the adhesion of soft tissues. According to Barfeie *et al*, (2015) the rough surface texture of L-PBF components facilitates bone-to-implant interlocking and improves osseointegration. Lin *et al*., (2009) highlight that high RA can lead to poor wear resistance, posing challenges for specific biomedical applications.

Given the intrinsic characteristics of L-PBF that result in some surface irregularities, there is an ongoing exploration of effective post-processing methods. Currently, techniques such as manual finishing, mass finishing, burnishing, media blasting, peening, CNC finishing, ultrasonic nanocrystal, chemical polishing, electro finishing, chemical abrasive flow, electro-discharge, laser polishing, and thermal deburring are being implemented to address the surface texture challenges associated with AM products (Sibanda *et al.*, 2019). The choice of post-processing method can significantly influence the properties of the outer layer and the overall shape of AM parts, necessitating careful consideration in the selection process (Bouland *et al.*, 2019).

Post-processing surface finishing techniques for AM metal components can be classified into three groups: mechanical, electro/chemical, and thermal methods (Figure 11). Existing post-processing methods are described in Appendix 2.

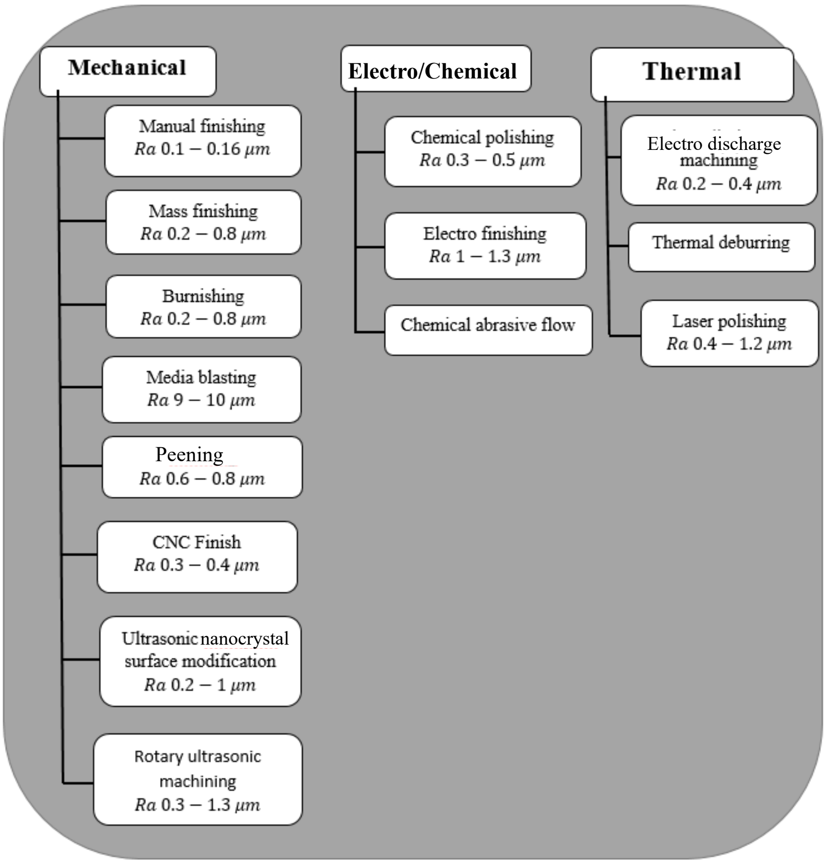

Figure 11: Implants commonly used post-process surface finish techniques and typical Ra (Sibanda et al., 2019)

2.10. Ti6Al4V alloy for biomedical applications

Ti6Al4V is an alloy which consists of 6% aluminium and 4% vanadium. Aluminium improves the stability of the alpha phase, while vanadium enhances the stability of the beta phase (Cherenda *et al.*, 2018). This alloy is also called the alpha-beta alloy since, at room temperature, it contains both the alpha and beta phases in the solid solution. Since the introduction of Ti6Al4V, several titanium alloys have been developed, but none have gained widespread popularity. (Zhang *et al*., 2022). Ti6Al4V is widely used in biomedical applications because it is corrosion resistant, strong, light in weight and can easily be cast into different shapes and forms (Cherenda *et al.*, 2018). The microstructure of titanium alloys is complicated due to the addition of alloying elements and thermomechanical processing, which are further affected by the specific types and quantities of these elements (Raji *et al.*, 2020).

Typical microstructure of Ti6Al4V alloys: Alpha (α) phase: At room temperature, Ti6Al4V is mainly constituted of α phase which has a hexagonal close-packed (HCP) crystal structure (Figure 12). Aluminium (Al) and vanadium (V) are also present in the α phase and these elements are incorporated in the matrix to provide their respective contributions to the solid solution strengthening of the material (Lu *et al.*, 2022).

Beta (β) phase: Ti6Al4V changes to the β phase at a higher temperature, where the microstructure of the alloy transforms into body-centered cubic (BCC) (Figure 12) (Liu *et al.*, 2021). The findings also reveal that the transus temperature of pure titanium is around 882 °C (Liu *et al.*, 2021). The β phase starts depending on the specific alloy composition and processing techniques used. This phase brings more strengthening thereby increasing the alloy’s ductility and strength (Lu *et al.*, 2022).

Alpha-Beta (α+β) phase: In practical applications, Ti6Al4V implants often exhibit a dual-phase microstructure consisting of both α and β phases. This α+β microstructure is achieved through controlled heat-treatment processes such as solution treatment followed by aging (precipitation hardening) (Motyka *et al*., 2014). The α+β microstructure offers a balanced combination of strength, ductility, and corrosion resistance making it well-suited for implant applications (Bauristhene *et al*., 2013).

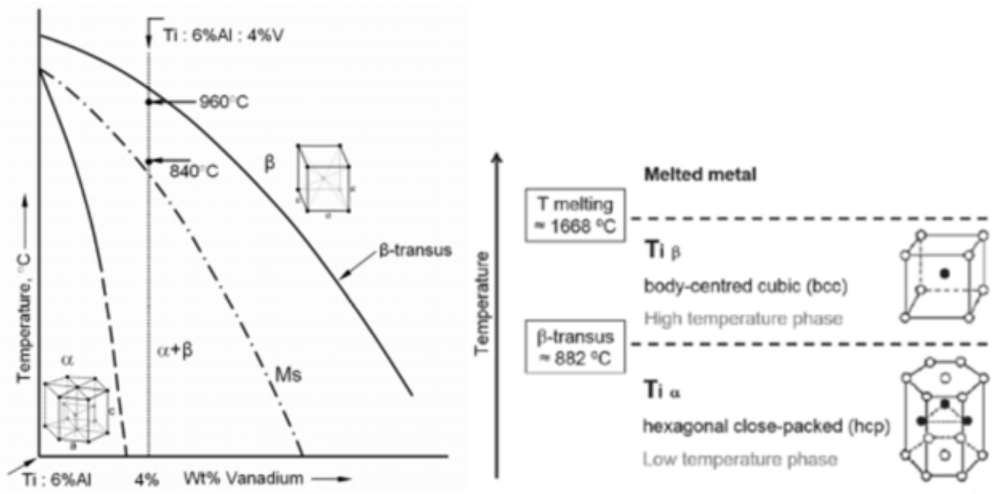

Figure 12: Schematic phase diagram of Ti6Al4V alloy; beta-transustemperature is 882 °C (Lu *et al.*, 2022)

Lamellar microstructures, as shown in Figure 13a, are important in specific metallic implant materials, particularly in titanium alloys such as Ti6Al4V. These alloys feature lamellar microstructures characterized by alternating layers of α and β phases. Typically, this lamellar configuration develops during heat-treatment processes including solution treatment followed by aging. The presence of lamellar microstructures in titanium alloys contributes to an optimal combination of strength, ductility and fatigue resistance rendering them ideal for load-bearing implant applications such as hip stems and bone plates (Etesami *et al*, 2022).

Equiaxed microstructures, as shown in Figure 13b, are frequently found in Ti6Al4V implants, especially in areas where directional solidification is not the primary mechanism. For instance, in cast Ti6Al4V implants or in areas distant from the heat-affected zones of welded implants, equiaxed grains that are approximately spherical can develop during the processes of solidification or recrystallization. These equiaxed microstructures can offer isotropic mechanical properties and enhanced formability which makes them advantageous for specific implant applications (Fischer *et al.*, 2023).

Bimodal microstructures, as shown in Figure 13c for Ti6Al4V implants, can occur either deliberately or inadvertently during the manufacturing process. For example, in AM techniques such as selective laser melting (SLM), the solidification phase can produce a combination of fine equiaxed grains alongside larger columnar grains, resulting in a bimodal microstructure. Furthermore, these microstructures can be purposefully designed through thermomechanical processing to create an optimal balance of strength and toughness in designated areas of the implant (Gorsse *et al.*, 2017).

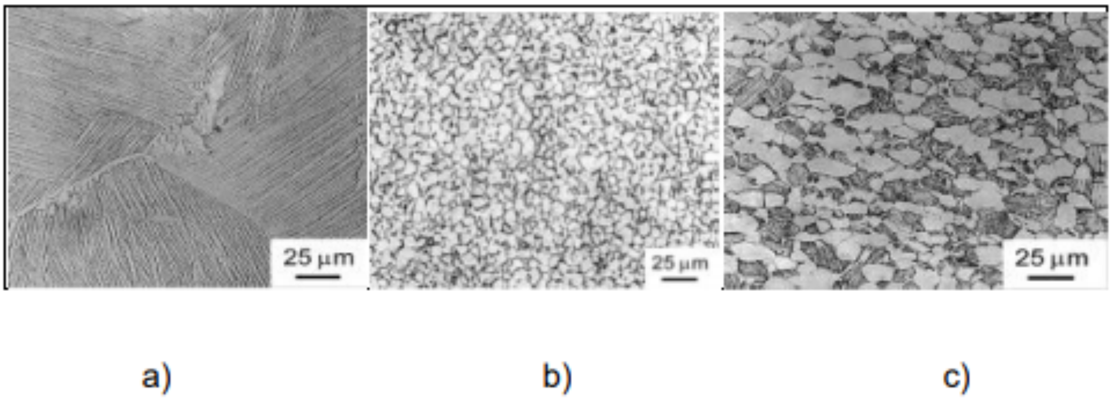

Figure 13: Ti6Al4V microstructure: (a) lamella structure, (b) equiaxed structure (c) bimodal structure (Etesami et al., 2022), (Fischer et al., 2023), (Gorsse et al., 2017)

The Ti6Al4V alloy requires post-heat treatment, which is an essential process that aims at improving the mechanical properties of the material as well as the microstructure to meet the requirements of the specific application in the biomedical, aerospace, and high-performance engineering fields. Although Ti6Al4V has excellent strength-to-weight ratio and corrosion resistance, its properties can be enhanced through appropriate heat treatment (Vrancken *et al.*, 2012).

There are several methods that can be used on Ti6Al4V implants to achieve the required microstructures, reduce internal stresses, and improve mechanical and fatigue properties. These techniques can be adjusted to fulfill the particular objectives of the implants, such as the mechanical properties, microstructure, and the application type (Wang *et al.*, 2023). The microstructure and performance of the material also depend on the heating, cooling, and holding times which have to be well-controlled (Vrancken *et al.*, 2012). Table 13 show different heat treatment techniques to obtain the required mechanical properties and microstructure for various Ti6Al4V implants.

Table 13: Heat treatment methods used for Ti6Al4V implants

Heat treatment method	**Process parameters**	**Effect on microstructure**	**Mechanical properties**	**Best implant applications**	**References**
Stress-relief annealing	600–750 °C for 2–4 hours, followed by slow cooling	- Partially decomposes α′ (martensite) into α+β phases - Reduces residual stress	- Improves ductility - Reduces cracking risk - Slight decrease in strength	- Dental implants - Spinal implants (cages, rods, screws) - Non-load-bearing orthopaedic implants	(Albrektsson *et al.*, 2004) (Niinomi, 2008)
Hot isostatic pressing (HIP)	920–1 000 °C at 100–150 MPa for 2–4 hours, followed by slow cooling	- Eliminates porosity - Converts martensitic α′ into equiaxed α+β grains	- Increases fatigue strength and toughness - Improves wear resistance - Enhances fracture resistance	- Load-bearing implants (hip, knee, femoral stems, acetabular cups) - Highly stressed orthopaedic implants	(Vrancken *et al.*, 2012) (Murr *et al.*, 2009)
Annealing (full recrystallization)	850–950 °C for 1–4 hours, followed by slow cooling	- Produces a coarse α+β structure - Reduces internal stresses	- Enhances toughness but reduces strength - Improves machinability	- Custom implants requiring machining - Non-load-bearing orthopaedic implants	(Le Guéhennec *et al.*, 2007) (Niinomi, 2008)

2.11. Summary

- The literature shows that the surface roughness of the as-built Ti6Al4V parts produced by L-PBF is influenced by many factors such as process parameters, powder size distribution, melting and solidification, building orientation, staircase effect, non-uniform Ar gas flow in the chamber, process-induced defects including partially melted particles, spatters, etc.
- As-built L-PBF parts have rougher surfaces that necessitate post-processing to meet the surface finish requirements of Ti6Al4V implants.
- The literature shows that there are several methods used for surface finishing of Ti6Al4V implants produced by L-PBF. However each method has its limitations, such as difficulty controlling unformity, dimensional inaccuracy, not

being effective for internal surfaces or complex geometries, and can introduce embedded particles, affecting biocompatibility.

- Implants made of Ti6Al4V typically require a surface roughness of Ra ≤ 5 μm for biocompatibility, osseointegration, and mechanical performance. Ra values in the 1–2 μm range are often preferred for load-bearing implants as they promote better cell adhesion and bone growth.
- The surface roughness of Ti6Al4V parts produced by L-PBF in their as-built state is generally too high to be used in implant applications without post-processing. The Ra values of as-built L-PBF parts can range from 5–20 μm or higher, which does not meet the Ra ≤ 5 μm standard required for biocompatibility, mechanical performance, and osseointegration in medical implants. This necessitates a post-processing surface finish to ensure the parts are suitable for implantation.

CHAPTER 3: MATERIAL AND METHODS

3.1. EOSINT M290 L-PBF system

The EOSINT M290 system shown in Figure 14 is an L-PBF system manufactured by EOS GmbH, a leading provider of industrial 3D printing solutions. This machine is tailored for the creation of high-quality metal components through AM processes. The EOSINT M290 was utilized to fabricate the samples for this research at the Centre for Rapid Prototyping and Manufacturing (CRPM) located at Central University of Technology, Free State (CUT) in Bloemfontein. The operational parameters of the system are confined to those outlined in Table 14. This equipment employs both nitrogen and Ar atmospheres for material protection.

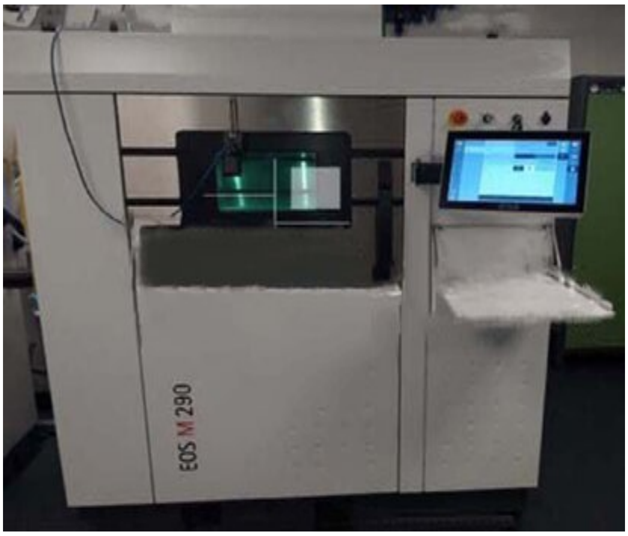

Figure 14: EOSINT M290 machine

Table 14: EOSINT M290 machine specifications

Build volume	250 mm x 250 mm x 325 mm
Laser type	Yb-fibre laser, 400 W
Precision optics	F-theta-lens, high-speed scanner
Scan speed	Up to 7m/s
Variable focus diameter	74 μm
Power supply	32A/400 V
Power consumption	Maximum 8.5 kW/average 2.4 kW/with platform heating up to 3,2 kW
Compressed air supply	7 000 hPa
AR supply	4 000 hPa

DIMENSIONS	
System	2 200 mm x 1 070 mm x 2 290 mm
Recommended installation space	Min 4.8 m x 3.6 m x 2.9 m
Weight	Approx. 1 250 kg
DATA PREPARATION	
Software	PSW/EOSPRINT 2.11
Version of software	PSW version 3.6.86
CAD interface	STL Optional: converter for all standard formats
Network	Ethernet

The samples for this study were produced using the L-PBF technique with the EOSINT M290 system from EOS GmbH. The samples were printed using EOSPRINT 2.11 software in an Ar-filled chamber and the recommended process parameters from the original equipment manufacturer.

3.2. Ti6Al4V ELI powder

The samples used in this research were created from Ti6Al4V ELI powder. Details regarding the chemical composition of the powder are presented in Table 15. This powder meets the specifications outlined in ASTM F1472. The powder particles varied in size and shape, including small, medium, large, and irregularly shaped particles, as shown in Figure 15. The particle size was in a range of 15–75 µm.

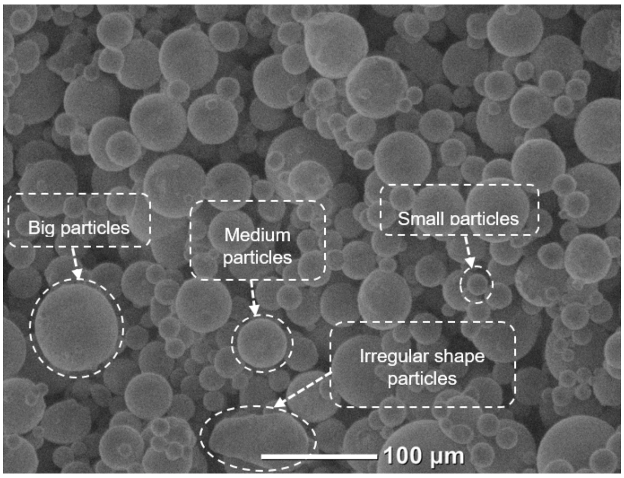

Figure 15: SEM photo of employed Ti6Al4V ELI powder

Table 15: Chemical composition of Ti6Al4V alloy

Element	Content (%)
Titanium, Ti	Bal
Aluminium, Al	6,31
Vanadium, V	4,09
Iron, Fe	0,20
Carbon, C	0,005
Nitrogen, N	0.009
Hydrogen, H	0,003
Oxygen, O	0,12

3.3. Design of experiments

3.3.1. Building layout plates

The samples were printed at multiple positions on the same plate. At least three specimens, namely vertical, horizontal, and semi-spherical samples, were produced to investigate the influence of different building orientations on surface roughness.

Figure 16 llustrates the positioning of each sample and the inlet and outlet directions for the Ar gas as well as the powder supply direction during the manufacturing process on the EOSINT M290 system. It also shows the zones to which each of the vertical, horizontal, and semispherical samples belongs.

To evaluate the impact of location on surface roughness, the samples were categorized into zones 1 through 9 based on the supply directions for powder and Ar, as shown in Figure 16. The red and blue arrows indicate the two sides of both horizontal and vertical samples, with the red arrow denoting side A and the blue arrow indicating side B.

Additional Ti6Al4V (ELI) semi-spherical samples were created with a specialized holder to fit the electropolishing machine. The additional semispherical samples were created under the same conditions as that of Figure 16a, employing the L-PBF technique with the EOSINT M290 system. Nine semispherical additional samples were fabricated on a single plate and allocated into zones, as shown in Figure 16b.

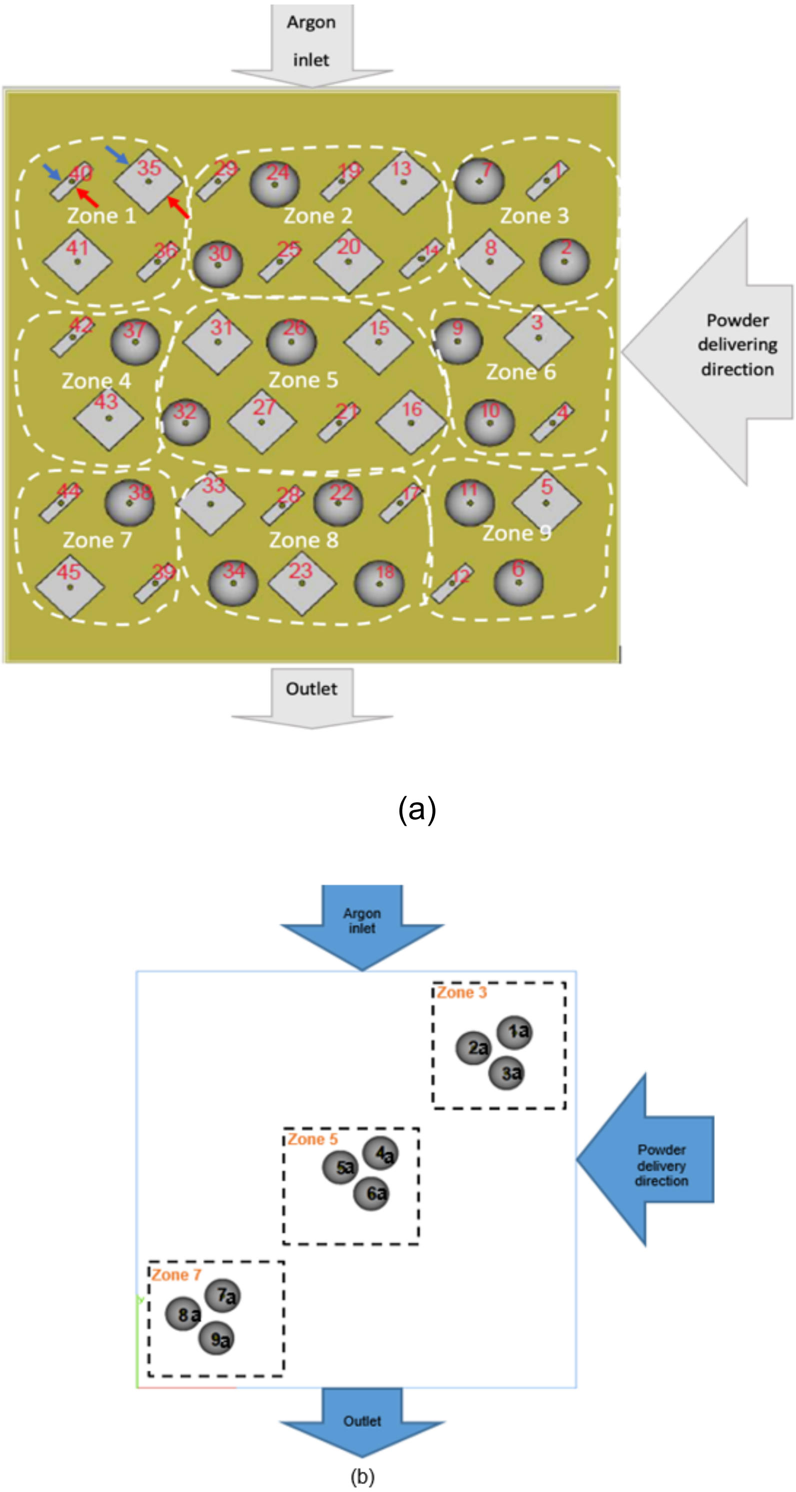

(a)

(b)

Figure 16: (a) Building plate showing the positions of the samples within the building plate and (b) additional plate with semispherical samples with a special holder

3.3.2. Horizontal samples

Figure 17 illustrates the CAD horizontal samples created using the EOSINT M290 with Ti6Al4V ELI powder. A total of 15 samples were strategically positioned on the building plate to examine how their placement affects surface irregularities. Horizontal bars were also fabricated to analyze the surface roughness of the as-built and the finishing of the inter-track on the upper surfaces.

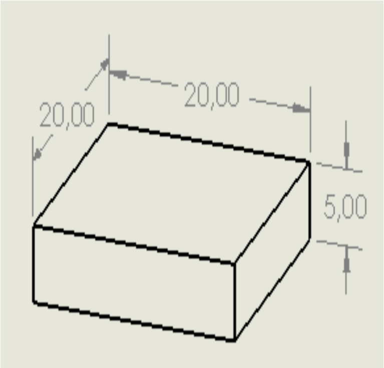

Figure 17: CAD horizontal sample with sizes (in mm)

3.3.3. Vertical samples

Figure 18 show the vertical samples created using CAD measuring 5 mm x 20 mm x 20 mm. A total of 15 vertical bars were manufactured to examine the roughness of the as-built surfaces and after surface finishing with particular attention given to the roughness between layers and the influence of placement within the building plate. The surface roughness on the side surfaces of the vertical samples was evaluated.

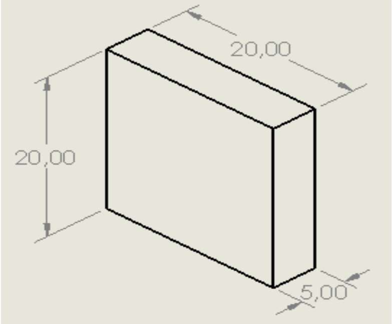

Figure 18: CAD Vertical sample (in mm)

3.3.4. Semispherical samples

A semi-sphere with a diameter of 20 mm, as shown in Figure 19, were produced to examine the surface roughness of curvey components. Additionally, to assess how the positioning affects surface roughness in relation to Ar intake and powder recoating, 15 samples with the addition of 9 samples with a holder (4 mm x 4 mm x 2 mm) were fabricated at various locations on the building plate. The additional Ti6Al4V ELI semi-spherical samples were created with a specialized holder (4 mm x 4 mm x 2 mm), as shown in Figure 19b, to fit the electropolishing machine.

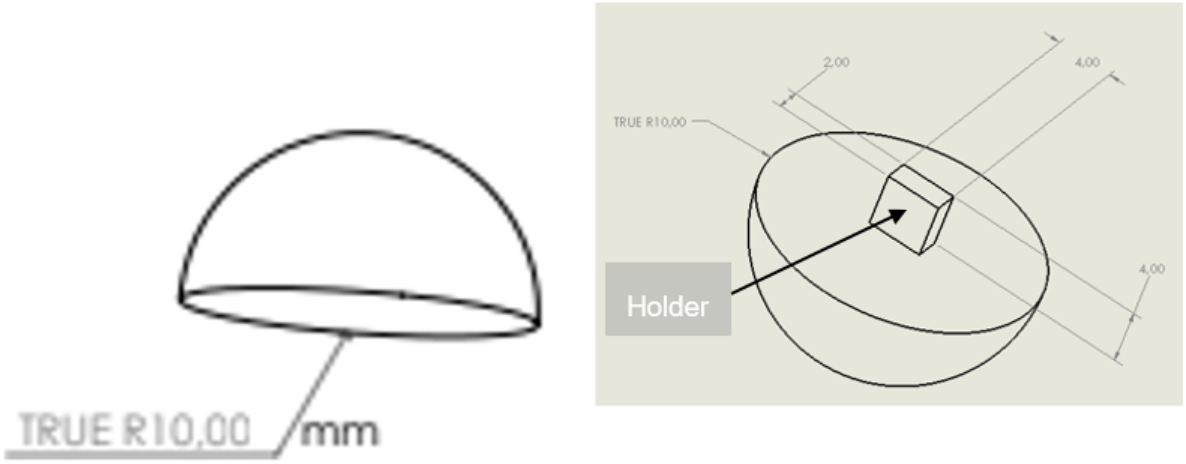

(a) (b)

Figure 19: CAD semispherical sample (a) semisphere with special holder (b) (in mm)

3.3.5. Post-heat treatment of samples

Figure 20 illustrates the heat treatment process applied to the manufactured samples for stress relief and annealing, which involved a stress-relief treatment at 650 °C for 3 hours, followed by an annealing process at 950 °C for 2 hours, in a vacuum furnace, as detailed in Yadroitsev *et al*., (2014).

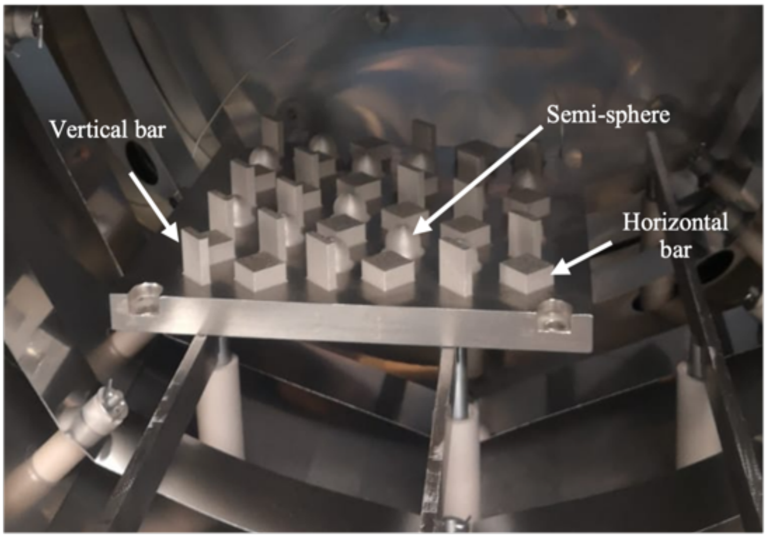

Figure 20: Samples in a vacuum furnace

3.4. Equipment for sample preparation and testing

3.4.1. Ultrasonic bath

Before assessing the surface roughness and capturing SEM images of the samples in their initial state and post-surface finishing, any contaminants present on both the printed and finished surfaces were removed. This cleaning process involved the use of acetone, ethanol, and distilled water in an ultrasonic bath, as depicted in Figure 21. The samples were immersed in the ultrasonic bath for 15–30 minutes, which is the recommended practice for biomedical implants. Subsequently, the samples were dried using compressed air.

Figure 21: Ultrasonic bath machine

3.4.2. Mitutoyo Surftest SJ-210

The surface roughness of the samples, both in their as-built state and after surface finishing, was assessed using the Mitutoyo SURFTEST SJ-210 illustrated in Figure 22. The Mitutoyo SURFTEST SJ-210 is a portable device for measuring surface roughness produced by Mitutoyo Corporation, a prominent manufacturer of precision measuring instruments. This model is engineered for reliable and effective surface roughness assessment across a range of industrial uses. The SURFTEST SJ-210 is particularly adept at evaluating the roughness of surfaces, adhering to the ISO 427:1997 standards, and displaying the results directly on its screen.

Figure 22: Mitutoyo surftest SJ-210

The arithmetical mean roughness (Ra), root mean square roughness (Rq), and average maximum height of the profile (Rz) of the top and side surfaces of each vertical, horizontal, and near-top semi-spherical sample were evaluated using the Mitutoyo Surftest SJ-210. In surface roughness analysis, Ra, Rq, and Rz are commonly chosen because they provide a comprehensive yet practical evaluation of the surface texture. Ra is commonly used because it provides a general indication of surface quality, is simple to measure, and is widely accepted in industry standards. Rq is more sensitive to peak variations than Ra, which is useful in L-PBF since melt pool instability can cause localized roughness variations. Rz measures the average height difference between the highest peak and lowest valley over a set number of sample lengths. The most extreme surface irregularities are highlighted, which are critical for fatigue resistance, coatings, and adhesion. This is more relevant for L-PBF, where high peaks or deep valleys can lead to mechanical failure. The Ra, Rq, and Rz together provide a balanced evaluation of the L-PBF surface roughness. For each sample, three measurements were obtained from randomly selected locations, and the averages, along with the standard deviation of these values, were calculated and presented. Each measurement was taken with a cut length of 0.8 m and an evaluation length of 4 mm, ensuring compliance with ISO 4288 and ASTM F42 for a single measurement.

3.4.3. Adjustable jigs for surface roughness measurement of curved surfaces

Measurements of the surface roughness of the curved samples were conducted using adjustable jigs, as shown in Figure 23. This jig is magnetically secured to the steel leg of the measurement table, as illustrated in Figure 23a. The semi-spherical samples were firmly attached to the specimen clamp shown in Figure 23b. As the stylus shown in Figure 23c traversed the sample, the movable arm illustrated in Figure 23d assisted in guiding and keeping the stylus in contact with the sample to ensure accurate measurements within the designated range. Adjustable knobs were used to position the jig correctly for the Mitutoyo Surftest SJ210 stylus. Surface roughness measurements were randomly taken five times near the upper surfaces of each semi-spherical sample, with the measurements being oriented perpendicular to the layers of the samples.

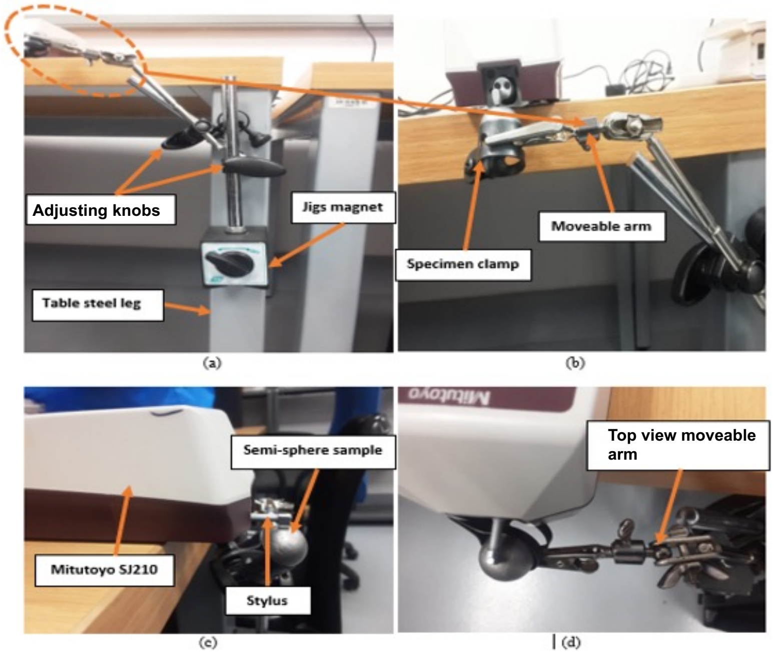

Figure 23: Adjustable jigs for surface roughness measurements of curved surfaces

3.4.4. Kern ABT120-5DNM balance

Mass was measured before and after chemical polishing using analytical balance kern ABT120-5DNM shown in Figure 24. Kern ABT120-5DNM is a high-precision analytical balance produced by Kern & Sohn, a German company known for manufacturing precision weighing instruments. This instrument is a highly sensitive and precise weighing instrument used primarily in laboratories and scientific research settings. They are designed to measure the mass of substances with exceptional accuracy, often to four or five decimal places (0.0001 g or 0.00001 g), depending on the model. Analytical balances are commonly used in chemistry, pharmaceuticals, biotechnology, and other scientific fields where precise measurements are of most importance. Compared to other types of balances, analytical balances are usually associated with enhanced capabilities like internal calibration functions, data recording features, touchscreen displays, and provisions for connecting the balance to other instruments or a Laboratory Information Management System (LIMS).

Figure 24: Analytical balance ABT 120-5DNM

3.4.5. Fluke 568EX infrared thermometer

The temperature of the solution during chemical polishing was recorded using an infrared thermometer, as shown in Figure 25. This type of thermometer determines temperature by detecting the thermal radiation emitted by an object, allowing for measurements to be taken from a distance without direct contact. It is capable of measuring temperatures ranging from -40 °C to 800 °C.

Figure 25: Fluke 568EX infrared thermometer

3.4.6. JCM 5000 NeoScope scanning electron microscope

The JCM 5000 NeoScope in Figure 26 was used to gather qualitative data from both the as-built state and post-surface finishing. This scanning electron microscope (SEM) facilitates a detailed visual examination of the components. It allows for high magnification imaging with excellent resolution and significant depth of focus akin to operating a digital camera while utilizing the advanced electron optics inherent in SEM technology. The photographs were taken to assess the surface roughness of each as-built and surface-finished sample. Images depicting the vertical, horizontal, and semi-spherical surfaces of both the as-built and finished morphologies were captured at various magnifications.

Figure 26: JCM 5000 NeoScope

3.5. Surface finishing methods and equipment

3.5.1. Dlyte dry electropolishing method

The Dlyte dry electropolishing (DryLyte) machine shown in Figure 27 was used to polish the samples for this research. DryLyte electropolishing is an advanced surface finishing technology developed by GPAINNOVA, a company specializing in innovative electrochemical processes. Unlike traditional methods, DryLyte utilizes specific electrolytes tailored to individual materials instead of liquid electrolytes, as detailed in Table 16. In the dry electropolishing process, humidity is a critical factor; there is a direct correlation between electrical current and humidity levels. A humidity sensor positioned on the holder evaluates moisture levels every two minutes throughout the cycle. Excess humidity can result in overly aggressive material removal and an uneven surface finish prompting the machine to adjust its operations based on current humidity conditions. This technology improves the surface finish of metals by facilitating ion transport.

During the dry electropolishing, the samples are firmly secured at the bottom of the anode, as illustrated in Figure 27a. The samples are drawn into a bucket that contains dry electrolyte media particles (i.e. Ti group-Ti01 shown in Figure 27d). A cathode, shown in Figure 27a, located in the bucket, generates stable electrical fields that promote a uniform surface finish. Additionally, a humidity sensor and a high-precision pump, circulate distilled water through the pipes shown in Figure 27d and 28e, modify the conductivity of the medium particles. The parameters governing the polishing process are displayed on the screen, as seen in Figure 27f.

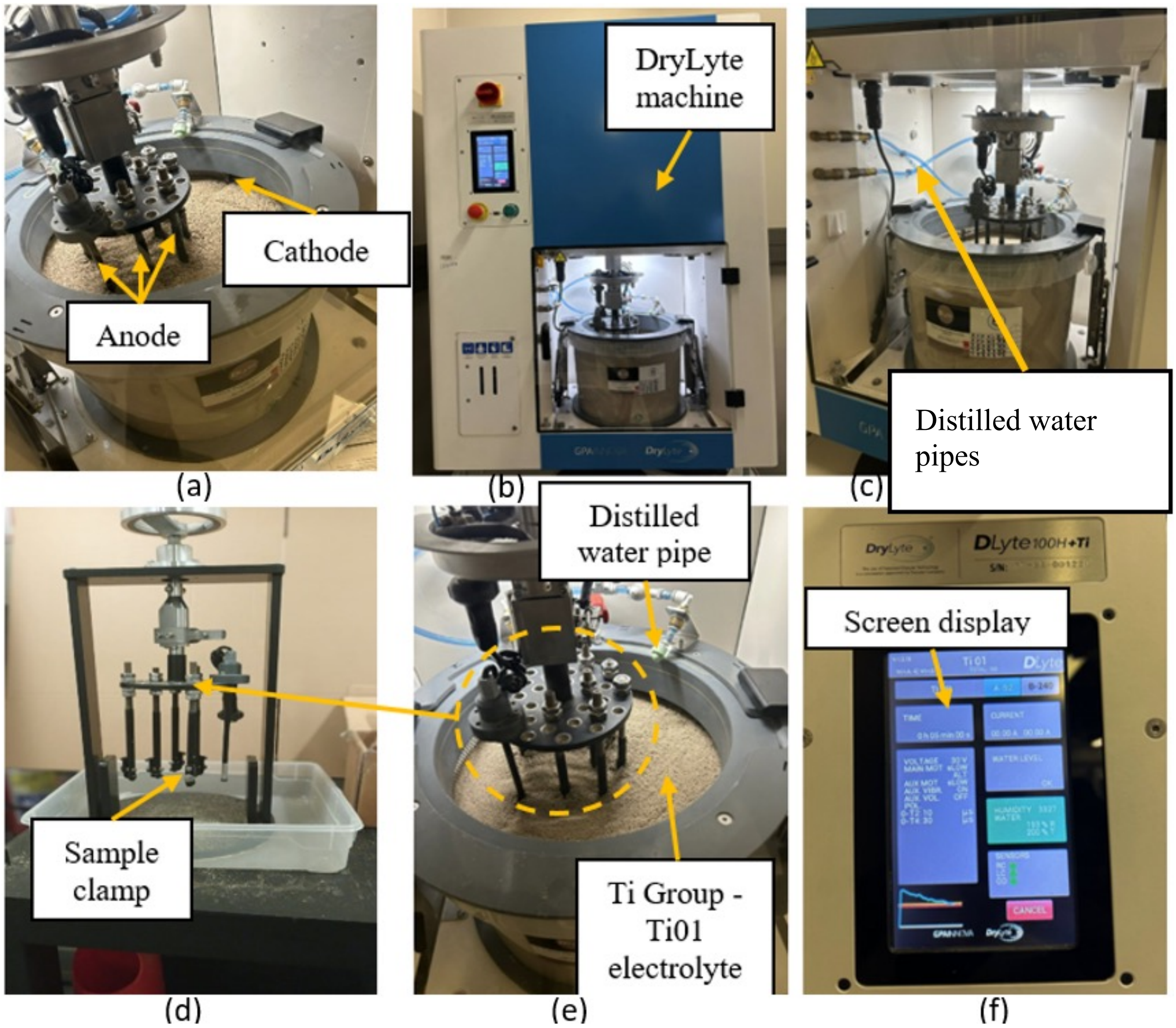

Figure 27: Drylyte electropolishing machine

Table 16: DryLyte electropolishing electrolyte media

Electrolyte	**Material**
Co-Cr Group – Co-Cr01	Co-Cr alloys
Co-Cr Group – Co-Cr02 (only for mirror finishing and complex geometries)	Co-Cr alloys
SS Group – SS01	Stainless steel alloys
SS Group – SS02 (only for mirror finishing and complex geometries)	Stainless steel alloys
Ti Group – Ti01	Nitinol and titanium alloys

3.5.2. Chemical polishing method

The samples underwent a cleaning process with acetone, ethanol, and distilled water in an ultrasonic bath following the dry electropolishing method and were subsequently dried using compressed air. Once the cleaning process was completed, surface roughness measurements and morphology were taken. The same samples that were designated for dry electropolishing were then utilized for chemical polishing. Hydrofluoric acid (HF) and nitric acid (HNO_3) were used as the chemical polishing solution.

The use of a mixture of HF and HNO_3 is a standard technique for enhancing the surfaces of metals such as stainless steel and titanium as well as alloy materials. HF functions as the main etchant, effectively attacking oxides and the surface of the material, while HNO_3 acts as an oxidizer, facilitating uniform dissolution and mitigating localized etching. It also contributes to the passivation of the surface.

The effectiveness of the polishing process was assessed based on the duration of polishing. Chemical polishing was conducted on vertical, horizontal, and semispherical samples using a solution with an initial HF concentration of 4 M and an HNO_3 concentration of 3.17 M as recommended by (Bezuidenhout *et al.*, 2020). Chemical polishing of samples was performed using one solution composition per duration. The initial nitric acid concentration $[HNO_3]_0$ was kept constant at 3.17 M, and the initial HF concentration $[HF]_0$ was kept at 4 M.

The setup for the process is illustrated in **Error! Reference source not found.**. The total volume of 650 ml of etchant solutions was prepared in high-density polyethylene (HDPE) containers with a capacity of 1 000 ml, which were then placed in an ice bath within a secondary polypropylene (PP) container. The polishing solution was stirred magnetically at 400 rpm. Three specimens were polished simultaneously in the HDPE containers, resulting in a total of three samples for each composition. The specimens were suspended using HDPE strings attached to the lid for safe handling, and no fresh acid was added, nor was the etchant volume intentionally reduced during the polishing process. The temperature of the solution was recorded after each polishing duration.

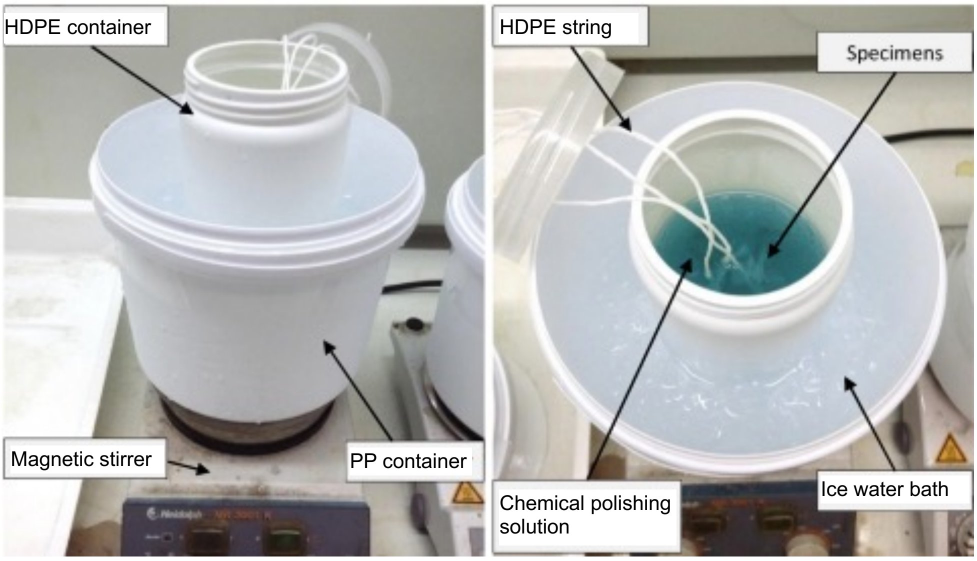

Figure 28: Chemical polishing process setup

3.6. Experiments with surface finishing

Since the samples were categorized into zones 1 through 9 based on the direction of powder and Ar supply to evaluate the impact of location on surface roughness, each vertical or horizontal sample was segmented into four sections as indicated by the orange dotted line in Figure 29. One section was examined in its as-built state while the remaining three underwent surface finishing processes, including dry electropolishing or a combination of dry electropolishing with chemical polishing.

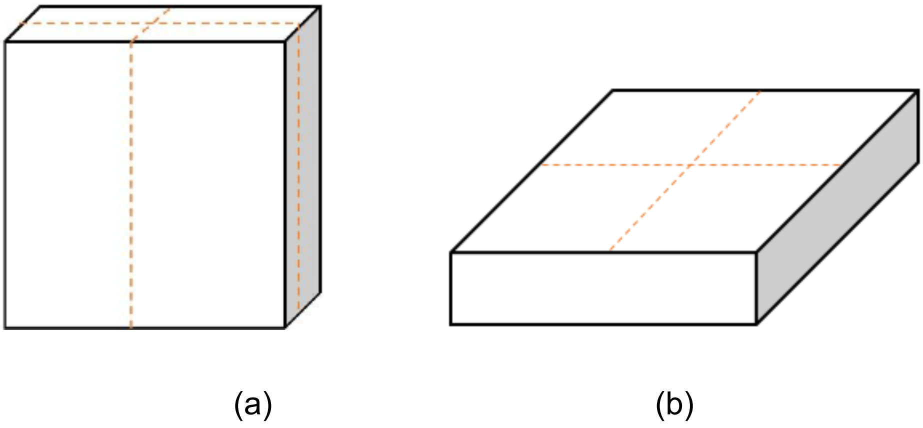

Figure 29: Vertical (a) and horizontal sample segmentation (b)

Specific vertical samples from selected zones were designated for the dry electropolishing surface finishing process with regard to the Ar inlet and outlet as well as the powder recoater “start” and “end” regions: Zone 1 – Sample 36, Zone 3 – Sample 1, Zone 5 – Sample 21, Zone 7 – Sample 44, and Zone 9 – Sample 12.

Each of these samples was cut as indicated by the orange dotted line in Figure 29. One part was examined in its as-built state, while the other three underwent a surface finishing process using dry electropolishing and then followed by chemical polishing. The vertical samples (side surfaces) were polished according to the specifications outlined in Table 17.

Table 17: Surface finishing of the vertical sample by dry electropolishing

Zone	**Sample No**	**Duration of processing**
1	36	30 minutes 60 minutes 120 minutes
3	1	
5	21	
7	44	
9	12	

The selected horizontal samples from the main zones with regard to the Ar inlet and outlet, as well as powder recoater “start” and “end” regions, included Zone 1 – Sample 41, Zone 3 – Sample 8, Zone 5 – Sample 27, Zone 7 – Sample 45 and Zone 9 – Sample 5. The polishing of the horizontal samples was conducted in accordance with the specifications outlined in Table 18.

Table 18: Surface finishing of the horizontal sample by dry electropolishing

Zone	**Sample No**	**Duration of processing**
1	41	30 minutes 60 minutes 120 minutes
3	8	
5	27	
7	45	
9	5	

The semisphere samples were selected based on the supply direction for both powder and Ar to evaluate the impact of location on surface roughness. The following semisphere samples from key zones were designated for the surface finishing process: Zone 3 – Samples 1a, 2a, and 3a, Zone 5 – Samples 4a, 5a, and 6a, and

Zone 7 – Samples 7a, 8a, and 9a. The polishing of the samples was carried out as outlined in Table 19.

Table 19: Electropolishing of semisphere samples

Zone	**Sample No**	**Duration of processing**
3	1a, 2a, 3a	30 minutes 60 minutes 120 minutes
5	4a, 5a, 6a	
7	7a, 8a, 9a	

A chemical polishing was performed using a solution of HF and HNO_3. Three specific zones were identified: Zone 3, which is located near both the Ar inlet and the area where the powder coating commences; Zone 5, situated in the middle; and Zone 7, positioned far from both the Ar inlet and the powder distribution initiating area. The samples were chemically polished as outlined in Table 20.

Table 20: Surface finishing of Ti6Al4V ELI samples by chemical polishing

Chemical Polishing Using HF-HNO3 Solutions				
Zones	**Dry electropolished semisphere**	**Dry electropolished vertical (side surface)**	**Dry electropolished horizontal (top surface)**	**Duration of chemical polishing**
3	3 semispheres Samples 1a, 2a, 3a	3 vertical bars Sample 1	3 horizontal bars Sample 8	5 minutes 10 minutes 20 minutes
5	3 semisphere Samples 4a, 5a, 6a	3 vertical bars Sample 21	3 horizontal bars Sample 27	5 minutes 10 minutes 20 minutes
7	3 semisphere Samples 7a, 8a, 9a	3 vertical bars Sample 44	3 horizontal bars Sample 45	5 minutes 10 minutes 20 minutes

3.7. Summary

This chapter provides a brief summary of the tools, measuring techniques, and analysis instruments, along with the powdered Ti6Al4V material used in this research. Furthermore, it details the experimental framework and the surface-finishing techniques applied in this study.

CHAPTER 4: RESULTS AND DISCUSSION

4.1. As-built surfaces

4.1.1. Rectangular (vertical and horizontal) samples

Appendix 3 and Figure 30–Figure 32 illustrate the average surface roughness (Ra, Rq, and Rz) values along with their variances and standard deviations for side A, side B, and the upper surfaces of the as-built horizontal and vertical Ti6Al4V samples produced by L-PBF. The sample that exhibited the highest profile Ra for side A was vertical sample 12, which was situated near the Ar discharge and close to the onset of powder delivery (Zone 9).

Conversely, the vertical sample nearest to the Ar inlet (vertical sample 3) demonstrated the least surface irregularity. For side B, vertical sample 42, positioned on the opposite side of the powder distribution initiation area, showed the most significant irregularity (Zone 4). Overall the average surface roughness of vertical samples was slightly greater than that of horizontal samples. This increase in roughness can be attributed to the longer heating duration of vertical samples which facilitates greater adherence of powder particles. Additionally, the measurement orientations for both vertical and horizontal samples differed; horizontal samples were assessed perpendicular to the building direction, whereas vertical samples were evaluated parallel to it.

The side surface morphology of samples produced using L-PBF is influenced by their layered structure, which may feature valleys along the scan trace and powder particles attached to the edges. When the profilometer stylus moves parallel to the layer it tends to yield a lower measurement of surface roughness compared to when measured in the perpendicular direction.

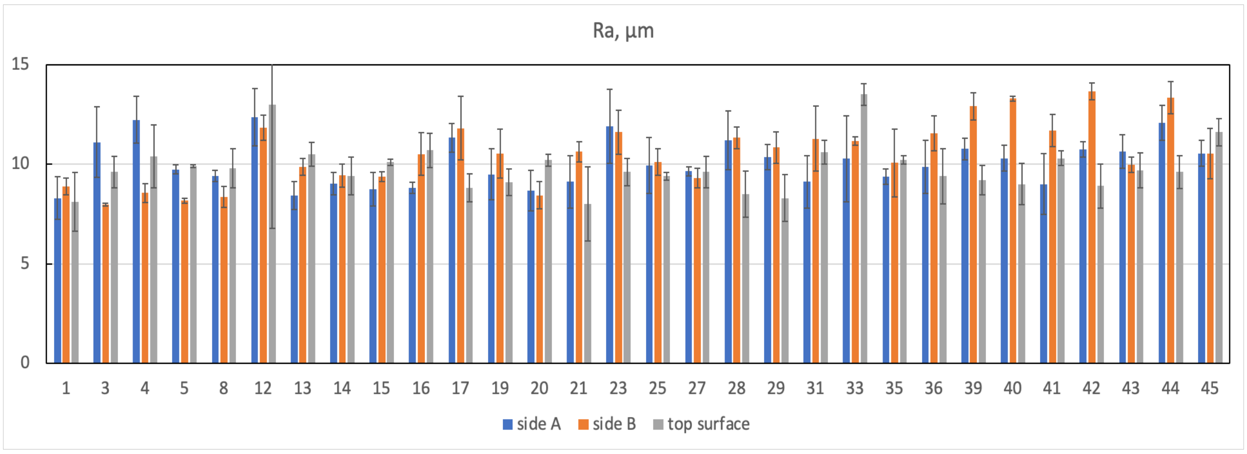

Figure 30: Average roughness (Ra) for side A, side B, and top surface of the samples

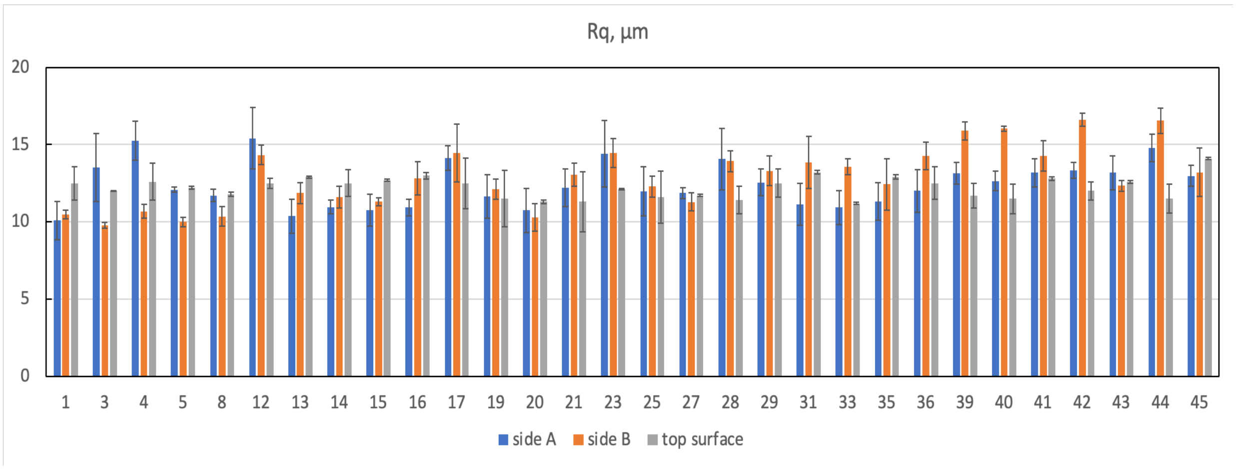

Figure 31: Root means square (Rq) of side A, side B, and top surface of the as-built samples

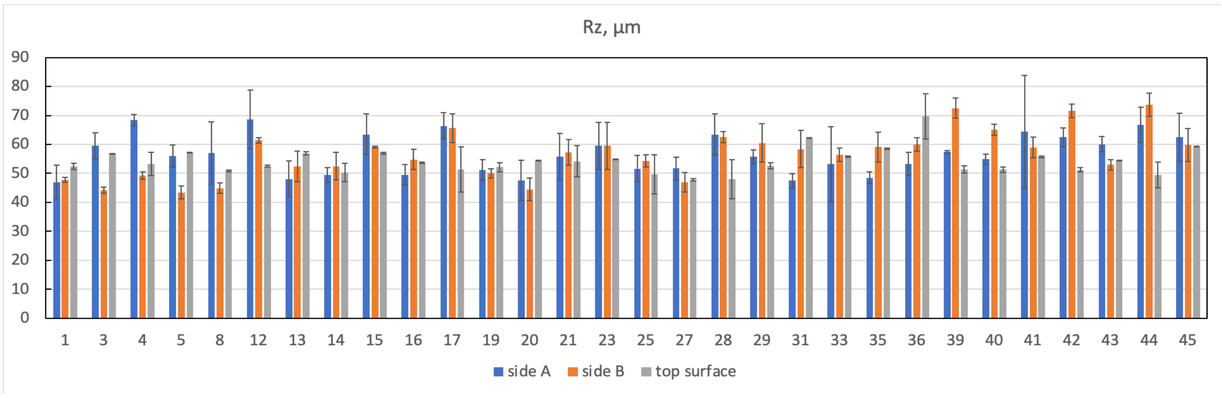

Figure 32: Ten-point height (Rz) of side A, side B, and top surface of the as-built samples

To ensure that the investigations were not influenced by the outcomes of profile tests, the average surface roughness for Zones 1 through 9 were determined based on all vertical and horizontal samples within specified zones (see Figure 16 for zone specifications). In zones located on the opposite side of the substrate from the initial powder dispersal (Zone 1) and at the center (Zone 5), the surface roughness Ra for vertical samples was found to be higher on side B compared to side A with this difference being statistically significant (t-test, $p<0.05$). In zones 4 and 7, the Ra values on side B exhibited notable differences with standard deviations of 2.05 and 1.55 µm respectively, resulting in a statistically insignificant difference at the chosen p-value ($p < 0.05$). Conversely, in areas closer to where particle deposition commenced, side A demonstrated greater roughness in Zone 6 ($p < 0.05$) and Zone 9. Zone 3 had the lowest surface irregularity, as determined by the profilometer.

The average Ra roughness for the upper surfaces was recorded at 9–10 µm for upper surface, which is consistent with findings reported by Yadroitsev *et al*, (2021). Rz values varied between 50 and 70 µm, peaking in Zone 7 (Figure 35), while the minimum Rz was noted on the surface of Zone 3 samples. A statistically significant difference ($p < 0.05$) was observed in the average Rz roughness of the upper surface in Zone 3 compared to Zones 1, 5, 6, and 9, where Rz values were higher.

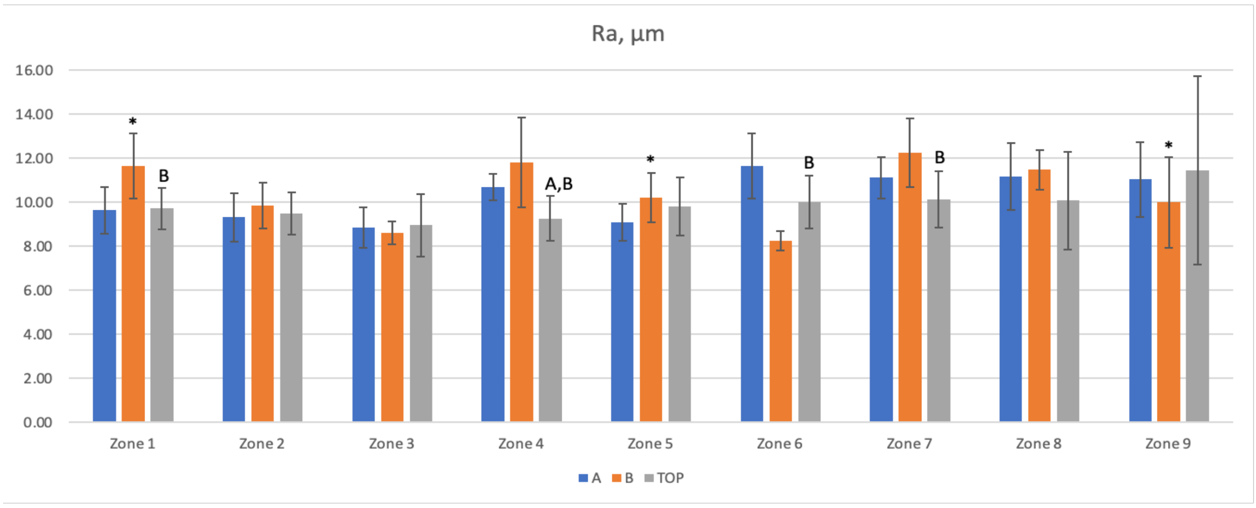

Figure 33: Average roughness (Ra) of side A, side B, and top surface per zone of as-built samples

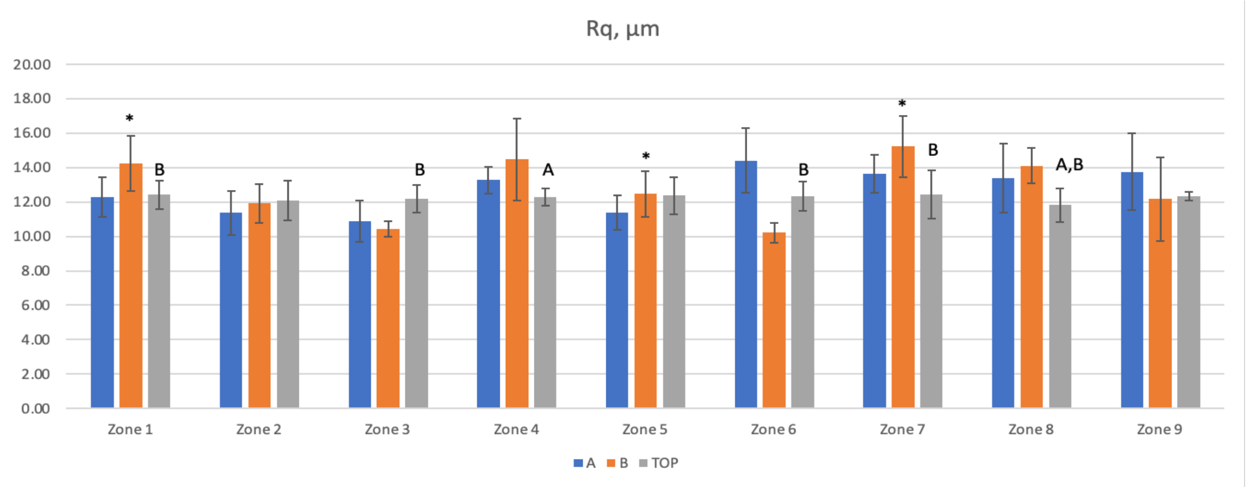

Figure 34: Root means square (Rq) of side A, side B, and top surface per zone of the as-built samples

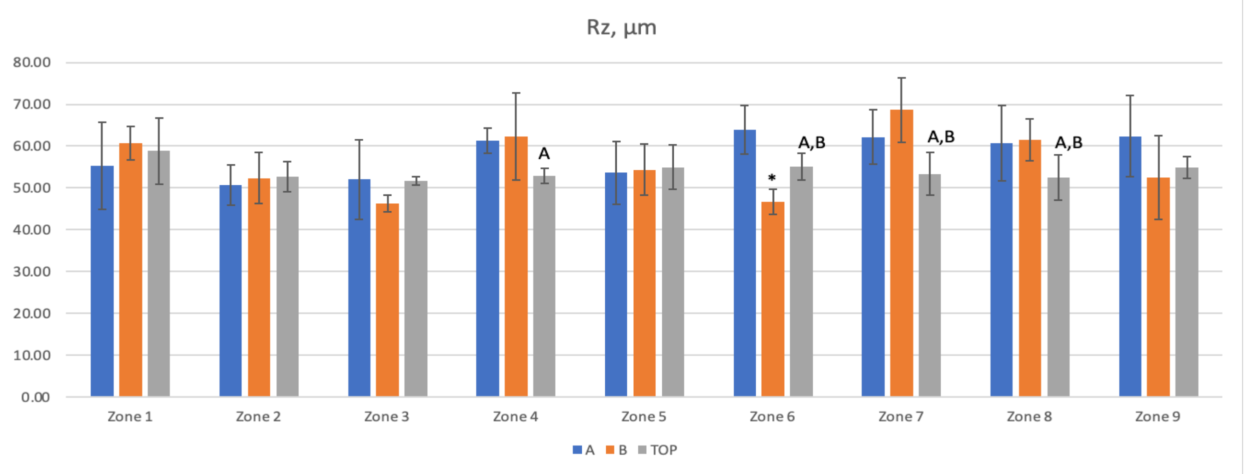

Figure 35: Ten-point height (Rz) of side A, side B, and top surface per zone of the as-built samples

Figure *36* shows the morphology of the side surface of the as-built Ti6Al4V sample produced by L-PBF. The characteristics of this surface primarily arise from the powder particles that adhere to it and cover the side surface as a coat. As the sample was produced through contouring, the vertical surface exhibits a relatively smooth finish. SEM analysis of the sample morphology indicated that the size of the adhered powder particles varies across different zones. The zone nearest to the initiation of powder recoating contains residual fine particles. Zone 3, as shown in Figure 36a, features finer partially molten particles and is positioned closer to the powder commencement and the Ar inlet. In contrast, Zone 7 in Figure 36c, contains larger-size powder droplets compared to Zone 3, and is situated further from the powder commencement and located at the Ar discharge point; zone 7 is also at the Ar discharge point.

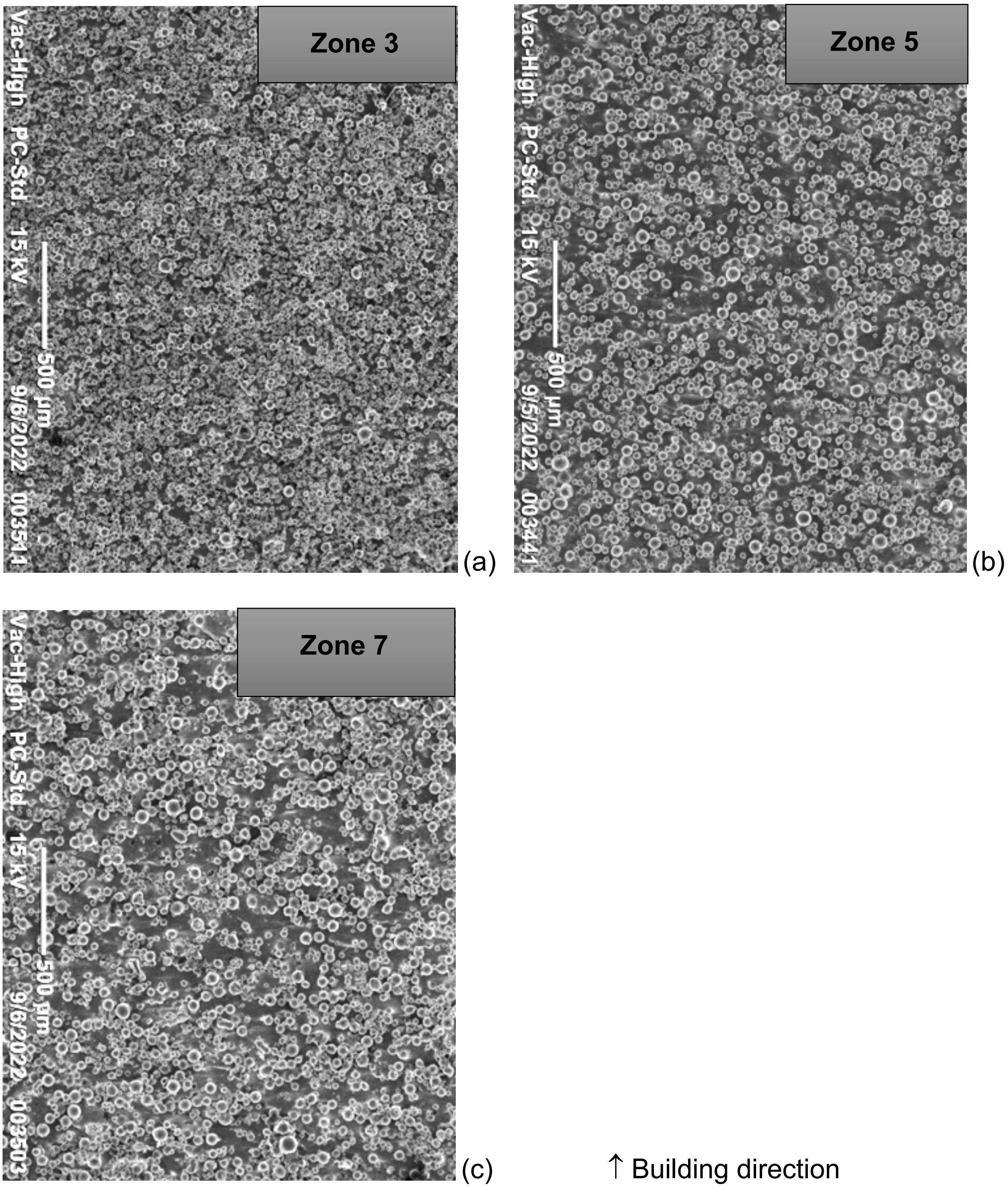

↑ Building direction

Figure 36: SEM photo of side surfaces A of vertical samples from Zone 3 (a), Zone 5 (b), and Zone 7 (c)

Zone 5 in Figure 36b is a mid-zone and has bigger partially molten particles than Zone 3 but less than Zone 7. This variation is attributed to the swaying and rolling phenomena that occur during the powder spreading process, as noted by Pal *et al.*, (2021). The difference in surface roughness between Zone 3, Zone 6, and Zone 9 can be attributed to the combined effects of powder delivery and shielding gas flow. Zone 3 is positioned near both the powder delivery commencement and the argon gas inlet. The proximity to the inlet ensures a more efficient removal of spatter and vaporized material from the melt pool, thereby reducing the likelihood of redeposition on the surface. This contributes to the relatively smoother finish observed in Zone 3.

In contrast, Zone 6 and Zone 9 are located farther from the argon inlet. Although they are still close to the powder delivery start, the effectiveness of gas shielding is reduced in these regions. As the argon flow progresses across the build plate, its velocity and ability to sweep away particles diminishes, which can lead to increased turbulence, entrainment of spatters, and redeposition of partially melted particles. These effects increase surface irregularities, explaining why Side A of Zone 6 and Zone 9 exhibited higher roughness compared to Zone 3.

The combination of adhering and partially melted powder particles, along with the morphology of the layer from the contouring track, contributes to the pronounced surface irregularity observed on the side surfaces of the samples. Figure 37 illustrates the sample from which the morphology of an individual layer can be assessed. Each layer consists of overlapping single tracks (the core) accompanied by a contouring track. While the melt pool incorporates powder particles, those that adhere do not have adequate time to fully melt; a significant number are only partially melted due to the rapid cooling that occurs at high scanning speeds. A metallurgical bond forms between the vertical surface and the adhering powder particles while the laser melts the powder. During this process, powder particles situated closer to the edge of the melt pool may be drawn into it. The likelihood of a powder particle completely or partially dissolving increases with its proximity to the energy source. Once the melt pool cools and solidifies, the adjacent unmelted powder particles bond to the surface especially on the side which enhances the roughness of the surface. Additionally, spattering contributes to these surface irregularities. The surface topography of the L-PBF sample is significantly impacted by the presence of partially melted powder, overlapping tracks, ripples, and contours.

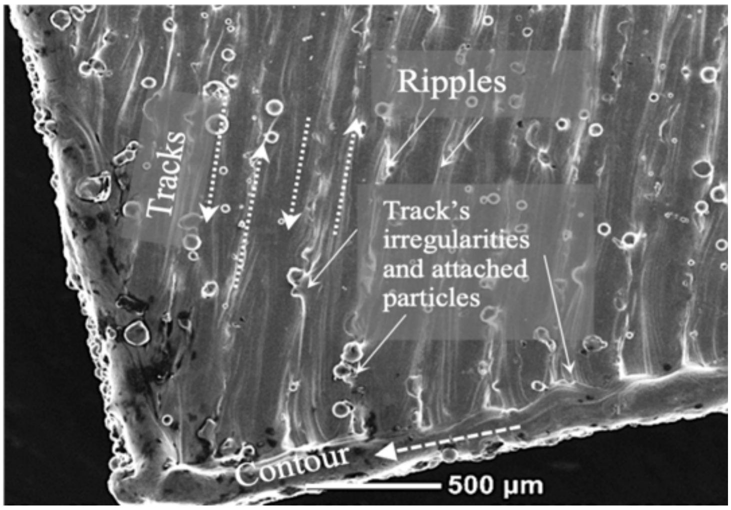

Figure 37: Top surface of the LPBF samples showing single-layer morphology

The surface irregularity at the top of the as-built Ti6Al4V parts produced by L-PBF is a result of track-by-track formation, ripple formation, and powder particle attachment. The track-by-track process generates peaks and valleys that can lead to a wavy appearance. When surface tension applies a shear force on the liquid, ripples emerge along the track (Simson *et al*., 2022). The surface irregularity of the L-PBF is not only affected by the particles of powder that adhered to the surface as a result of elevated local temperature and spattering but ripples and track formation also contribute to the surface roughness. However, the particles attached to the top surface of as-built samples vary slightly by zone regarding the start of powder spreading; the zones where powder spreading begins have fewer attached powder particles than those farther away from the powder spreading initiation and the Ar inlet. Zone 3 in Figure 38a has fewer attached powder particles than Zones 5 and 7, as it is situated closer to where the powder spreading starts and the Ar inlet. Although these differences between zones are minor, they indicate that local build conditions, such as powder flow direction and gas dynamics, can influence on top-surface quality in L-PBF components.

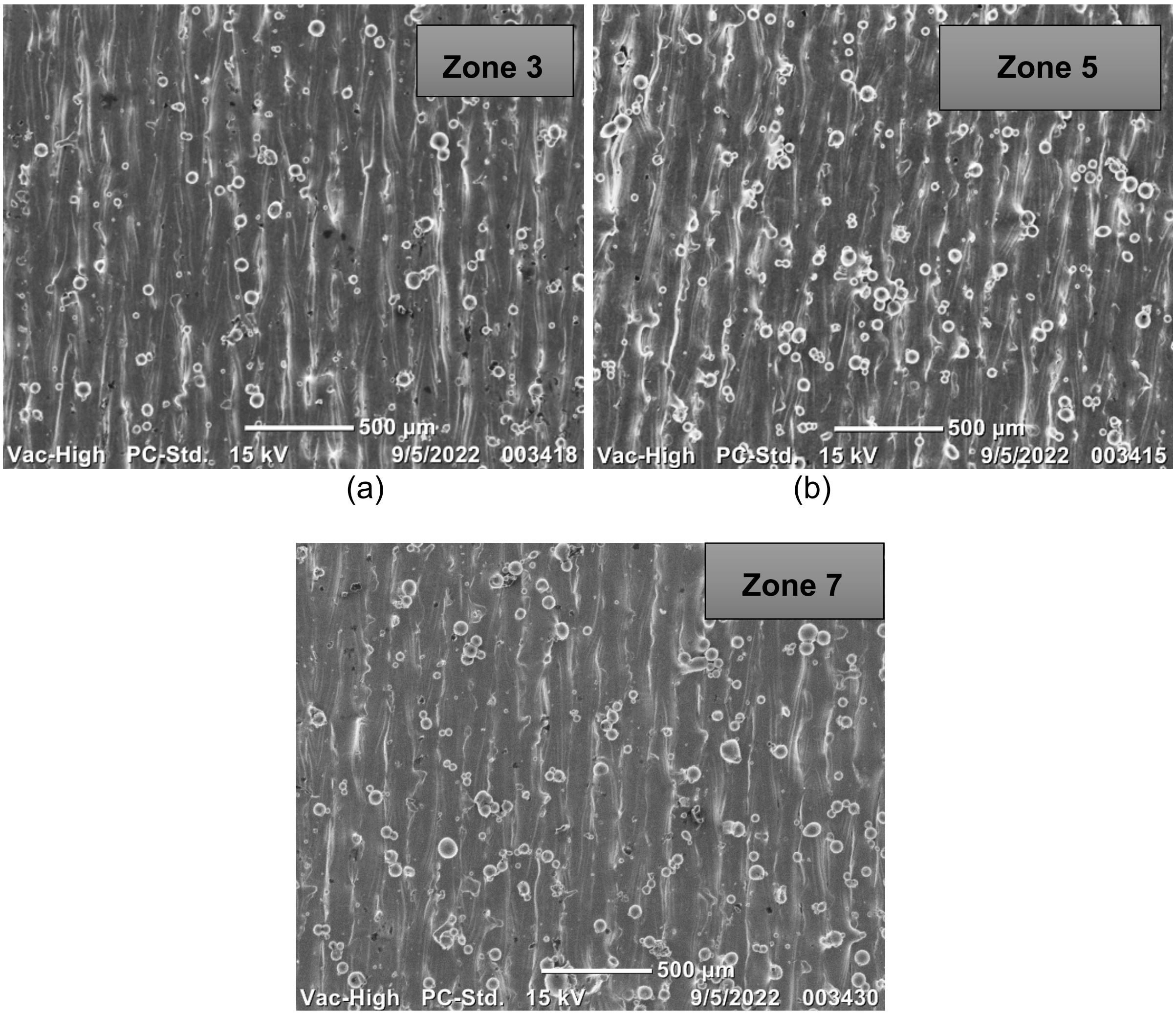

(a) (b)

(c)

Figure 38: SEM photo of the top of horizontal samples from Zone 3 (a), 5 (b), and 7 (c)

Zones 5 and 7 in Figure 38b and Figure 38c have more large-sized powder droplets than Zone 3, and they are located far from where the powder spreading commences. Zone 7 is also at the Ar discharge inlet. Zone 5 is a mid-zone and has more large-sized particles than Zone 3 in Figure 38b. This is due to the swaying and rolling phenomenon during powder spreading, as stated by Pal et al., (2021).

4.1.2. Semisphere samples

Appendix 3.3 and Figures 39-41 illustrate the average surface roughness (Ra, Rq, and Rz) values and their standard deviations for the near-top semisphere samples. Among these, Sample 38 (Zone 7), situated near the Ar discharge inlet at the far end of the building tray from the start of the powder recoating, exhibited the highest Ra measurement for the near-top semisphere samples. Conversely, the semisphere sample closest to the Ar inlet and the beginning of the powder recoating was designated as Sample 2 in Zone 3. The measurements of the semisphere samples were taken perpendicular to the building direction. The side surface morphology of the L-PBF samples is influenced by the layered structure, which incorporates staircases as well as particles of powder that adhere to the sides.

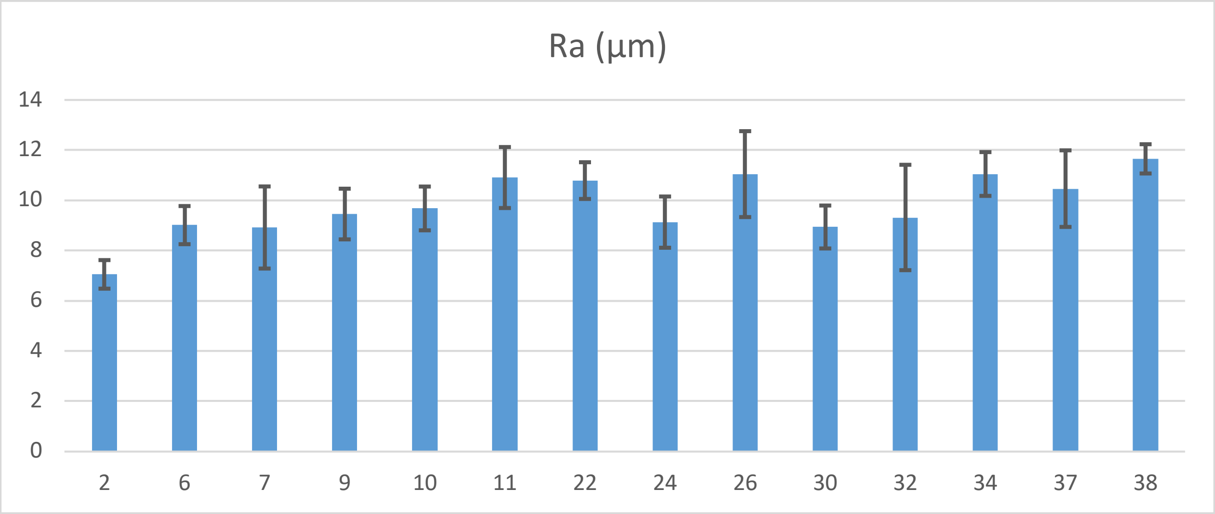

Figure 39: Average roughness (Ra) of the as-built semisphere sample (measured near the top of the sample)

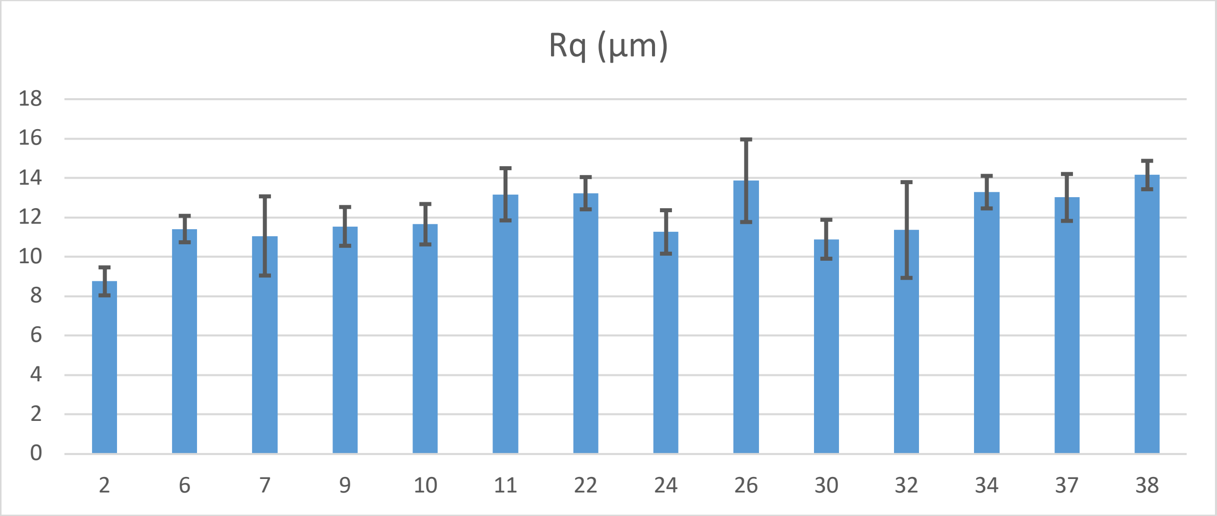

Figure 40: A root means square (Rq) of the as-built semisphere sample (measured near the top of the sample)

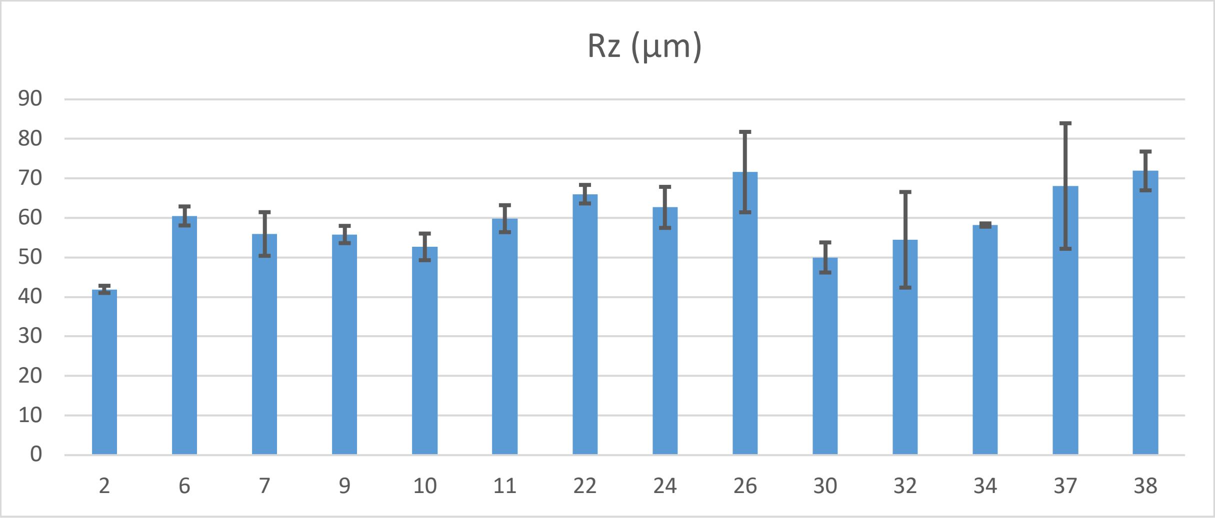

Figure 41: Ten-point height (Rz) of the as-built semisphere samples (measured near the top of the sample)

To ensure the investigations were not influenced by the results of profile tests, the average surface roughness for Zones 2 through 9 based on all semisphere samples within a designated area was determined. In the zones located opposite the start of powder dispersal (specifically Zone 4 and Zone 7), the average surface roughness (Ra) was found to be higher than that of the zones near the start of powder dispersal (Zone 3, Zone 6, and Zone 9) and this difference was statistically significant (t-test, $p < 0.05$). Examining the inlet and outlet of the Ar, the Ra of zones located near the Ar outlet (i.e., Zones 7–9) exceeded that of zones near the Ar inlet (i.e., Zone 2 and Zone 3), with this variation also being statistically significant (t-test, $p < 0.05$). Conversely, for surfaces situated closer to the point of particle deposition, a different trend was noted as the ten-point height roughness (Rz) values ranged from 48 to 70 µm, peaking in Zone 7 – see Figure 44v– while the lowest Rz was recorded at the surface of Zone 3 samples. There was a statistically significant difference in the ten-point Rz between zones near the start of the powder recoating and those located towards the end of the building tray (t-test, $p < 0.05$).

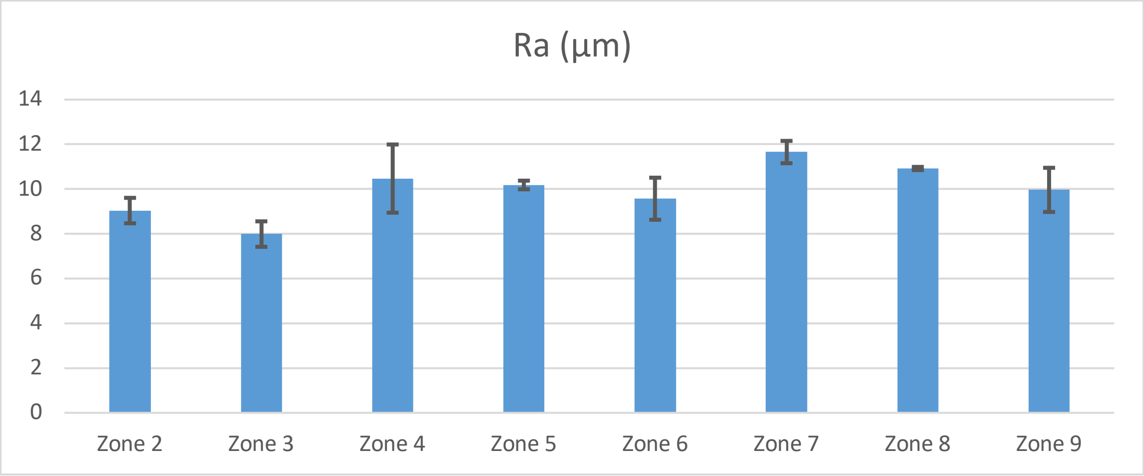

Figure 42: Side average roughness (Ra) of the as-built semisphere per zone

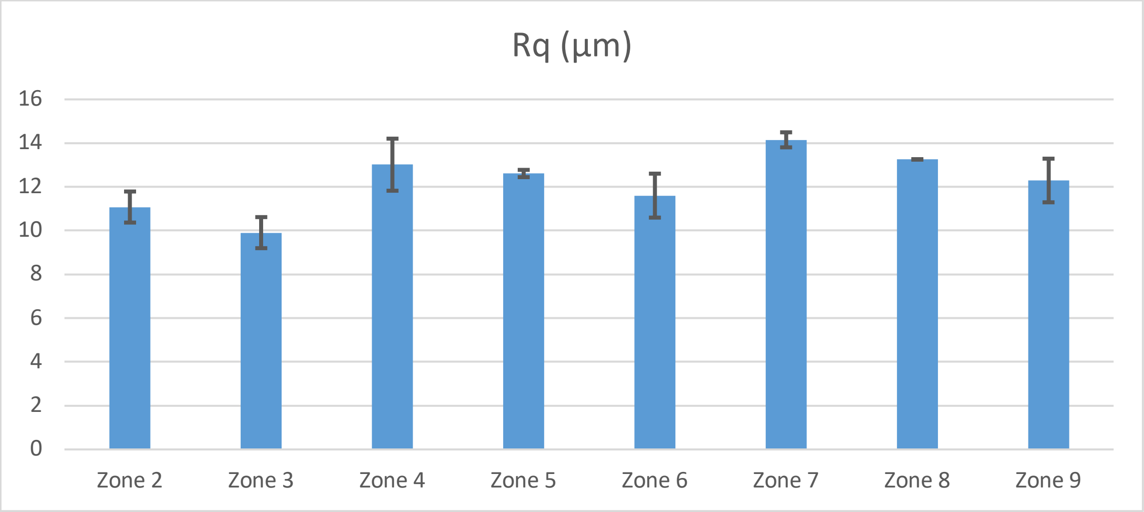

Figure 43: Side root means square (Rq) of the as-built semisphere per zone

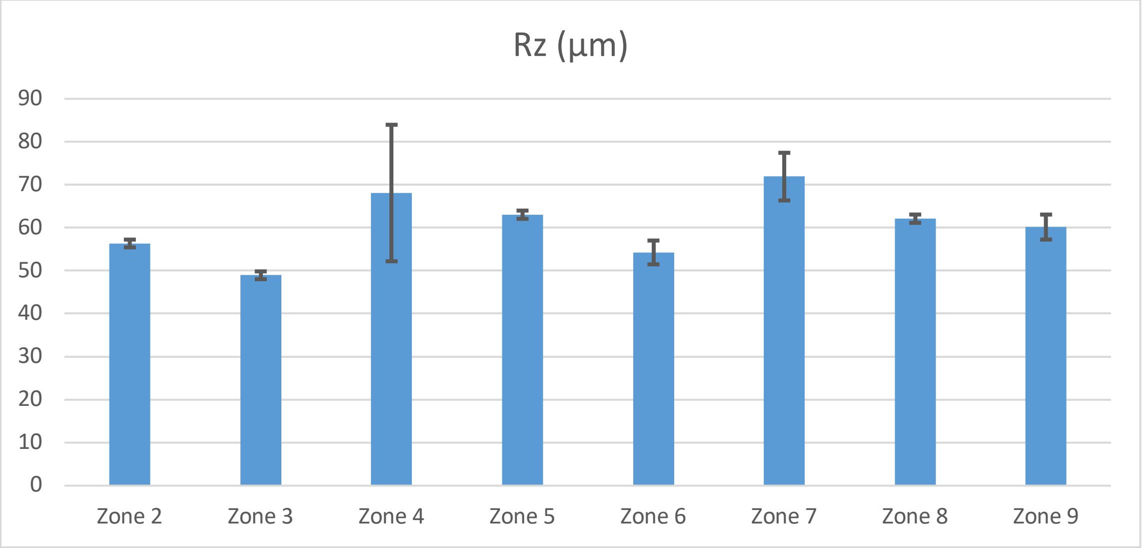

Figure 44: Side ten-point height (Rz) of the as-built semisphere per zone

L-PBF fabricates components incrementally forming stair-step patterns on inclined surfaces. These staircases contribute to the surface irregularities observed in the curved components produced via L-PBF (Kumar *et al.,* 2015). Figure 45 illustrates the perspective of a sample from which the characteristics of a top semisphere surface can be analyzed. The presence of partially melted powder particles adhered to the surface of the semispherical sample along with the stair-step layers, uneven paths and profiles of each layer, significantly influences the surface roughness of the as-built curved L-PBF parts.

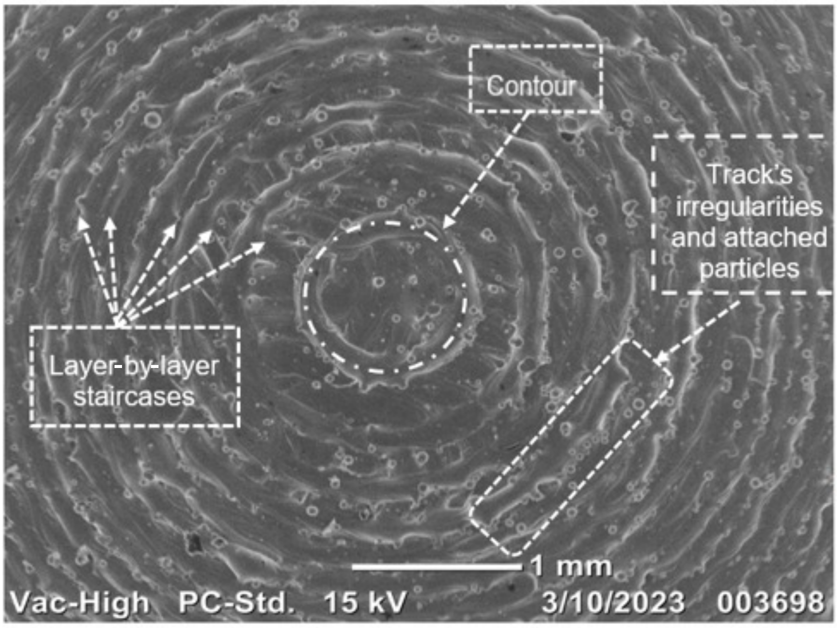

Figure 45: Typical top surface morphology of semisphere sample

Figure 46 illustrates the top surface morphology of the semispheres from Zones 3, 5, and 7. Each of the semisphere samples, regardless of the zone, displays a layer-by-layer staircase structure, and partially melted powder particles, contours, and irregularities in tracks are evident. These staircases, along with the attached particles, contours, and track inconsistencies, as shown in Figure 46a-c, play a role in the surface roughness of the curved components produced by L-PBF, as also found by Shange *et al*., (2019). However, the size and quantity of particle adhesion differs by zone. Zone 3, which is closer to the powder delivery system and Ar inlet, accounts for the reduced number of adhered powder particulates compared to Zone 5 and 7 in Figure 46b and Figure 46c, which are located far from both the Ar inlet and the powder recoater commencement and have more and larger-sized affixed powder particulates than the zones located near the powder recoater commencement. Zone 5 exhibits some droplets of powder particles; however, the number of attached particles is greater than in Zone 3. This is due to the swaying and rolling of the powder, as stated by Pal *et al.*, (2021).

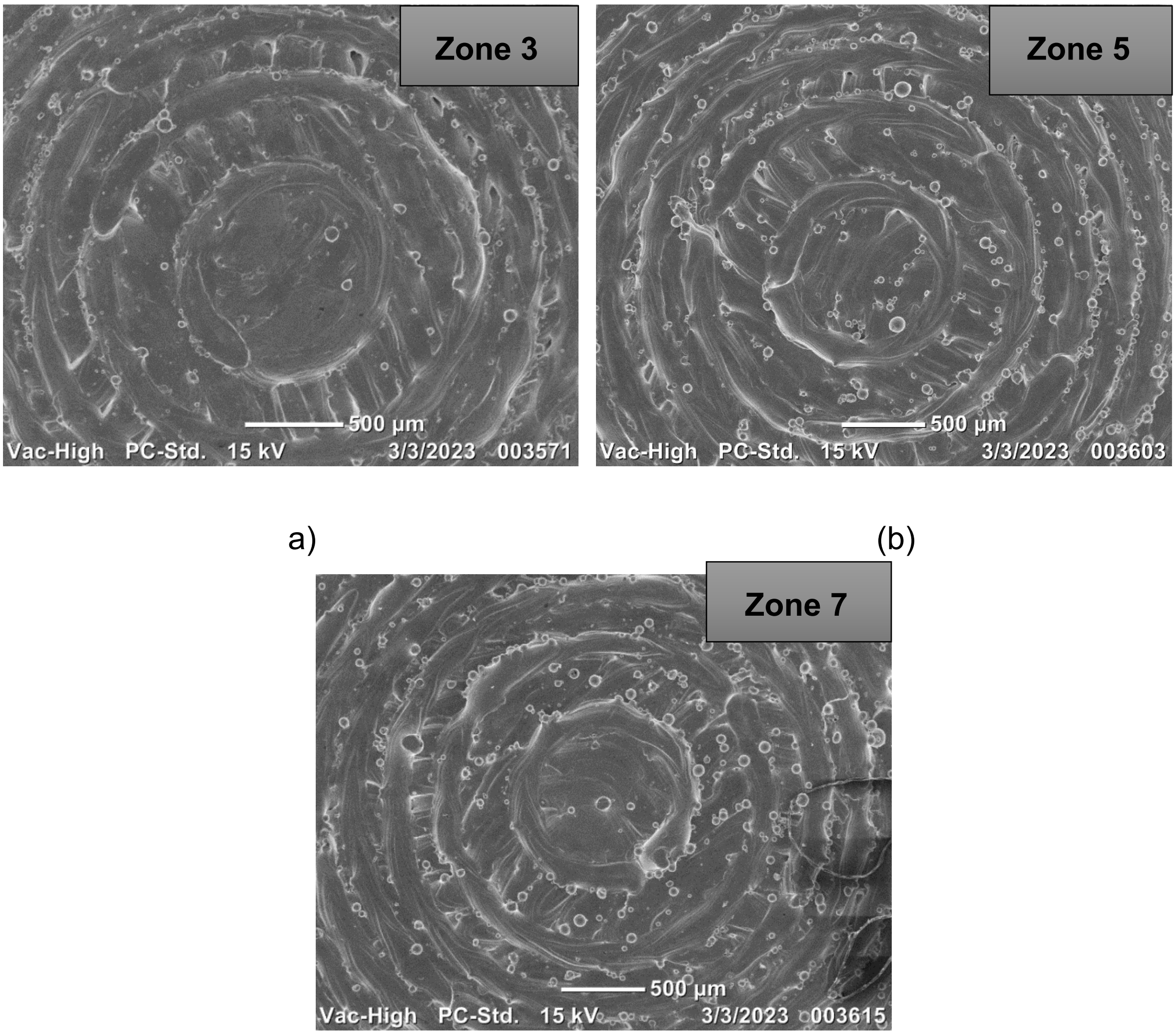

a) (b)

(c)

Figure 46: SEM photo of the top surface of the semisphere from Zone 3 (a), 5 (b), and 7 (c)

Figure 47 illustrates the view of the side surface of a semisphere sample for an assessment of the morphology of an individual stratum. It depicts partially attached particles of various sizes, small, medium, and large, as well as irregular shapes, along with peaks and valleys. The irregularities on the semispherical side surface are attributed to these partially attached particulates and surface inconsistencies. According to Rech *et al.*, (2023), vibrations caused surface irregularities (peaks and valleys) during L-PBF processing.

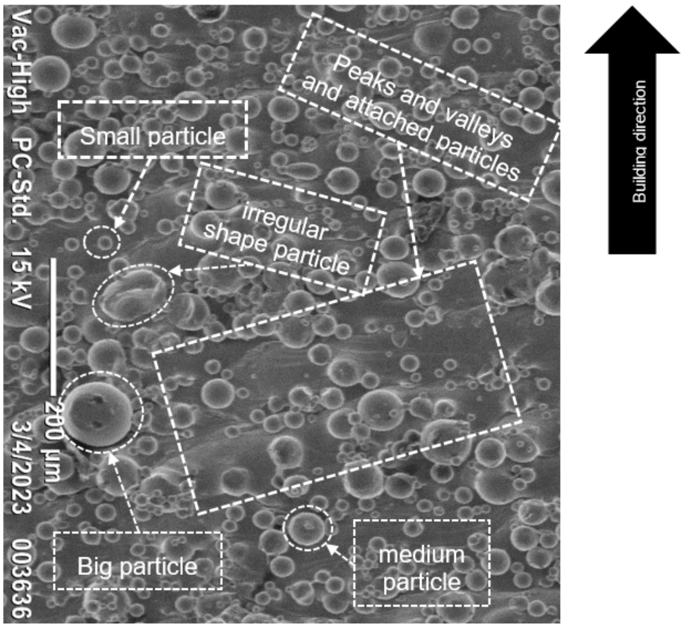

Figure 47: Side surface morphology of the semisphere

As illustrated in Figure 48, the analysis focused on the surface morphology of the as-fabricated side surface of semispheres in Zones 3, 5, and 7. The findings indicate that the side surfaces of these semi-spherical samples exhibit both adhered powder particles and peaks and valleys in all the zones. Research has shown that these adhered particles, along with the uneven surface features, significantly contribute to the roughness observed in components produced by L-PBF (Sendino *et al.*, 2023). Notably, the nature of the adhered powder particles varies by zone. In Zone 3, as seen in Figure 48a smaller-sized particles are prevalent compared to those in Zones 5 and 7. Zone 5 contains particles of both small, medium, and larger particles. In Zone 7, depicted in Figure 48c, large particles are more prominent, attributable to the filtering effect of larger particles at the end of the construction tray, which is located further from the Ar inlet, a phenomenon also reported by Pal *et al.*, (2021).

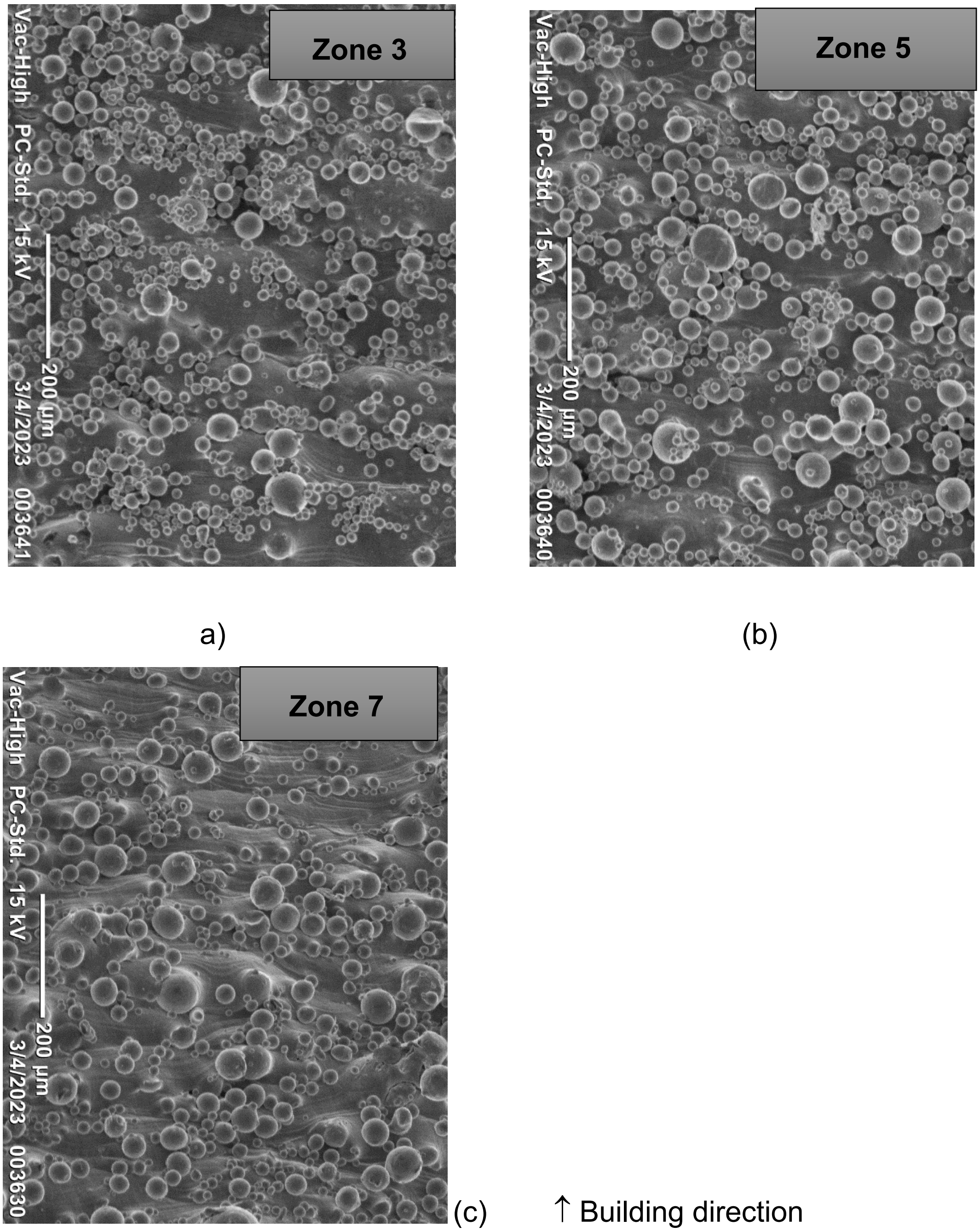

a)

(b)

(c)

↑ Building direction

Figure 48: SEM photos at 200 μm scale of the side surface of the semisphere from Zone 3 (a), 5 (b), and 5 (c)

4.1.3. Conclusion

- The top surface roughness of the as-built Ti6Al4V samples produced by L-PBF (top surface) is significantly influenced by track-by-track formation, ripple formation, and powder particle attachment positioning with regard to the Ar inlet and outlet as well as the powder distribution start and end regions on the building plate.

- The side surface roughness of the as-built Ti6Al4V samples produced by L-PBF is primarily influenced by powder particles that adhere to it and also positioning with regard to the Ar inlet and outlet, as well as the powder distribution start and end regions on the bulding plate.
- The surface roughness of the as-built curvey or inclined surface Ti6Al4V samples produced by L-PBF is primarily influenced by staircase effect, powder particle attachment, track irregularities and positioning with regard to the Ar inlet and outlet as well as the powder distribution start and end regions on the building plate.
- As measured by the profilometer, side surface roughness was slightly greater than that of top surfaces. This increase in roughness can be attributed to the longer heating duration of side surfaces which facilitates greater adherence of powder particles.
- The surface roughness of the samples placed at the Ar inlet and powder distribution start regions shows a reduced surface roughness compared to samples placed far/opposite the Ar inlet and powder distribution start regions regardless of the sample shape.
- The surface roughness of the as-built samples shows a higher surface roughness compared to that of the implants' required surface roughness regardless of the placement with regard to the Ar inlet and outlet, as well as powder distribution start and end areas on the building plate and optimum process parameter. This higher surface roughness necessitates post-processing to attain the surface finishing required for medical implants.

4.2. Surface roughness of L-PBF dry electropolished samples

4.2.1. Surface roughness of rectangular samples after dry electropolishing

Figure 49 to Figure 51 show the surface roughness of the side and top surfaces for both as-built samples and those subjected to dry electropolishing. The mean and standard deviation of surface roughness (Ra, Rq, and Rz) for the side and top surface before and after surface finishing are detailed by zone. It is evident across all zones that surface roughness decreases with longer polishing durations during dry electropolishing. Specifically polishing for 30 minutes yields the least reduction in Ra while a duration of 120 minutes results in the most significant reduction. This trend whereby Rq and Rz exhibit similar behavior to Ra is also illustrated in Figure 49 and Figure 50. No notable differences were detected between zones located further from or closer to the Ar inlet and the initiation point of powder delivery, as all zones demonstrated a consistent decrease in surface roughness over time regardless of their position on the building plate. Given that time is the primary variable considered, polishing for 120 minutes proved to be the most effective at minimizing the surface roughness of horizontal and vertical samples as shown in the percentage reduction in Figure 52. As shown previously, the highest surface roughness for as-built samples was observed in Zones 7 and 9, which are situated near the Ar outlet, while the lowest roughness values were recorded for samples near the Ar inlet and the start of the powder recoater in Zone 3. After 30 minutes of polishing, a statistically significant decrease in Ra values was noted for samples from Zones 7 and 9 (t-test, $p < 0.05$). Additional polishing for 60 minutes was found to be particularly effective for samples from Zones 9 and 3. Notably, samples from Zone 3 exhibited the best surface roughness in both top and side measurements after 120 minutes of polishing – achieving Ra values between 6.8–7.4 µm compared to 9.8–8.9 µm in their as-built condition. Overall polishing for 120 minutes was effective in decreasing surface roughness across all samples.

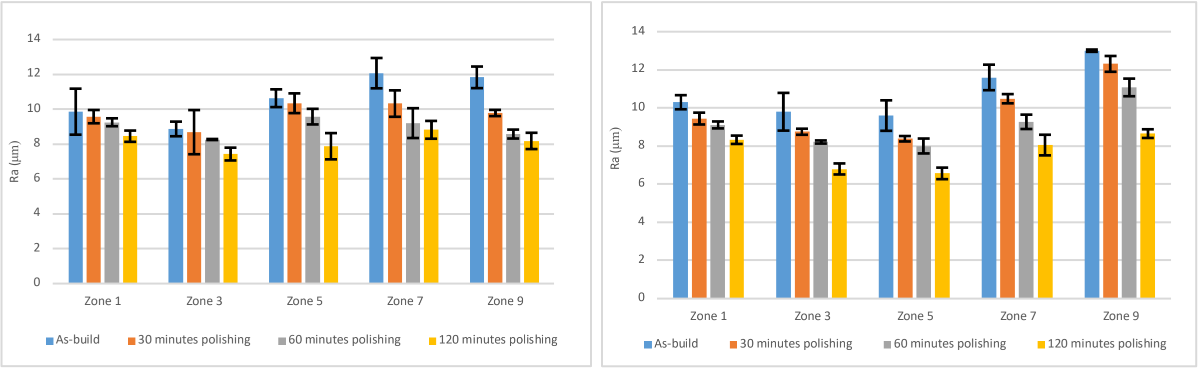

(a) (b)

Figure 49: Ra values for side (a) and top (b) surfaces of as-built and after dry electropolishing finishing for periods (30, 60, and 120 minutes)

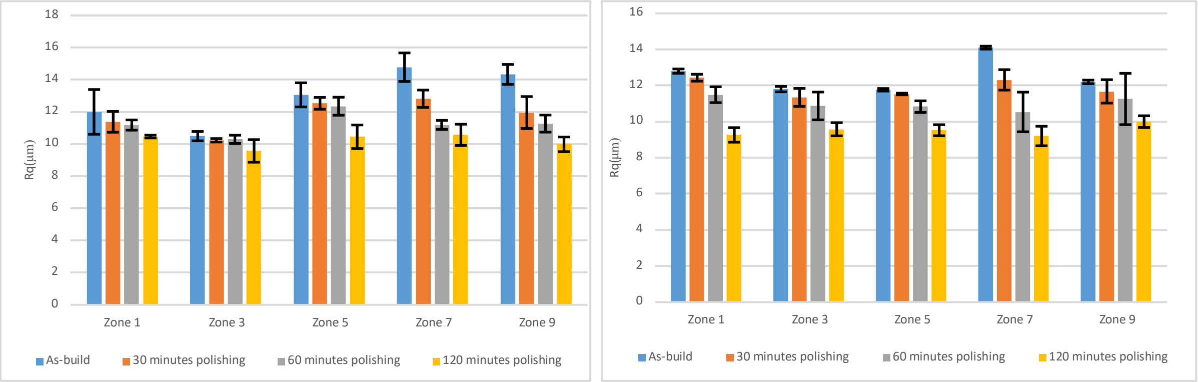

(a) (b)

Figure 50: Rq values for side (vertical) (a) and top (horizontal) (b) surfaces of as-built and after dry electropolishing finishing periods (30, 60, and 120 minutes)

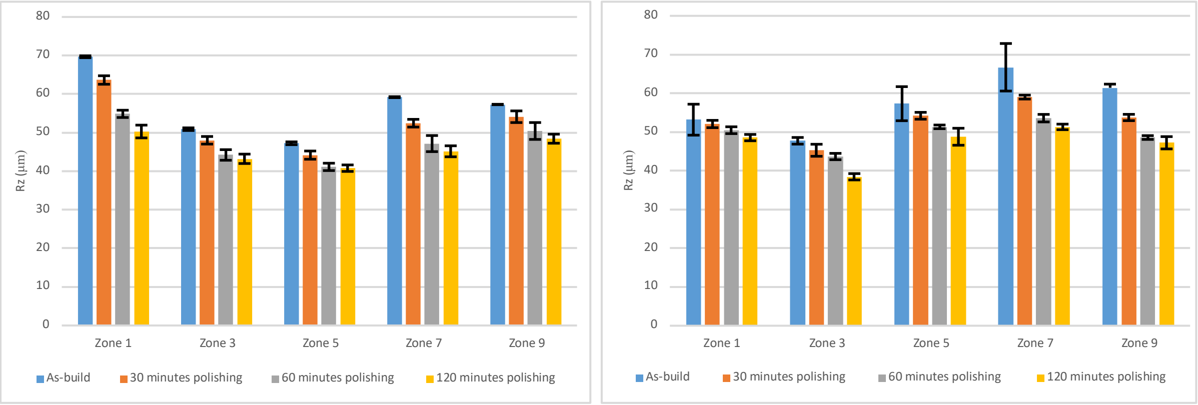

(a) (b)

Figure 51: Rz values for side (vertical) (a) and top (horizontal) (b) surfaces of as-built and after dry electropolishing finishing periods (30, 60, and 120 minutes)

To examine how time affects surface polishing through dry electropolishing, the percentage loss of surface roughness for each zone during various polishing periods was calculated from the as-built conditions. The percentage loss associated with each polishing period is shown in Figure 52–Figure 54. It was observed that the loss of Ra varies with time across all zones; as polishing time increases, the Ra loss also escalates. Specifically, polishing for 30 minutes resulted in the lowest percentage loss of Ra, while polishing for 120 minutes resulted in the greatest loss, as highlighted in Figure 52. This indicates a direct relationship where an increase in surface polishing time correlates with a greater loss of Ra. Similarly, the metrics Rq and Rz exhibit trends analogous to that of Ra, as seen in Figure 53 and Figure 54.

In all the zones, particularly for both vertical and horizontal samples, the pattern remains uniform, the percentage of loss increases with extended polishing periods regardless of the specific zone on the building plate. Zone 9 exhibited the most significant Ra loss for both vertical and horizontal samples, recording losses of 30.83% and 33.45%, respectively, after 120 minutes of polishing. In contrast, Zone 3 experienced the least loss with a mere 2.08% reduction for vertical samples after 30 minutes, as shown in Figure 52a. The smallest Ra reduction for horizontal surfaces was also noted in Zone 9, which recorded a loss of 5.33% after 30 minutes of polishing, as shown in Figure 52b.

Figure 53a indicates that the vertical samples in Zone 3 had the lowest Rq loss at 1.88% after 60 minutes, while the horizontal samples show the least reduction in Rq in Zone 5, recording a 1.98% decrease after 30 minutes, as seen in Figure 53b. Furthermore, among the horizontal samples, Zone 7 demonstrated the highest Rz loss at 27.83% in Zone 1 after 120 minutes, whereas Zone 9 had the smallest Rz reduction, showing only a 5.54% loss after 30 minutes. This detail is illustrated in Figure 54b. Whereas Zone 9 also had the highest Rz loss for vertical samples, recording 23.11% after 120 minutes, while the least loss was noted in Zone 1, with a reduction of 2.09% after 30 minutes of polishing (Figure 54a).

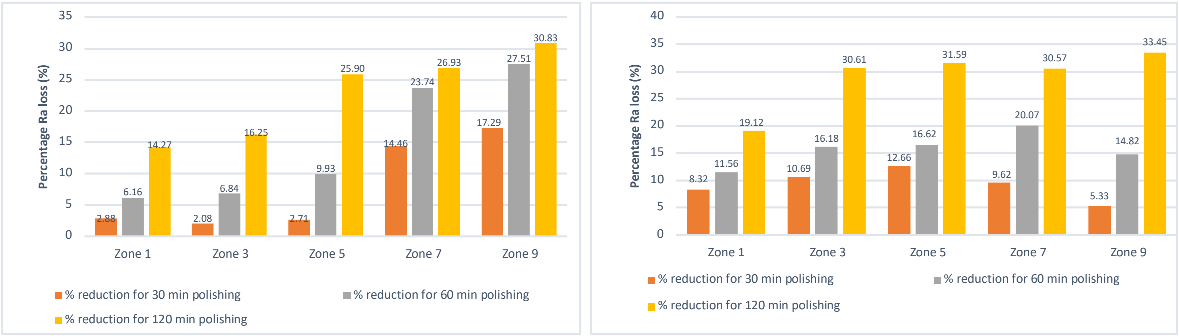

(a) (b)

Figure 52: Ra reduction percentage for side (vertical) (a), and top (horizontal) (b) surface per zone for each polishing period

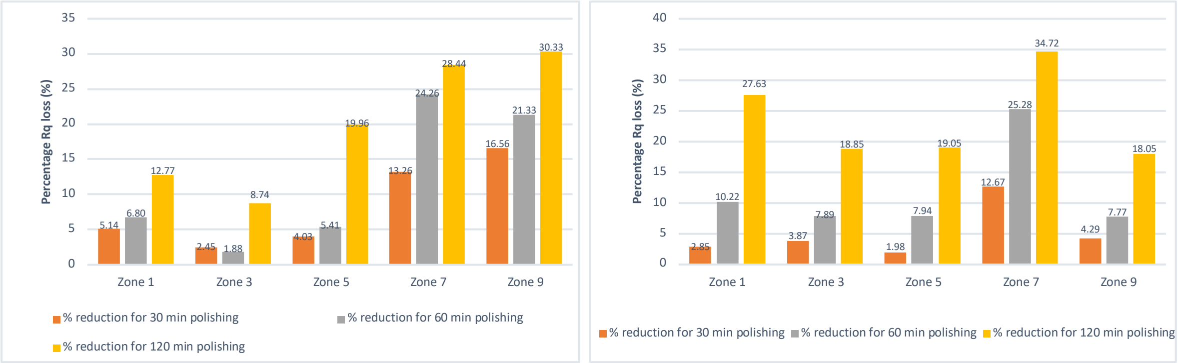

(a) (b)

Figure 53: Rq reduction percentage for side (vertical) (a), and top (horizontal) (b) surface per zone for each polishing period

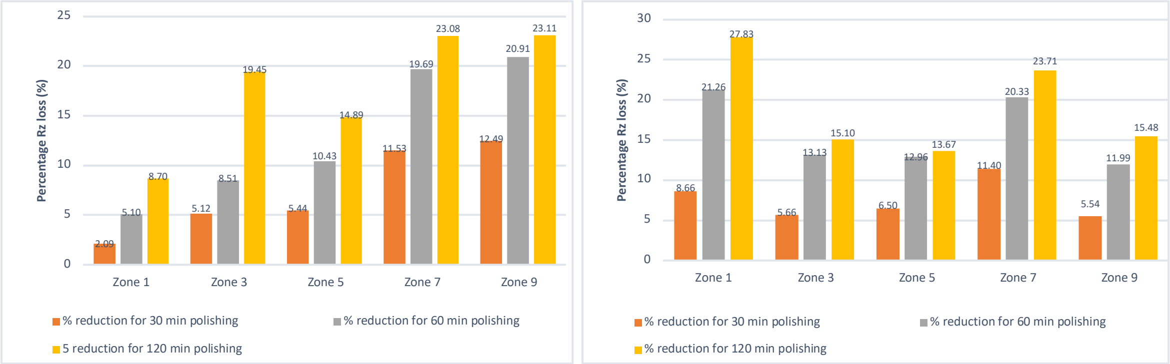

Figure 54: Rz reduction percentage for side (vertical) and top (horizontal) surface per zone for each polishing period

4.2.2. Morphology of top surfaces after dry electropolishing

SEM micrographs illustrating the surface characteristics of the top surface (horizontal samples) as-built samples and those subjected to dry electropolishing for durations of 30, 60, and 120 minutes are presented in Figure 55. As the polishing time increased, a notable decrease in surface roughness was observed. In Figure 55a, the as-built horizontal samples displayed a significant presence of partially sintered powder particles and tracks. However, after 30 minutes of polishing (Figure 55b), these particles were largely removed, although some peaks and valleys, tracks, and remnants of the partially sintered powder remained visible. The surface treated for 60 minutes (Figure 55c), exhibited the initial signs of a more uniform smoothing effect, yet some particles and tracks were still apparent, albeit with improved conditions compared to both the as-built and 30-minute polishing samples. The samples polished for 120 minutes (Figure 55d) showed marked improvement with a substantial reduction in partially sintered powder and a smoother surface compared to those polished for 30 and 60 minutes, achieving a roughness reduction of 33.45% from the as-built state. When comparing the SEM morphology and roughness measurements, there is clear agreement: both techniques confirm that the 120-minute treatment delivers the most effective improvement. However, the data also highlight that the rate of enhancement diminishes with longer durations, with the most noticeable gains occurring between the as-built state and the 60-minute treatment, while subsequent improvements (60 to 120 minutes) are more gradual.

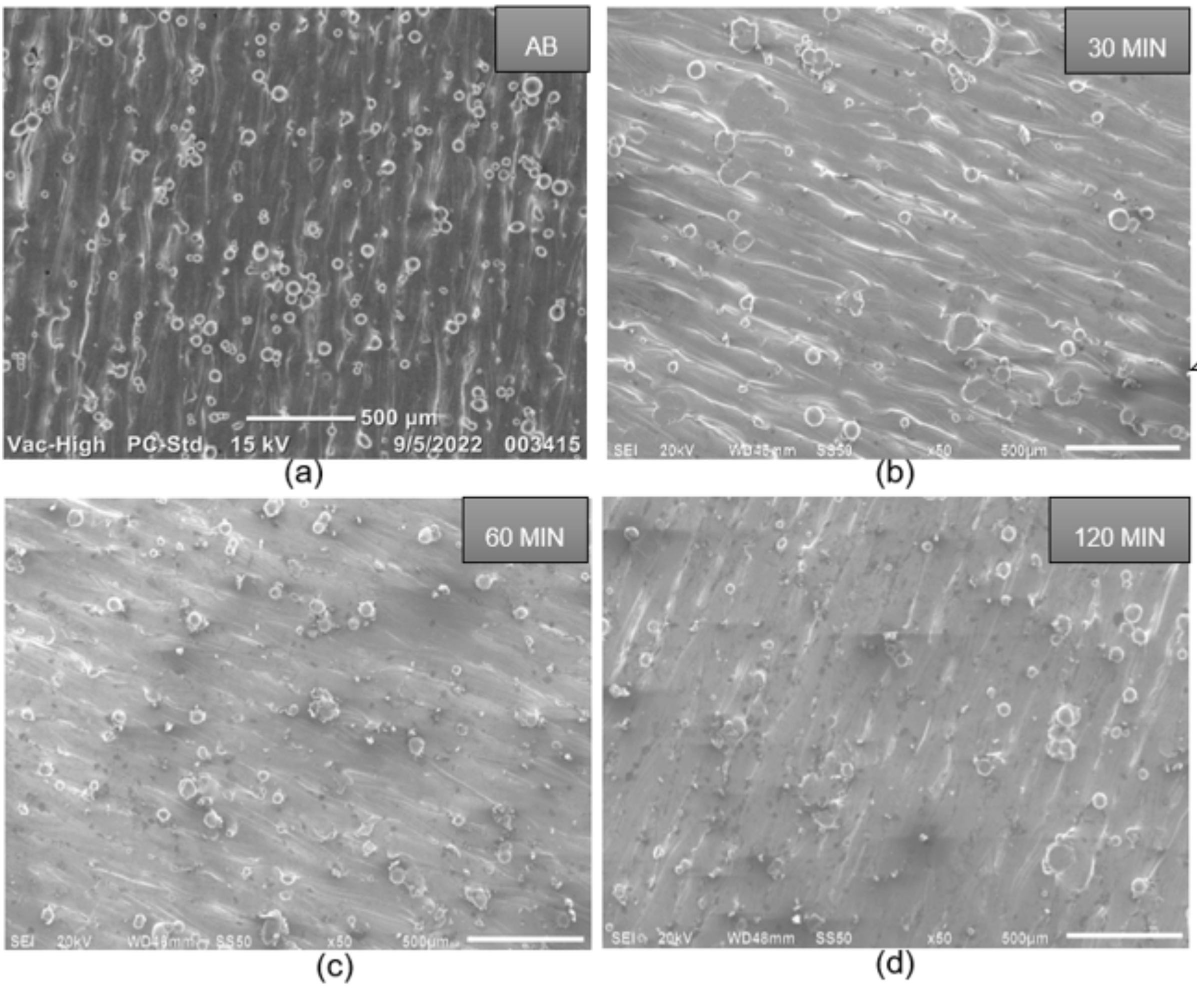

Figure 55: SEM micrographs of horizontal (top) surfaces of L-PBF-produced Ti6Al4V ELI samples in a) as-built (AB), b) 30 min, c) 60 min, and d) 120 mi dry electropolishing

4.2.3. Morphology of side surfaces after dry electropolishing

SEM micrographs of the side surface (vertical samples) samples of as-built and those subjected to 30, 60, and 120 minutes of dry electropolishing are presented in Figure 56a–d. As the polishing duration increases, there is a significant decrease in the size of the partially sintered powder. In Figure 56a, the surface of the as-built vertical sample is predominantly covered with particles of partially sintered powder.

For the sample polished for 30 minutes (Figure 56b), there is minimal enhancement compared to the as-built sample, as particles of partially sintered powder remain clearly visible. The surface treated for 60 minutes (Figure 56c) shows the initial signs of a uniform smoothness with a greater presence of smaller partially sintered powder particles compared to both the as-built and the 30-minute polishing sample.

After 120 minutes of polishing (Figure 56d) a substantial improvement is noted over the as-built sample with further reduction in the size of the partially sintered powder particles. The surface polished for 120 minutes exhibits a smoother texture than those polished for 30 and 60 minutes, with a roughness reduction of 30.83% compared to the as-built surface.

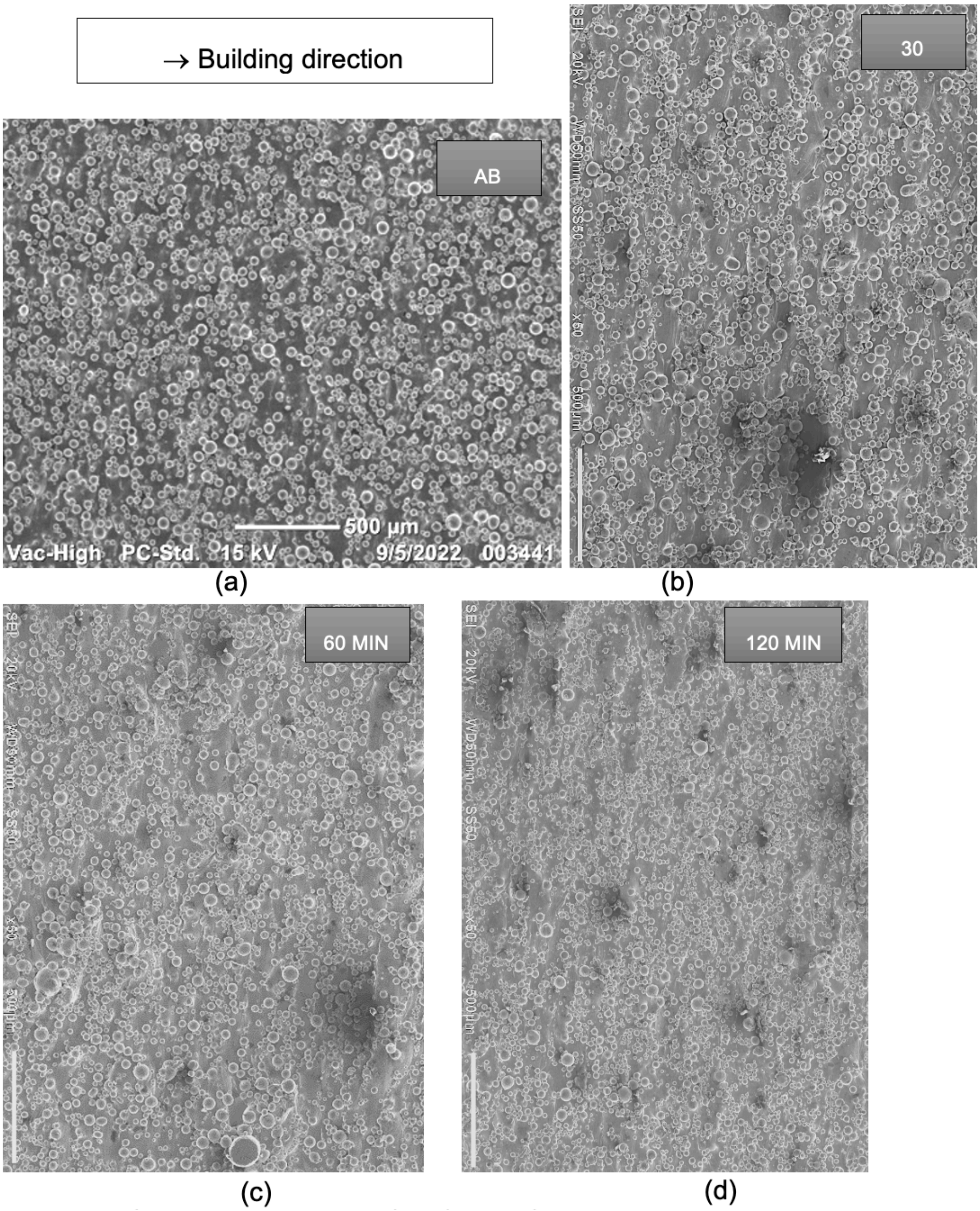

Figure 56: SEM micrographs of surfaces of vertical samples L-PBF-produced Ti6Al4V ELI samples in a) as-built, b) 30 min, c) 60 min, d) 120 min polishing conditions

4.2.4. Dry electropolishing of semisphere samples

The mean and standard deviation of surface roughness (Ra, Rq, and Rz) for the semisphere samples, both pre- and post-surface finishing, are detailed by zone in

Figure 57, Figure 58, and Figure 59. Observations indicate that as polishing time increases, surface roughness consistently decreases across all zones. Specifically, polishing for 30 minutes results in the least reduction in Ra, while a duration of 120 minutes yields the most significant Ra reduction. This trend is similarly reflected in the Rq and Rz measurements, as illustrated in Figure 58 and Figure 59.

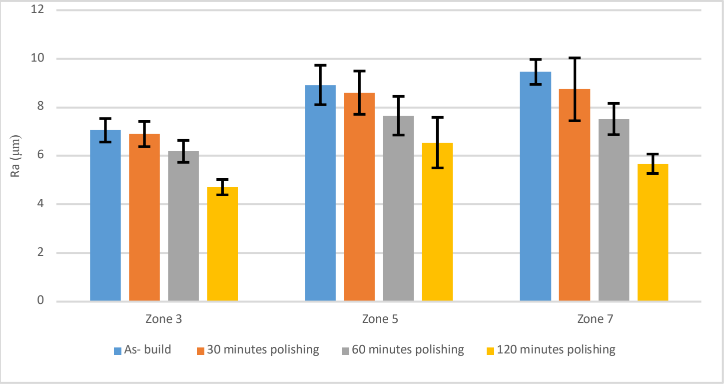

Figure 57: Ra values for semisphere surfaces of as-built and after dry electropolishing finishing periods (30, 60, and 120 minutes)

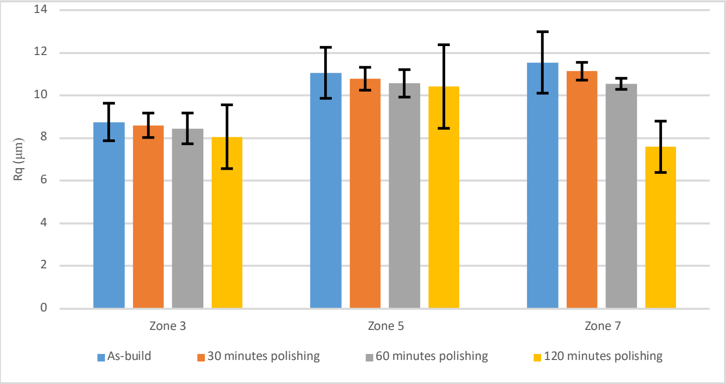

Figure 58: Rq values for semisphere surface of as-built and after dry electropolishing finishing periods (30, 60, and 120 minutes)

Notably, zones situated far from the Ar inlet and the point of powder delivery do not exhibit any significant differences compared to those located closer to these points. Overall, regardless of their position on the building plate, all zones show a decrease in surface roughness with extended polishing time. Given that time is the primary factor considered, polishing for 120 minutes proves to be the most effective method for minimizing the surface roughness of the semispheres, as indicated by the percentage reductions shown in Figure 60.

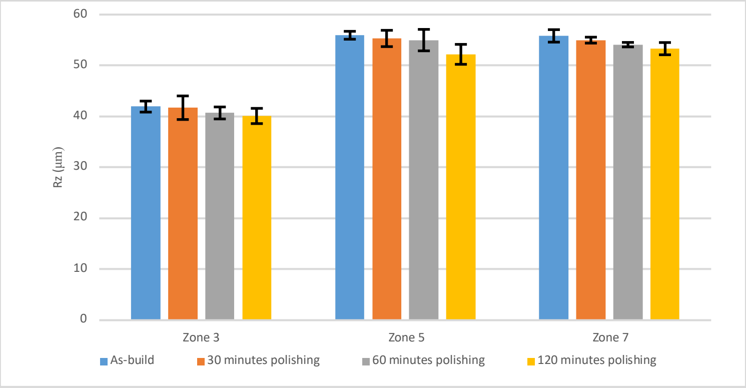

Figure 59: Rz values for semisphere surfaces of as-built and after dry electropolishing finishing periods (30, 60, and 120 minutes)

Figure 60–Figure 62 illustrate the percentage loss of the semisphere sample corresponding to various polishing durations across different zones. In every zone, the reduction in Ra is influenced by the duration of polishing; as the polishing time extends, the loss of Ra also escalates. Notably, polishing for 30 minutes results in the least Ra loss across all zones, while the most significant percentage loss of Ra occurs after 120 minutes of polishing. The data indicate that increased polishing duration correlates with greater Ra loss.

Rq and Rz exhibit similar patterns to Ra, as demonstrated in Figure 61 and Figure 62. The trend remains consistent across all zones, with percentage loss rising in tandem with polishing time, irrespective of the sample's location on the building plate. In Zone 7, the semisphere sample experiences the highest percentage loss at 24.50% in Ra after 120 minutes of polishing, whereas Zone 3 shows the lowest percentage loss at 2.21% after 30 minutes, as depicted in Figure 60. For Rq, Zone 7 also records the most substantial loss at 34.24% after 120 minutes, while Zone 3 registers the least loss at 1.77%, as shown in Figure 61. In terms of Rz, the highest percentage loss is observed in Zone 5 at 6.70% after 60 minutes of polishing, whereas the lowest loss is seen in Zone 3 as well, with a reduction of 0.53% after 30 minutes illustrated in Figure 62.

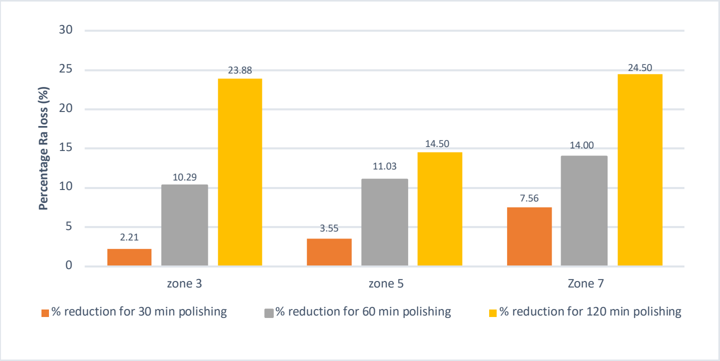

Figure 60: Ra reduction percentage for semisphere samples per zone for each polishing period

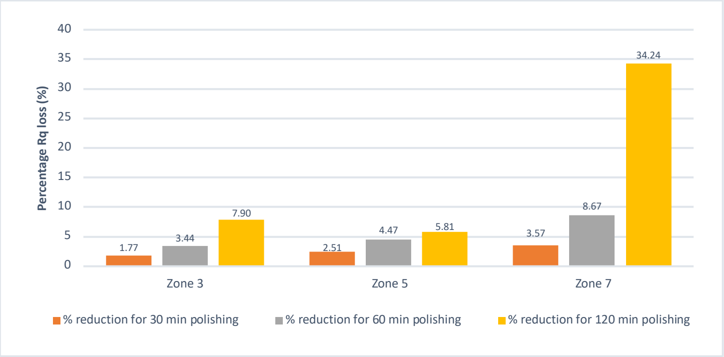

Figure 61: Rq reduction percentage for semisphere samples per zone for each polishing period

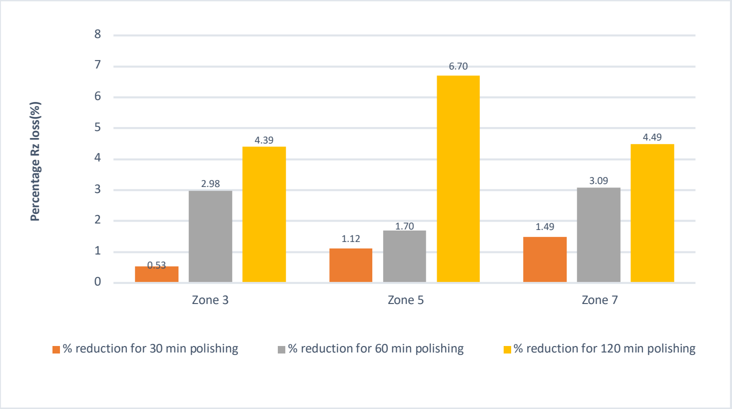

Figure 62: Rz reduction percentage for semisphere samples per zone for each polishing period

SEM micrographs of the semisphere surfaces of as-built samples and those subjected to dry electropolishing for durations of 30, 60, and 120 minutes are illustrated in Figure 63a–d. An increase in polishing time resulted in a notable decrease in surface roughness. In Figure 63a, the as-built semisphere is predominantly covered with ripples, contours, and staircases formed layer by layer and various-sized particles of partially sintered powder. After 30 minutes of polishing (Figure 63b), these features were substantially diminished, although some ripples, contours, staircases, and particles of partially sintered powder remained visible. The amount of partially sintered powder was reduced during this period. The surface treated for 60 minutes (Figure 63c) shows an additional decrease in partially sintered powder, yet staircases and contours are still visible. The 120 minutes of polishing (Figure 63d) resulted in the most significant improvement, exhibiting a surface that is largely free of partially sintered powder and smoother compared to the surfaces polished for 30 and 60 minutes, with a 24.50% Ra loss from the as-built state. The SEM micrographs (Figure 63a–d) reveal a slightly progressive improvement in surface quality with increasing dry electropolishing duration. The as-built semisphere exhibited prominent ripples, contours, stair-step features, and significant amounts of partially sintered powder. After 30 minutes of polishing, these features were noticeably reduced, although residual particles and layer-related morphologies remained. At 60 minutes, further removal of partially sintered powder was achieved, but traces of staircases and contours were still evident. The most substantial improvement occurred at 120 minutes, where the surface appeared smoother and largely free of particles compared to the as-built condition. This trend highlights the direct relationship between polishing duration, morphological refinement, and quantitative roughness reduction.

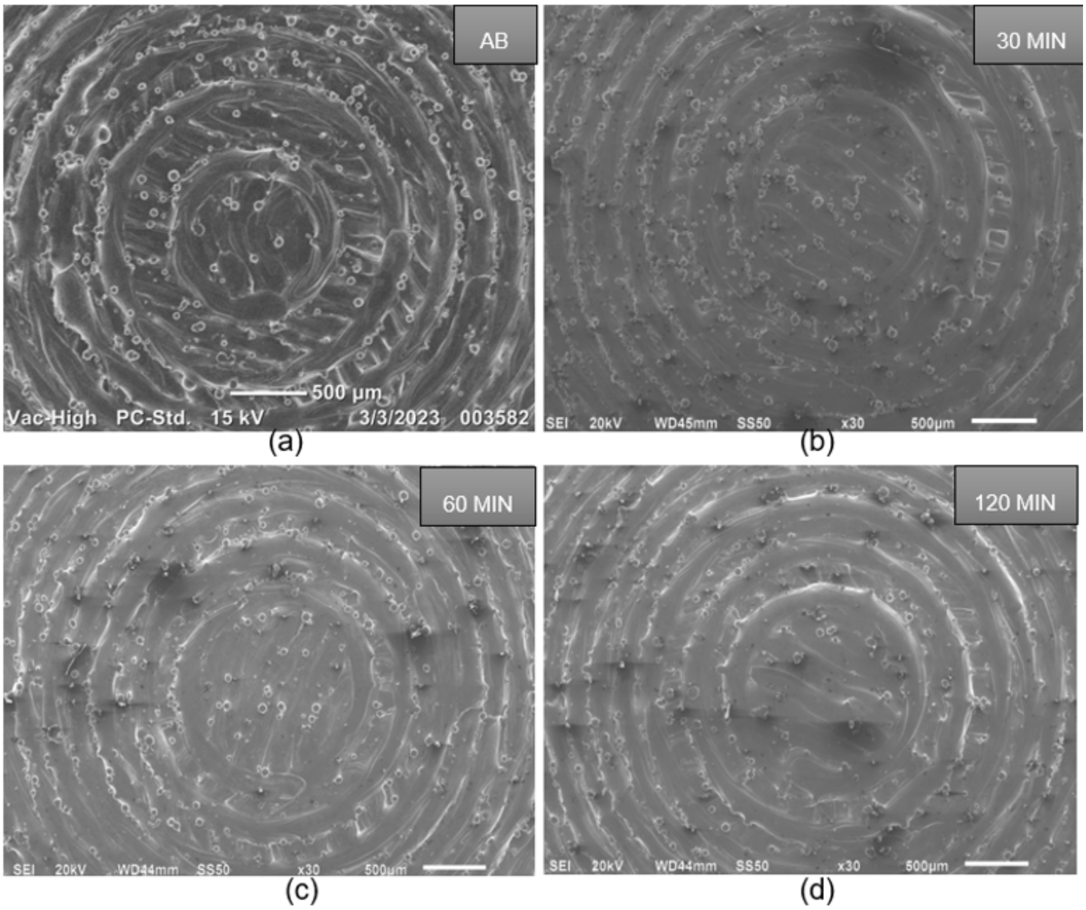

Figure 63: SEM micrographs (top view) of surfaces of semisphere samples L-PBF-produced Ti6Al4V ELI samples in a) as-built, b) 30 min, c) 60 min, and d) 120 min polishing condition

4.2.5. Conclusions

- In dry electropolishing, as the polishing time increases, a notable decrease in surface roughness was observed in all the zones.
- Percentage reduction among the selected periods of polishing shows that after 120 minutes, there was a significant reduction of surface roughness, but even after 120 minutes of dry electropolishing, the required surface finish for biomedical implants did not meet international standards.
- Increased period of polishing can result in a smoother surface; however, increasing the period of polishing results in higher processing time and cost.

4.3. Combination of dry electropolishing with chemical polishing

4.3.1. 30 minutes of dry electropolishing followed by 5 minutes of chemical polishing

Figure 64, Figure 65 and Figure 66 illustrate the surface roughness of the vertical (side surface) (V), horizontal (top surface) (H), and semisphere (S) surfaces after 30 minutes of dry electropolishing, followed by 5 minutes of chemical polishing. The mean and standard deviation for surface roughness parameters (Ra, Rq, and Rz) of the side, top, and semisphere surfaces after this treatment are detailed for each zone. It is evident across all zones that surface roughness decreased further after the 5 minutes of chemical polishing.

The most significant reduction in Ra after this process was recorded in Zone 3, corresponding to the semisphere samples, with a Ra value of 5.1 µm, while Zone 7 exhibited the least reduction with statistically significant differences noted (t-test $p < 0.05$). Additionally, both the top and side surfaces also displayed a decrease in surface roughness across all zones following the 5 minutes of chemical polishing. The trends for Rq and Rz mirrored that of Ra, with the greatest reductions occurring in Zone 3 and the least in Zone 7. After the 5 minutes of chemical polishing, the solution's temperature was measured at 20 °C, and the weight loss was relatively minor compared to the losses observed at 10 and 20 minutes of chemical polishing.

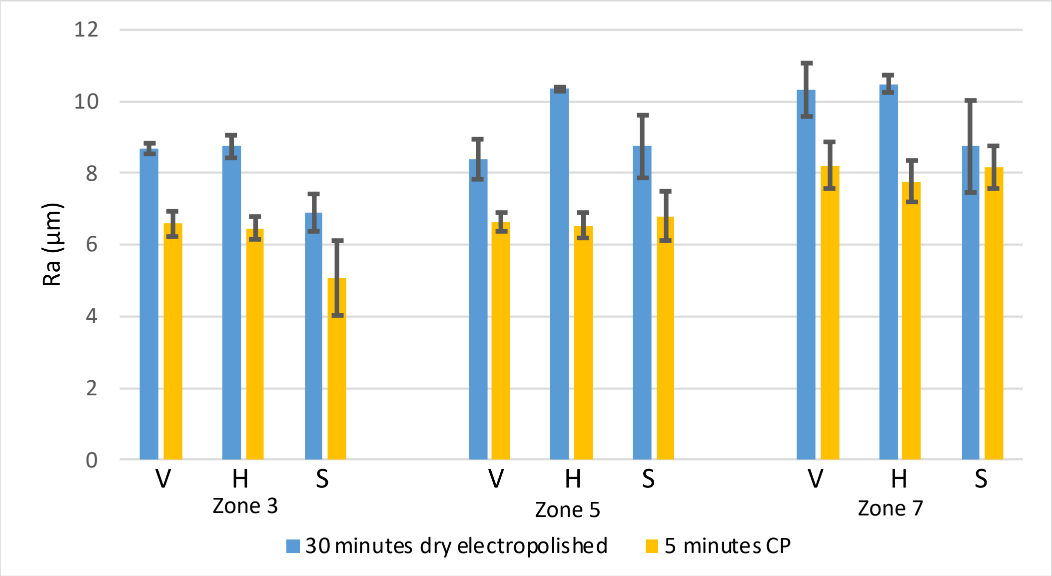

Figure 64: Ra after 30 minutes of dry electropolishing followed by 5 minutes of chemical polishing

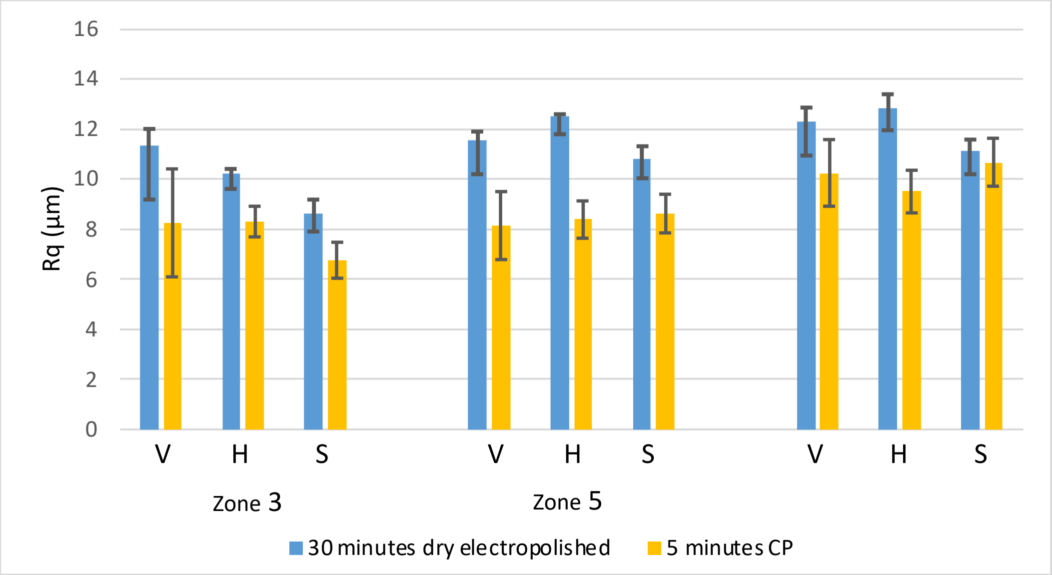

Figure 65: Rq after 30 minutes of dry electropolishing followed by 5 minutes of chemical polishing

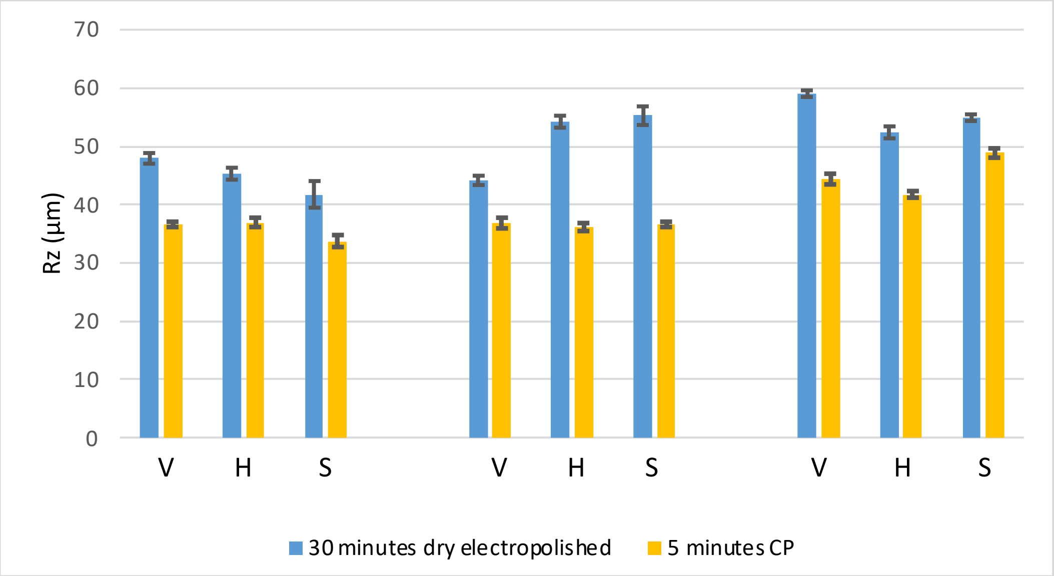

Figure 66: Rz after 30 minutes of dry electropolishing followed by 5 minutes of chemical polishing

Figure 67 presents SEM images of three types of samples: vertical (V), horizontal (H), and semisphere (S). A notable decrease in the presence of attached powder particles is evident across all samples in every zone compared to the results of the 30 minutes of dry electropolishing. Vertical samples exhibited melted-like attached powder particles in all zones after 5 minutes of chemical polishing. The horizontal samples retained some visibility of tracks, peaks, and valleys along with a reduced number of attached powder particles after the 5 minutes of chemical polishing. In the semisphere samples, there was an evident removal of attached powder particles and contour marks across all zones; however, the stair-step patterns remained visible in all samples.

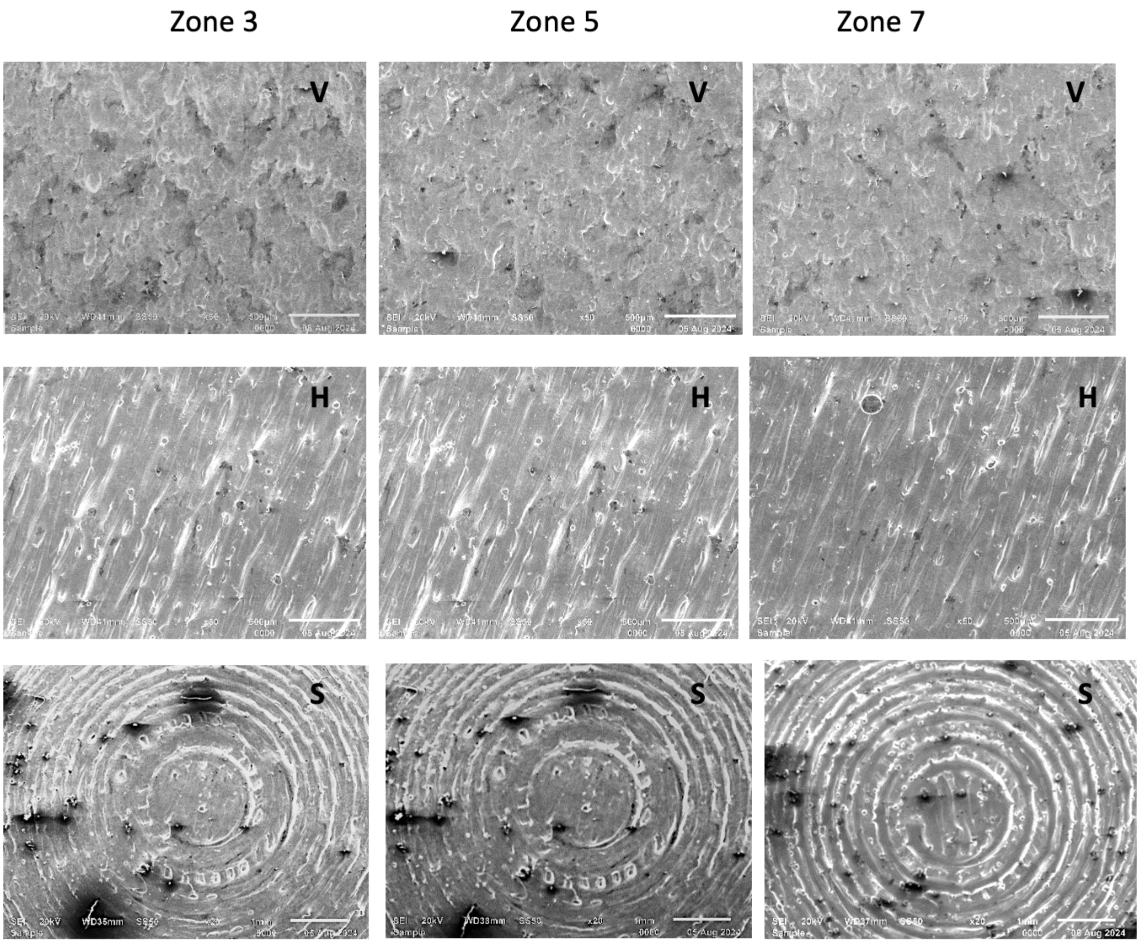

Figure 67: SEM images of 30 minutes of dry electropolishing followed by 5 minutes of chemical polishing

4.3.2. 60 minutes of dry electropolishing followed by 10 minutes of chemical polishing

Figure 68–Figure 70 illustrate the outcomes for Ra, Rq, and Rz after a 60-minute dry electropolishing process followed by an additional 10 minutes of chemical polishing. A

reduction in these parameters is evident. The vertical, horizontal, and semispherical surfaces display additional decreases in Ra, Rq, and Rz after the chemical polishing phase. It is noted that the duration of chemical polishing is directly proportional to the reduction observed in Ra, Rq, and Rz. Nevertheless, extending the time for chemical polishing leads to an increase in the chemical solution temperature, which can cause the part to melt, resulting in a loss of weight. After 5 minutes of chemical polishing, the temperature reached 20 °C while it increased to 25 °C after 10 minutes. The long duration of polishing leads to a rise in the temperature of the solution, resulting in the loss of mass of the samples. The loss of mass during this polishing was higher compared to that of 30 minutes of dry electropolishing followed by 5 minutes of chemical polishing in all the zones; this is due to long durations of polishing that lead to higher temperatures and result in speeding up of chemical reactions, with a greater rate of mass loss.

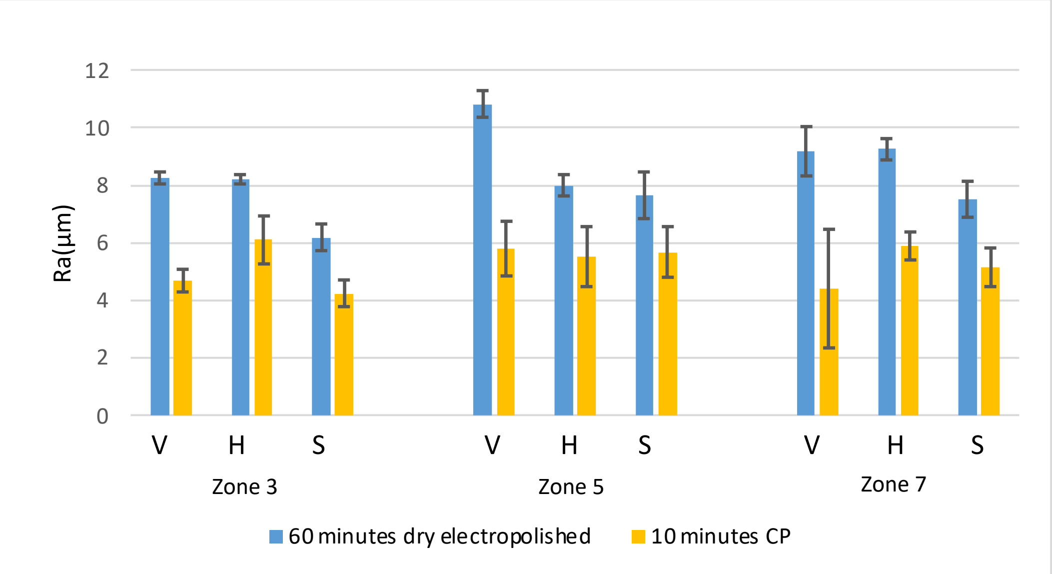

Figure 68: Ra after 60 minutes of dry electropolishing followed by 10 minutes of chemical polishing

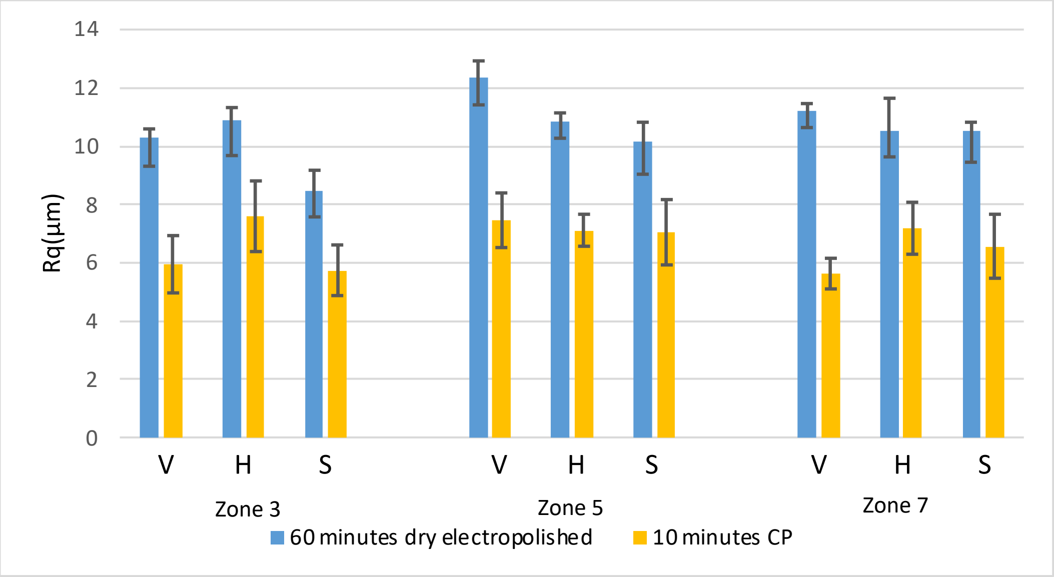

Figure 69: Rq after 60 minutes of dry electropolishing followed by 10 minutes of chemical polishing

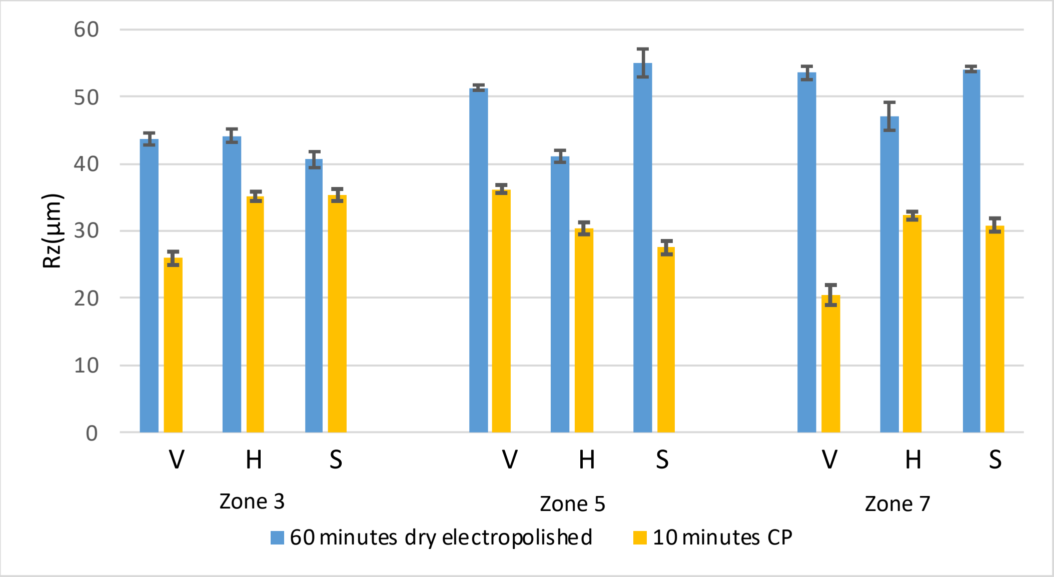

Figure 70: Rz after 60 minutes of dry electropolishing followed by 10 minutes of chemical polishing

Figure 71 shows the vertical, horizontal, and semispherical SEM images that were polished for 60 minutes of dry electropolishing followed by 10 minutes of chemical polishing. There is notable removal of powder particles attached to the surface of the vertical samples until the smooth surface emerges in all zones. However, the smooth surface is not uniform, as peaks and valleys are visible on the surface of the vertical samples in all the zones. There is continual removal of attached powder particles and the appearance of a smooth surface horizontal surface. The peaks and valleys due to tracks during the building were still visible. The reduction in contour, attached powder particles, and staircases can be seen in the semisphere sample.

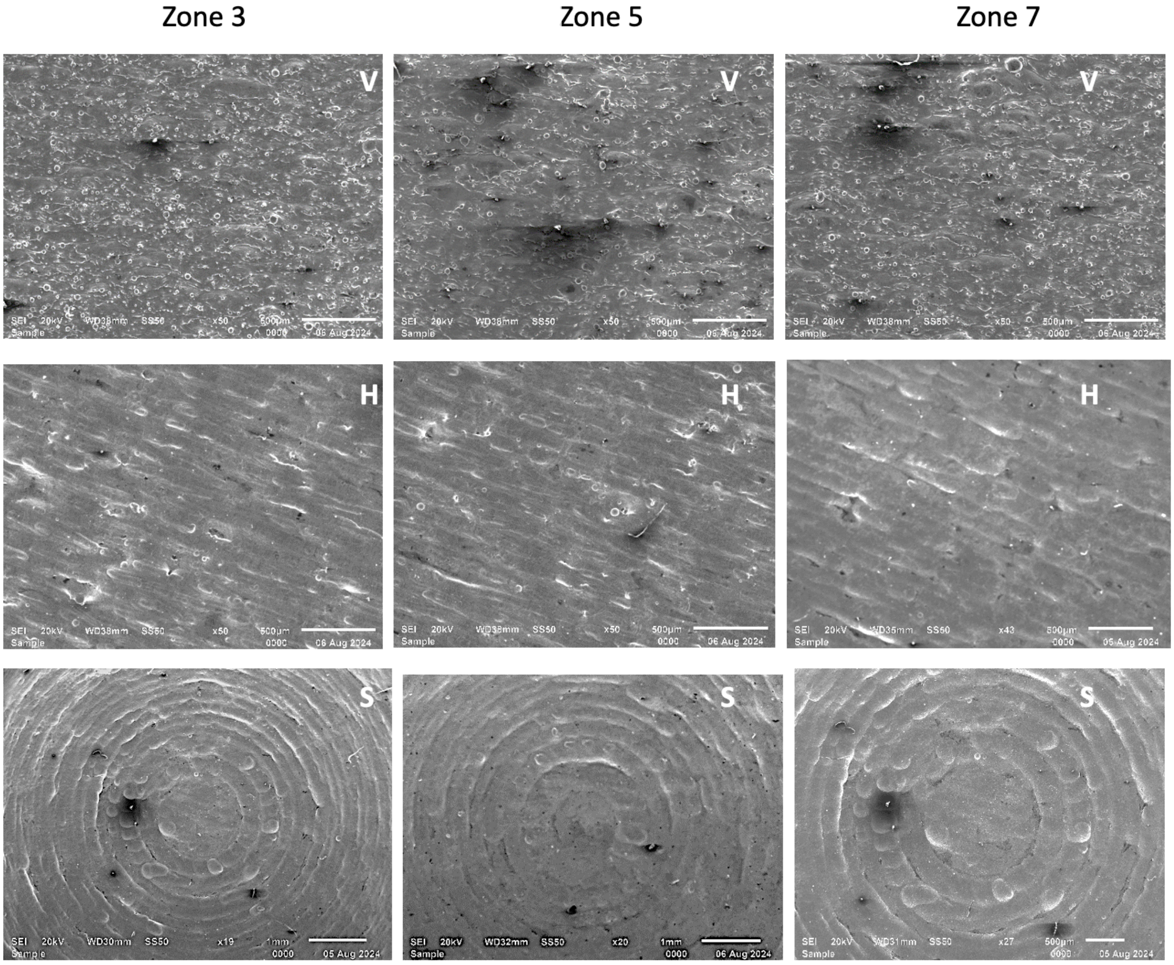

Figure 71: SEM images of 60 minutes of dry electropolishing followed by 10 minutes of chemical polishing

4.3.3. 120 minutes of dry electropolishing followed by 20 minutes of chemical polishing

The most significant reductions in Ra, Rq, and Rz are observed following 120 minutes of dry electropolishing, and this effect is enhanced when followed by 20 minutes of chemical polishing, especially when compared to 5 minutes and 10 minutes of chemical polishing as illustrated in Figure 72, Figure 73, and Figure 74. After 20 minutes of polishing, Zone 3 recorded the lowest Ra, while Zone 7 exhibited the highest. An increase in chemical polishing duration correlates with a greater decrease in Ra values. The minimum Ra observed was 2.858 μm in Zone 3, whereas the maximum following chemical polishing reached 3.875 µm in Zone 7. Rq and Rz displayed a similar pattern to Ra. Following 20 minutes of chemical polishing, the temperature was 40 °C due to the extended polishing time. Across all surfaces, including the sides, top, and semisphere, there was a marked reduction in surface roughness after 20 minutes of chemical polishing.

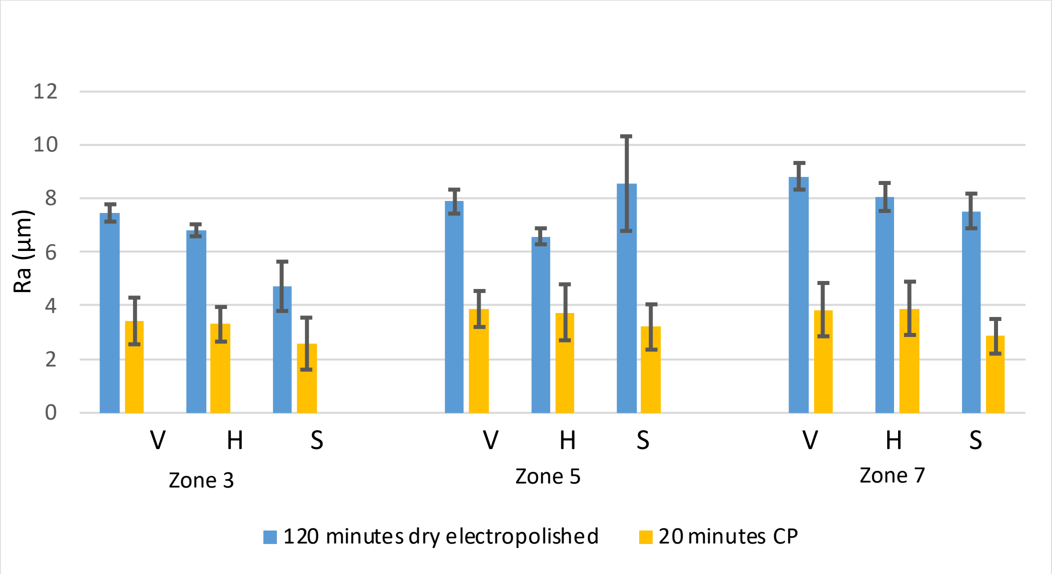

Figure 72: Ra after 120 minutes of dry electropolishing followed by 20 minutes of chemical polishing

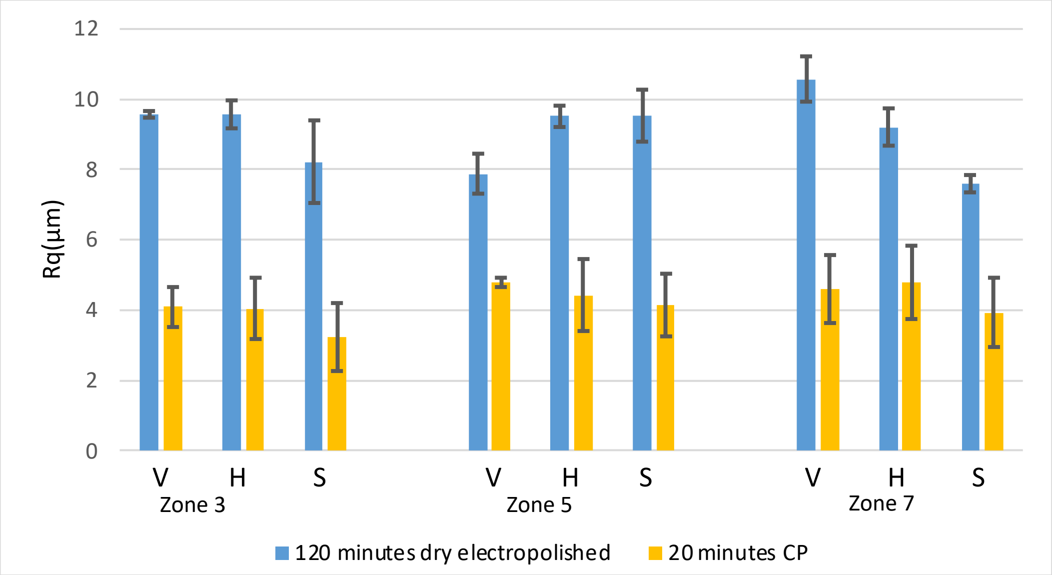

Figure 73: Rq after 120 minutes dry electropolishing followed by 20 minutes of chemical polishing

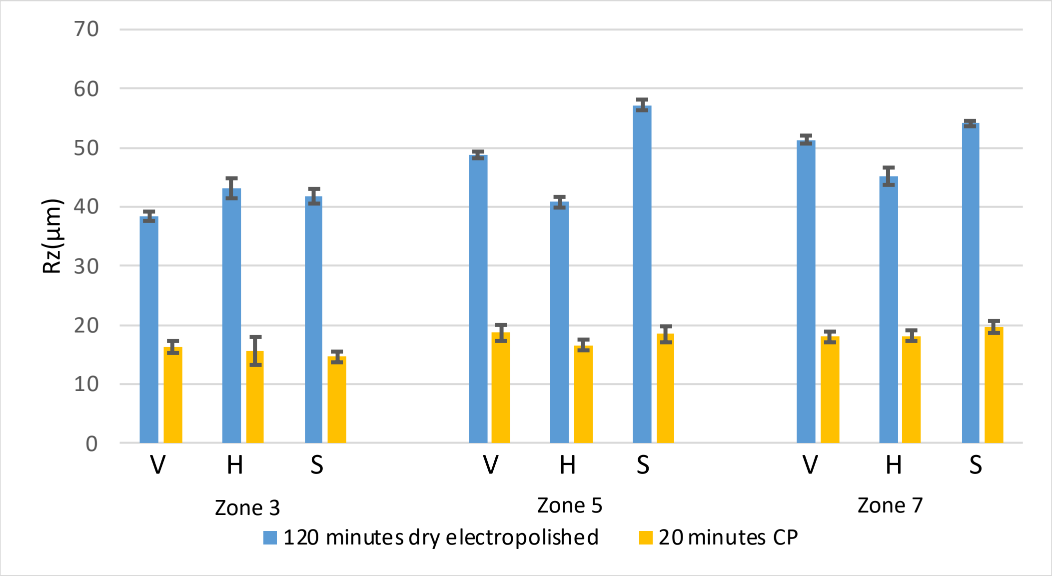

Figure 74: Rz of 120 minutes dry electropolishing followed by 20 minutes of chemical polishing

Figure 75 shows the SEM images of the vertical, horizontal, and semisphere samples that were polished for 120 minutes of dry electropolishing followed by 20 minutes of chemical polishing. After polishing, nearly all attached powder particles, peaks, and valleys were removed, resulting in a smooth surface observed in the vertical samples across all zones. The peaks and valleys due to tracks were still noticeable in the horizontal samples. Nearly all the attached powder particles, contours, and staircases on the surface of the semisphere were removed; however, the surface was not uniform, and peaks and valleys were visible.

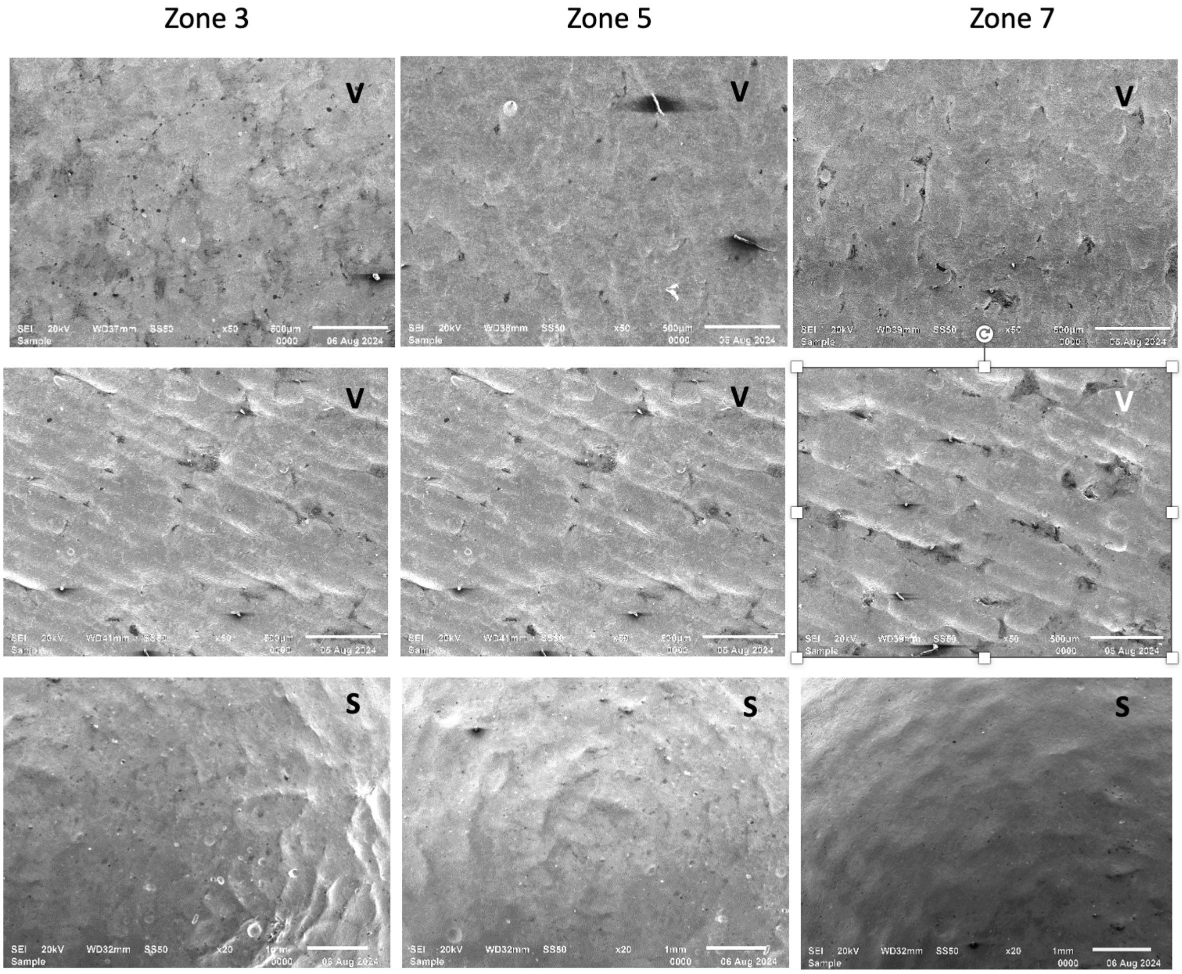

Figure 75: SEM images of 120 minutes of dry electropolishing followed by 20 minutes of chemical polishing

4.3.4. Weight loss before and after chemical polishing

During the process of chemical polishing, the surface quality of the samples across all zones showed considerable enhancement. Nevertheless, it was observed that as the surface roughness improved, there was a corresponding increase in the weight loss of the components. In the case of a 5-minute chemical polishing treatment, no notable enhancement in surface roughness was detected, and the weight loss was minimal when compared to longer polishing durations, as illustrated in Figure 76. A trend was noted where the weight of the components diminished as the duration of chemical polishing extended. Figure 76, Figure 77, Figure 78, and Appendix 4 depict the weight of the components before and after 5, 10, and 20 minutes of chemical polishing. Across all zones and forms, vertical, horizontal, and semisphere weight loss was evident throughout all durations of the chemical polishing process. The weight loss observed after 10 minutes of polishing was greater than that after 5 minutes. Furthermore, the 20-minute polishing resulted in significantly improved surface roughness compared to both the 5-minute and 10-minute treatments. However, it is important to note that while a 20-minute chemical polishing session led to marked improvements in surface roughness, it also resulted in a heightened weight loss, with parts polished for this duration exhibiting the greatest weight reduction, as shown in Figure 78. This phenomenon is attributed to the extended polishing time. The longer the chemical polishing duration, the better the achieved surface roughness, although there is an increase in weight loss during the process in HF and HNO_3 solutions. The loss of mass is due to higher temperatures that speed up chemical reactions leading to a greater rate of mass loss.

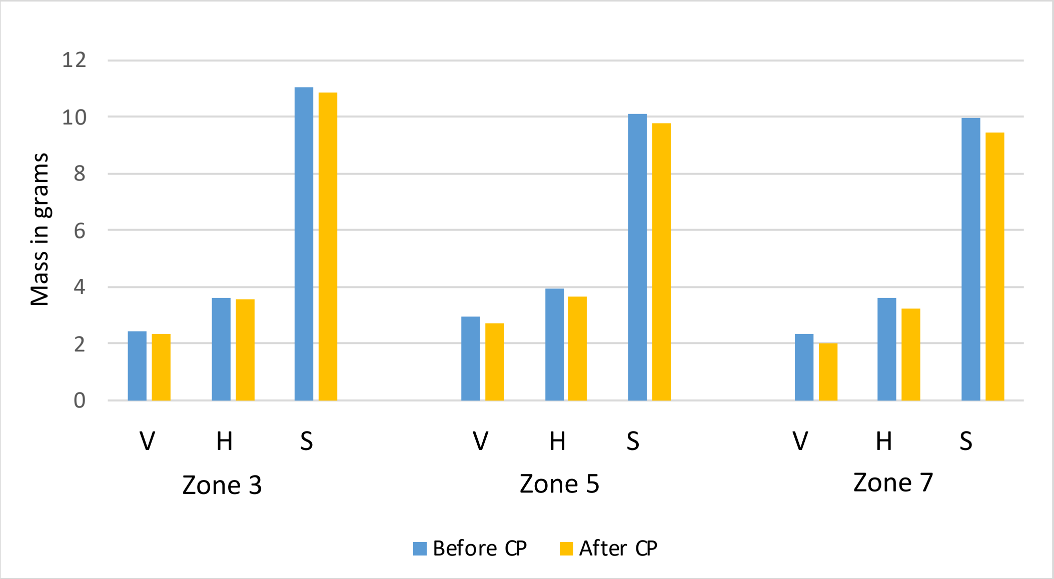

Figure 76: Weight loss after 5 minutes of chemical polishing

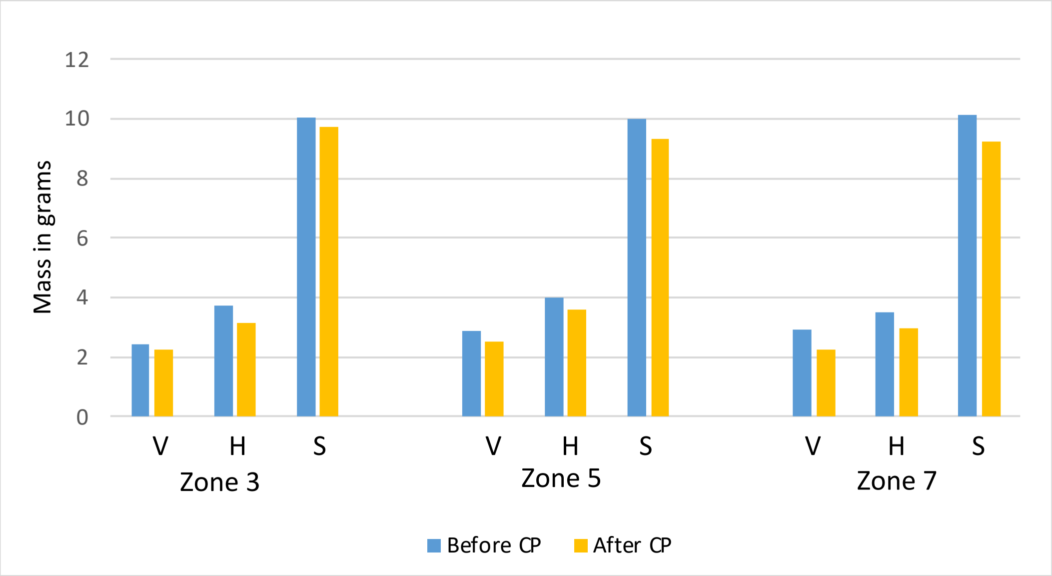

Figure 77: Weight loss after 10 minutes of chemical polishing

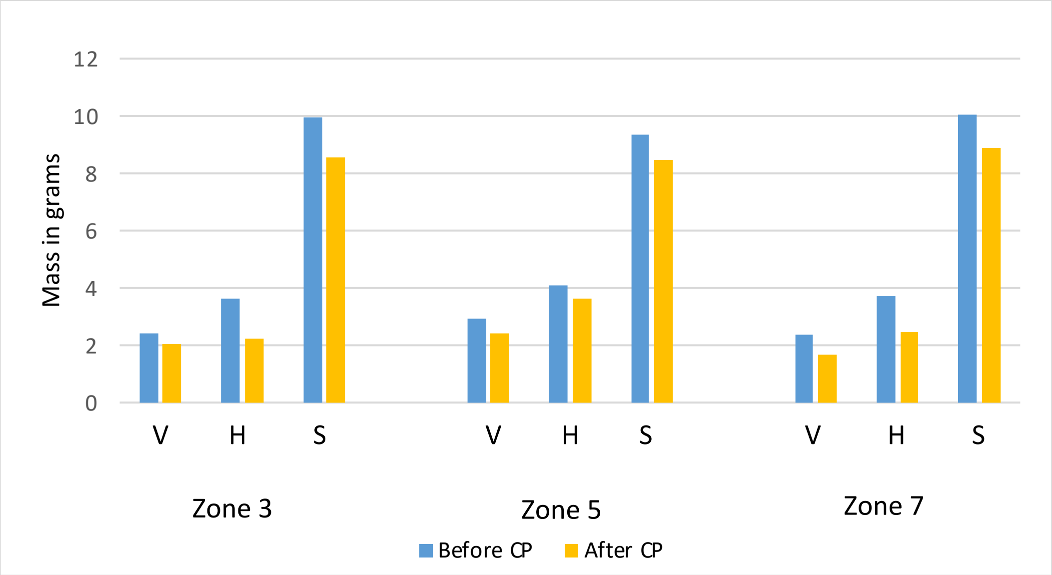

Figure 78: Weight loss after 20 minutes of chemical polishing

Overall, the SEM morphology and surface roughness results are consistent as the number of dry and chemical polishing cycles increases, morphological defects such as partially sintered powder, peaks, valleys, and stair-step patterns decrease, which is quantitatively captured by decreasing Ra, Rq, and Rz. The process demonstrates diminishing returns beyond certain durations, with improvements more pronounced in Zone 3 than Zones 5 and 7, highlighting the influence of local build conditions on surface finish. Prolonged chemical polishing enhanced surface quality at the expense of material removal, but following weight loss requires the balance between surface smoothness and component integrity.

4.3.5. Conclusions

- The combination of dry electropolishing and chemical polishing in HF and HNO_3 solution shows the surface roughness of Ra ≤ 5 µm required for biocompatibility, osseointegration, and longevity in medical implants after 120 minutes of dry electropolishing and 120 minutes of dry electropolishing, followed by 20 minutes chemical polishing.
- After 30 and 60 minutes of dry electropolishing and 30 and 60 minutes of dry electropolishing followed by 5 and 10 minutes of chemical polishing, there is a fluctuation of Ra, mostly Ra > 5µm.
- As the polishing period increases during chemical polishing, weight loss also increases.
- After 20 minutes of dry electropolishing and 120 minutes of dry electropolishing, followed by 20 minutes of chemical polishing, Ra ≤ 5µm is achieved; however, this comes at the expense of weight loss.
- After 30 and 60 minutes of dry electropolishing, and 30 and 60 minutes of dry electropolishing followed by 5 and 10 minutes of chemical polishing, the results show Ra>5 µm. However, the weight loss is lower compared to 20 minutes of DryLyte and 120 minutes of DryLyte followed by 20 minutes of chemical polishing.
- The loss of weight is due to several factors involved in chemical polishing, such as titanium dissolution, oxide layer removal, and surface roughening and pitting.

CHAPTER 5: CONCLUSION AND FUTURE WORK

This study presents and examines the outcomes derived from the as-built state and subsequent surface finishing through dry electro- and chemical polishing in HF and HNO_3 solutions of L-PBF Ti6Al4V samples for biomedical applications. The analysis focuses on assessing how the location within the building plate influences surface roughness both prior to and after surface finishing processes. The following conclusions can be drawn from this study:

1. The surface roughness of the as-built samples is found to be affected by their positioning on the building plate during the L-PBF AM process. Samples situated further from the Ar inlet exhibited a greater level of surface roughness compared to those located closer to it.
2. The particle size distribution (PSD) in L-PBF might have an impact on the surface roughness of the part. During the distribution of a layer of powder over the building plate, the areas at the inception of the powder deposition system (recoater) exhibit a high concentration of small particles, while the areas farthest from the initiation point of recoater exhibit a PSD from the larger particle fraction.
3. The as-built roughness on the side surface of the L-PBF part is primarily attributable to the thickness of the powder layer, peaks and valleys, and the presence of partially melted particles. In contrast, the predominant cause of surface roughness on the top surface is attributed to track-by-track and attached powder particles. The surface roughness on curved (or inclined) surfaces is mainly influenced by staircases, attached powder particles, and contours.
4. Dry electropolishing has been shown to effectively reduce surface roughness, irrespective of the samples' locations on the building plate. However, it should be noted that this process requires a longer processing time to achieve the required surface roughness for Ti6Al4V medical implants. The process of dry electropolishing indicates a decrease in surface roughness with an increase in processing time.

5. The combination of dry electro- and chemical polishing has been demonstrated to result in further significant reductions in surface roughness of the L-PBF parts.
6. Achieving the desired surface roughness of the implant through dry electropolishing followed by chemical polishing is possible; however, it should be noted that long-time chemical polishing may lead to significant mass loss of the component, pitting and protrusions on the surface. This occurs because prolonged exposure increases the temperature of the chemical solution, which can accelerate material removal.

Recommendation for future work

This study confirmed the feasibility of achieving the appropriate surface quality of simple rectangular and semispherical objects. Further research is necessary to determine whether surface optimization can be accomplished through chemical polishing without affecting dimensional accuracy of L-PBF components with complex shape and/or lattice structures.

References

Abd-Elaziem, W., Elkatatny, S., Abd-Elaziem, A., Khedr, M., Abd El-Baky, M., Hassan, M., Abu-Okail, M., Mohammed, M., Järvenpää, A., Allam, T. and Hamada, A. (2022) 'On the current research progress of metallic materials fabricated by laser powder bed fusion process: a review', *Journal of Materials Research and Technology*, 20, pp. 681–707. Available at: https://doi.org/10.1016/j.jmrt.2022.07.085

Abd-Elaziem, W., Darwish, A.M., Hamada, A. and Daoush, W.M. (2024) 'Titanium-based alloys and composites for orthopedic implants applications: A comprehensive review', *Materials and Design*, 241(December 2023), p. 112850. Available at: https://doi.org/10.1016/j.matdes.2024.112850

Abdi, F., Yavari, P., Harik, V. and Godines, C. (2020) 'Material allowable generation and AM process parameters effect on porosity', *Coatings*, 10(7). Available at: https://doi.org/10.3390/coatings10070625

Agarwal, P. (2021) *Manufacturing and Industrial Engineering*, *Manufacturing and Industrial Engineering*. Available at: https://doi.org/10.1201/9781003088073

Ahmed, N., Barsoum, I., Haidemenopoulos, G., and Abu Al-Rub, R.K. (2022) 'Process parameter selection and optimization of laser powder bed fusion for 316L stainless steel: A review', *Journal of Manufacturing Processes*, 75(October 2021), pp. 415–434. Available at: https://doi.org/10.1016/j.jmapro.2021.12.064

Ahuja, B., Karg, M. and Schmidt, M. (2015) 'Additive manufacturing in production: challenges and opportunities', *Laser 3D Manufacturing II*, 9353(July 2017), p. 935304. Available at: https://doi.org/10.1117/12.2082521

Ahuja, N., Grewal, N.S., Kumar, K., and Batra, U. (2023) 'Investigating in-vitro degradation, fatigue behavior, and fracture toughness of electrical discharge-processed mg alloys for biodegradable implant applications', *International Journal of Lightweight Materials and Manufacture*, 7(2), pp. 293–307. Available at: https://doi.org/10.1016/j.ijlmm.2023.11.001

AISI Type 316 Stainless Steel, annealed sheet Subcategory: (2020) Ferrous Metal; Metal; Stainless Steel; T 300 Series Stainless Steel Material Notes', *[Journal or Publisher]*, pp. 1–2.

Albrektsson, T. and Wennerberg, A. (2004) 'Oral implant surfaces: Part 1–review focusing on topographic and chemical properties of different surfaces and in vivo responses to them', *The International Journal of Prosthodontics*, 17(5), pp. 536–43. Available at: http://www.ncbi.nlm.nih.gov/pubmed/15543910

Alquaity, A.B.S. (2025) 'Influence of nozzle diameter and gas flow on spatter removal in laser powder bed fusion: A CFD approach', *Results in Engineering*, 25(December 2024), p. 103759. Available at: https://doi.org/10.1016/j.rineng.2024.103759

Amann, H. and Arba Mosquera, S. (2024) 'Optimization of the spot spacings for reducing roughness in laser-induced optical breakdown processes for corneal laser vision correction', *Photonics*, 11(2). Available at: https://doi.org/10.3390/photonics11020114

Anwar, A. Bin, Ibrahim, I.H. and Pham, Q.C. (2019) 'Spatter transport by inert gas flow in selective laser melting: A simulation study', *Powder Technology*, 352, pp. 103–116. Available at: https://doi.org/10.1016/j.powtec.2019.04.044

Artzt, K., Mishurova, T., Bauer, P.P., Gussone, J., Barriobero-Vila, P., Evsevleev, S., Bruno, G., Requena, G., and Haubrich, J. (2020) 'Pandora's box-influence of contour parameters on roughness and subsurface residual stresses in laser powder bed fusion of Ti-6Al-4V', *Materials*, 13(15). Available at: https://doi.org/10.3390/ma13153348

Balachandramurthi, A.R., Moverare, J., Dixit, N., and Pederson, R. (2018) 'Influence of defects and as-built surface roughness on fatigue properties of additively manufactured Alloy 718', *Materials Science and Engineering A*, 735(June), pp. 463–474. Available at: https://doi.org/10.1016/j.msea.2018.08.072

Balbaa, M.A., Ghasemi, A., Fereiduni, E., Elbestawi, M.A., Jadhav, S.D., and Kruth, J.P. (2021) 'Role of powder particle size on laser powder bed fusion processability of AlSi10mg alloy', *Additive Manufacturing*, 37(May 2020), p. 101630. Available at: https://doi.org/10.1016/j.addma.2020.101630

Barber, C.C., Burnham, M., Ojameruaye, O., and McKee, M.D. (2021) 'A systematic review of the use of titanium versus stainless steel implants for fracture fixation', *OTA International: The Open Access Journal of Orthopaedic Trauma*, 4(3), p. e138. Available at: https://doi.org/10.1097/oi9.0000000000000138

Barfeie, A., Wilson, J. and Rees, J. (2015) 'Implant surface characteristics and their effect on osseointegration', *British Dental Journal*, 218(5). Available at: https://doi.org/10.1038/sj.bdj.2015.171.

Bauristhene, A.M., Mutombo, K. and Stumpf, W.E. (2013) 'Alpha case formation mechanism in Ti-6Al-4V alloy investment castings using YFSZ shell moulds', *Southern African Institute of Mining and Metallurgy*, 113(4), pp. 357–361.

Benčina, M., Resnik, M., Starič, P., and Junkar, I. (2021) 'Use of plasma technologies for antibacterial surface properties of metals', *Molecules*, 26(5). Available at: https://doi.org/10.3390/molecules26051418

Bennett, J.L., Wolff, S.J., Hyatt, G., Ehmann, K., and Cao, J. (2017) 'Thermal effect on clad dimension for laser deposited Inconel 718', *Journal of Manufacturing Processes*, 28, pp. 550–557. Available at: https://doi.org/10.1016/j.jmapro.2017.04.024

Bezuidenhout, M., Ter Haar, G., Becker, T., Rudolph, S., Damm, O., and Sacks, N. (2020) 'The effect of HF-HNO3 chemical polishing on the surface roughness and fatigue life of laser powder bed fusion produced Ti6Al4V', *Materials Today Communications*, 25(June), p. 101396. Available at: https://doi.org/10.1016/j.mtcomm.2020.101396

Bhadeshia, H.K.D.H. (2016) ‘Additive manufacturing’, *Materials Science and Technology (United Kingdom)*, 32(7), pp. 615–616. Available at: https://doi.org/10.1080/02670836.2016.1197523

Bhushan, B. (2000) ‘Surface roughness analysis and measurement techniques’, *Modern Tribology Handbook: Volume One: Principles of Tribology*, pp. 49–119. Available at: https://doi.org/10.1201/9780849377877-10

Bocchetta, P., Chen, L.Y., Tardelli, J.D.C., Reis, A.C., Almeraya-Calderón, F., and Leo, P. (2021) ‘Passive layers and corrosion resistance of biomedical ti-6al-4v and β-ti alloys’, *Coatings*, 11(5). Available at: https://doi.org/10.3390/coatings11050487

Bouland, C., Urlea, V., Beaubier, K., Samoilenko, M., and Brailovski, V. (2019) ‘Abrasive flow machining of laser powder bed-fused parts: Numerical modeling and experimental validation’, *Journal of Materials Processing Technology*, 273(June), p. 116262. Available at: https://doi.org/10.1016/j.jmatprotec.2019.116262

Brown, C.A. (2012) ‘Roughness’, *Handbook of Lubrication and Tribology, Volume II: Theory and Design, Second Edition*, 123, pp. 3-1-3–13. Available at: https://doi.org/10.1201/b12265

Buser, D., Chappuis, V., Kuchler, U., Bornstein, M.M., Wittneben, J.G., Buser, R., Cavusoglu, Y., and Belser, U.C. (2013) ‘Long-term stability of early implant placement with contour augmentation’, *Journal of Dental Research*, 92(12). Available at: https://doi.org/10.1177/0022034513504949

Charfeddine, Y., Youssef, S., Sghaier, S., Sghaier, J., and Hamdi, H. (2021) ‘Study of the simultaneous grinding/ball-burnishing of AISI 4140 based on finite element simulations and experiments’, *International Journal of Mechanical Sciences*, 192(July 2020), p. 106097. Available at: https://doi.org/10.1016/j.ijmecsci.2020.106097.

Charles, A. P., Elkaseer, A., Müller, T., Thijs, L., Torge, M., Hagenmeyer, V., and Scholz, S. (2018) ‘A study of the factors influencing generated surface roughness of downfacing surfaces in selective laser melting’, *Proceedings of the World Congress on Micro and Nano Manufacturing*, pp. 327–330. Available at: https://doi.org/10.3850/978-981-11-2728-1_57

Cherenda, N.N., Basalai, A.V., Shymanski, V.I., Uglov, V.V., Astashynski, V.M., Kuzmitski, A.M., Laskovnev, A.P., and Remnev, G.E. (2018) ‘Modification of Ti-6Al-4V alloy element and phase composition by compression plasma flows impact’, *Surface and Coatings Technology*, 355(February), pp. 148–154. Available at: https://doi.org/10.1016/j.surfcoat.2018.02.048

Chiocca, A., Frendo, F. and Bertini, L. (2021) ‘Residual stresses influence on the fatigue strength of structural components’, *Procedia Structural Integrity*, 38(C), pp. 447–456. Available at: https://doi.org/10.1016/j.prostr.2022.03.045

Chowdhury, S., Yadaiah, N., Prakash, C., Ramakrishna, S., Dixit, S., Gupta, L.R., and Buddhi, D. (2022) ‘Laser powder bed fusion: a state-of-the-art review of the technology, materials, properties & defects, and numerical modelling’, *Journal of*

Materials Research and Technology, 20, pp. 2109–2172. Available at: https://doi.org/10.1016/j.jmrt.2022.07.121

Collan, M. and Michelsen, K.E. (2020) *Technical, Economic and Societal Effects of Manufacturing 4.0: Automation, Adaption and Manufacturing in Finland and Beyond*, *Technical, Economic and Societal Effects of Manufacturing 4.0: Automation, Adaption and Manufacturing in Finland and Beyond*. Available at: https://doi.org/10.1007/978-3-030-46103-4

Cutolo, A., Neirinck, B., Lietaert, K., de Formanoir, C., and Van Hooreweder, B. (2018) ‘Influence of layer thickness and post-process treatments on the fatigue properties of CoCr scaffolds produced by laser powder bed fusion’, *Additive Manufacturing*, 23(June), pp. 498–504. Available at: https://doi.org/10.1016/j.addma.2018.07.008

Davoodi, E., Montazerian, H., Mirhakimi, A.S., Zhianmanesh, M., Ibhadode, O., Shahabad, S.I., Esmaeilizadeh, R., Sarikhani, E., Toorandaz, S., Sarabi, S.A. and Nasiri, R. (2022) *Additively manufactured metallic biomaterials*, *Bioactive Materials*. KeAi Communications Co., Ltd. Available at: https://doi.org/10.1016/j.bioactmat.2021.12.027

DebRoy, T., Wei, H.L., Zuback, J.S., Mukherjee, T., Elmer, J.W., Milewski, J.O., Beese, A.M., Wilson-Heid, A., De, A. and Zhang, W. (2018) ‘Additive manufacturing of metallic components – Process, structure and properties’, *Progress in Materials Science*, 92, pp. 112–224. Available at: https://doi.org/10.1016/j.pmatsci.2017.10.001

Depboylu, F.N., Yasa, E., Poyraz, Ö., Minguella-Canela, J., Korkusuz, F. and De los Santos López, M.A. (2022) ‘Titanium based bone implants production using laser powder bed fusion technology’, *Journal of Materials Research and Technology*, 17, pp. 1408–1426. Available at: https://doi.org/10.1016/j.jmrt.2022.01.087

Dimkovski, Z. (2006) ‘Characterization of a Cylinder Liner Surface by Roughness Parameters Analysis’, *Mechanical Engineering* [Preprint].

Dong, Z., Liu, Y., Wen, W., Ge, J. and Liang, J. (2018) ‘Effect of hatch spacing on melt pool and as-built quality during selective laser melting of stainless steel: Modeling and experimental approaches’, *Materials*, 12(1). Available at: https://doi.org/10.3390/ma12010050

Elias, C.N., Fernandes, D.J., Souza, F.M., Monteiro, E.D.S. and Biaggio, S.R. (2018) ‘Mechanical and clinical properties of titanium and titanium-based alloys (Ti G2, Ti G4 cold worked nanostructured and Ti G5) for biomedical applications’, *Integrative Medicine Research*, 8(1), pp. 1060–1069. Available at: https://doi.org/10.1016/j.jmrt.2018.07.016

Eliaz, N. (2019) ‘Corrosion of metallic biomaterials: A review’, *Materials*, 12(3). Available at: https://doi.org/10.3390/ma12030407

Erinosho, M.F., Akinlabi, E.T. and Johnson, O.T. (2019) ‘Effect of scanning speed on the surface roughness of laser metal deposited copper on titanium alloy’, *Materials Research*, 22(5), pp. 3–8. Available at: https://doi.org/10.1590/1980-5373-MR-2019-

0297

Etesami, S.A., Fotovvati, B. and Asadi, E. (2022) ‘Heat treatment of Ti-6Al-4V alloy manufactured by laser-based powder-bed fusion: Process, microstructures, and mechanical properties correlations’, *Journal of Alloys and Compounds*, 895, p. 162618. Available at: https://doi.org/10.1016/j.jallcom.2021.162618

Fatemi, A., Molaei, R. and Phan, N. (2020) ‘Multiaxial fatigue of additive manufactured metals: Performance, analysis, and applications’, *International Journal of Fatigue*, 134(December 2019), p. 105479. Available at: https://doi.org/10.1016/j.ijfatigue.2020.105479

Feng, Z., Zhang, X., Wang, Y., Liu, H. and Chen, J. (2024) ‘Influence of scale effect on surface morphology in laser powder bed fusion technology’, *Virtual and Physical Prototyping*, 19(1), pp. 1–21. Available at: https://doi.org/10.1080/17452759.2024.2336157

Ferrar, B., Mullen, L., Jones, E., Stamp, R. and Sutcliffe, C.J. (2012) ‘Gas flow effects on selective laser melting (SLM) manufacturing performance’, *Journal of Materials Processing Technology*, 212(2), pp. 355–364. Available at: https://doi.org/10.1016/j.jmatprotec.2011.09.020

Fischer, A., Jacobs, J. J., and Pourzal, R. (2023) ‘Ti6Al4V implant alloys’, *Current Osteoporosis Reports*, 8(1), pp. 1–28. Available at: https://doi.org/10.1007/s40735-021-00623-3

Fox, J.C., Moylan, S.P. and Lane, B.M. (2016) ‘Effect of process parameters on the surface roughness of overhanging structures in laser powder bed fusion additive manufacturing’, *Procedia CIRP*, 45, pp. 131–134. Available at: https://doi.org/10.1016/j.procir.2016.02.347

Gadelmawla, E.S., Koura, M.M., Maksoud, T.M.A., Elewa, I.M. and Soliman, H.H. (2002) ‘Roughness parameters’, *Journal of Materials Processing Technology*, 123(1), pp. 133–145. Available at: https://doi.org/10.1016/S0924-0136(02)00060-2

Gaur, B., Ghyar, R. and Bhallamudi, R. (2022) ‘Parameter optimization for printing Ti6Al4V-alloy patient-customized orthopaedic implants by laser powder bed fusion using physio-mechanical properties and biological evaluations’, *Indian Journal of Orthopaedics*, 56(5), pp. 797–804. Available at: https://doi.org/10.1007/s43465-021-00577-1

Geetha, M., Singh, A.K., Asokamani, R. and Gogia, A.K. (2009) ‘Ti based biomaterials, the ultimate choice for orthopaedic implants - A review’, *Progress in Materials Science*, 54(3), pp. 397–425. Available at: https://doi.org/10.1016/j.pmatsci.2008.06.004

GonzáLez-Carrasco, J.L. (2009) *Metals as bone repair materials*, *Bone Repair Biomaterials*. Available at: https://doi.org/10.1533/9781845696610.2.154

Gorsse, S., Hutchinson, C., Gouné, M. and Banerjee, R. (2017) ‘Additive manufacturing of metals: a brief review of the characteristic microstructures and properties of steels, Ti-6Al-4V and high-entropy alloys’, *Science and Technology of Advanced Materials*, 18(1), pp. 584–610. Available at: https://doi.org/10.1080/14686996.2017.1361305

Goulas, A. *et al.* (2016) ‘Solid Freeform Fabrication 2016: Proceedings of the 26th Annual International Solid Freeform Fabrication Symposium – An Additive Manufacturing Conference Reviewed Paper’, pp. 2271–2281.

Le Guéhennec, L., Soueidan, A., Layrolle, P., and Amouriq, Y. (2007) ‘Surface treatments of titanium dental implants for rapid osseointegration’, *Dental Materials*, 23(7), pp. 844–854. Available at: https://doi.org/10.1016/j.dental.2006.06.025

Guo, Q., Zhao, C., Escano, L.I., Young, Z., Xiong, L., Fezzaa, K., Everhart, W., Brown, B., Sun, T., and Chen, L. (2018) ‘Transient dynamics of powder spattering in laser powder bed fusion additive manufacturing process revealed by in-situ high-speed high-energy x-ray imaging’, *Acta Materialia*, 151, pp. 169–180. Available at: https://doi.org/10.1016/j.actamat.2018.03.036

Han, T., Chen, J., Wei, Z., Qu, N., Liu, Y., Yang, D., Zhao, S., Lai, Z., Jiang, M., and Zhu, J. (2023) ‘Effect of cooling rate on microstructure and mechanical properties of AlCrFe2Ni2 medium entropy alloy fabricated by laser powder bed fusion’, *Journal of Materials Research and Technology*, 25, pp. 4063–4073. Available at: https://doi.org/10.1016/j.jmrt.2023.06.241

Hansson, K.N. and Hansson, S. (2011) ‘Skewness and Kurtosis: Important Parameters in the Characterization of Dental Implant Surface Roughness—A Computer Simulation’, *ISRN Materials Science*, 2011, pp. 1–6. Available at: https://doi.org/10.5402/2011/305312

Hansson, S. and Norton, M. (1999) ‘The relation between surface roughness and interfacial shear strength for bone-anchored implants. A mathematical model’, *Journal of Biomechanics*, 32(8), pp. 829–836. Available at: https://doi.org/10.1016/S0021-9290(99)00058-5

Hao, L., Wang, W., Zeng, J., Song, M., Chang, S., and Zhu, C. (2023) ‘Effect of scanning speed and laser power on formability, microstructure, and quality of 316L stainless steel prepared by selective laser melting’, *Journal of Materials Research and Technology*, 25, pp. 3189–3199. Available at: https://doi.org/10.1016/j.jmrt.2023.06.144

Hashmi, A.W., Khan, M., Khan, A., Khan, M.A., and Khan, A. (2023) ‘A comprehensive review on surface post-treatments for freeform surfaces of bio-implants’, *Journal of Materials Research and Technology*, 23, pp. 4866–4908. Available at: https://doi.org/10.1016/j.jmrt.2023.02.007

Heary, R.F., Parvathreddy, N., Sampath, S., and Agarwal, N. (2017) ‘Elastic modulus in the selection of interbody implants’, *Journal of Spine Surgery*, 3(2), pp. 163–167. Available at: https://doi.org/10.21037/jss.2017.05.01

Hong, J.H. and Yeoh, F.Y. (2019) ‘Mechanical properties and corrosion resistance of cobalt-chrome alloy fabricated using additive manufacturing', *Materials Today: Proceedings*, 29(November 2018), pp. 196–201. Available at: https://doi.org/10.1016/j.matpr.2020.05.543

Hossain, N., Hossain, M.Z., Al Mahmud, M.T., and Rayhan, M.A. (2023) 'Recent development of dental implant materials, synthesis process, and failure – A review', *Results in Chemistry*, 6(July), p. 101136. Available at: https://doi.org/10.1016/j.rechem.2023.101136

Islam, S. A., Hao, L., Javaid, Z., Xiong, W., Li, Y., Jamil, Y., Chen, Q., & Han, G. (2024). Surface Roughness of Interior Fine Flow Channels in Selective Laser Melted Ti-6Al-4V Alloy Components. *Micromachines*, 15(3), 348. https://doi.org/10.3390/mi15030348

Herrera, P., Zhang, W., and Zhang, L. (2023) 'Abrasive wear resistance of Ti-6Al-4V obtained by the conventional manufacturing process and by electron beam melting (EBM)', *Wear*, 524, p. 204. Available at: https://doi.org/10.1016/j.wear.2023.204

Javaid, M., Haleem, A., and Singh, R. (2021) 'Role of additive manufacturing applications towards environmental sustainability', *Advanced Industrial and Engineering Polymer Research*, 4(4), pp. 312–322. Available at: https://doi.org/10.1016/j.aiepr.2021.07.005

Jemat, A., Ghazali, M.J., Razali, M., and Otsuka, Y. (2015a) 'Surface modifications and their effects on titanium dental implants', *BioMed Research International*, 2015. Available at: https://doi.org/10.1155/2015/791725

Jemat, A., Ghazali, M.J., Razali, M., and Otsuka, Y. (2015) 'Surface modifications and their effects on titanium dental implants', *BioMed Research International*, 2015b. Available at: https://doi.org/10.1155/2015/791725

Kamachi Mudali, U., Sridhar, T.M. and Baldev, R.A.J. (2003) 'Corrosion of bio implants', *Sadhana - Academy Proceedings in Engineering Sciences*, 28(3–4), pp. 601–637. Available at: https://doi.org/10.1007/BF02706450

Kasperovich, G., Becker, R., Artzt, K., Barriobero-Vila, P., Requena, G., and Haubrich, J. (2021) 'The effect of build direction and geometric optimization in laser powder bed fusion of Inconel 718 structures with internal channels', *Materials and Design*, 207, p. 109858. Available at: https://doi.org/10.1016/j.matdes.2021.109858

Keyence (2001) 'Introduction to Surface Roughness'. Available at: https://www.keyence.com

Khairallah, S.A., Anderson, A.T., Rubenchik, A., and King, W.E. (2016) 'Laser powder-bed fusion additive manufacturing: Physics of complex melt flow and formation mechanisms of pores, spatter, and denudation zones', *Acta Materialia*, 108, pp. 36–45. Available at: https://doi.org/10.1016/j.actamat.2016.02.014

Kónya, G. and Ficzere, P. (2023) 'The effect of layer thickness and orientation of the workpiece on the micro- and macrogeometric properties and the machining time of the part during 3D printing', *Periodica Polytechnica Mechanical Engineering*, 67(2), pp. 143–150. Available at: https://doi.org/10.3311/PPme.21473

Kumar, K. and Kumar, G. S. (2015) 'An experimental and theoretical investigation of surface roughness of poly-jet printed parts: *Virtual and Physical Prototyping*, 10(1), pp. 23–34. Available at: https://doi.org/10.1080/17452759.2014.999218

Lammi, C.J. and Lados, D.A. (2011) 'Effects of residual stresses on fatigue crack growth behavior of structural materials: Analytical corrections', *International Journal of Fatigue*, 33(7), pp. 858–867. Available at: https://doi.org/10.1016/j.ijfatigue.2011.01.019

Le, T.P., Wang, X., Davidson, K.P., Fronda, J.E., and Seita, M. (2021) 'Experimental analysis of powder layer quality as a function of feedstock and recoating strategies', *Additive Manufacturing*, 39, p. 101890. Available at: https://doi.org/10.1016/j.addma.2021.101890

Lee, J.M., Sing, S.L. and Yeong, W.Y. (2020) 'Bioprinting of multimaterials with computer-aided design/computer-aided manufacturing', *International Journal of Bioprinting*, 6(1), pp. 65–73. Available at: https://doi.org/10.18063/ijb.v6i1.245

Lee, J.Y., Nagalingam, A.P. and Yeo, S.H. (2021) 'A review on the state-of-the-art of surface finishing processes and related ISO/ASTM standards for metal additive manufactured components', *Virtual and Physical Prototyping*, 16(1), pp. 68–96. Available at: https://doi.org/10.1080/17452759.2020.1830346

Li, Y., Yang, C., Zhao, H., Qu, S., Li, X., and Li, Y. (2014) 'New developments of ti-based alloys for biomedical applications', *Materials*, 7(3), pp. 1709–1800. Available at: https://doi.org/10.3390/ma7031709

Lin, C.C., Hu, C.C. and Lee, T.C. (2009) 'Electropolishing of 304 stainless steel: Interactive effects of glycerol content, bath temperature, and current density on surface roughness and morphology', *Surface and Coatings Technology*, 204(4), pp. 448–454. Available at: https://doi.org/10.1016/j.surfcoat.2009.08.005

Liu, M., Kumar, A., Bukkapatnam, S., and Kuttolamadom, M. 'A review of the anomalies in directed energy deposition (DED) processes & potential solutions - Part quality & defects', *Procedia Manufacturing*, 53(Figure 1), pp. 507–518. Available at: https://doi.org/10.1016/j.promfg.2021.06.093

Liverani, E., Manfredi, D., and Fino, P. (2017) 'Effect of selective laser melting (SLM) process parameters on microstructure and mechanical properties of 316L austenitic stainless steel', *Journal of Materials Processing Technology*, 249(November 2016), pp. 255–263. Available at: https://doi.org/10.1016/j.jmatprotec.2017.05.042

Lu, S.L., Zhang, Z.J., Liu, R., Qu, Z., Wang, B., Zhou, X.H., Eckert, J., and Zhang, Z.F. (2022) 'Prior β grain evolution and phase transformation of selective laser melted Ti6Al4V alloy during heat treatment', *Journal of Alloys and Compounds*, 914. Available at: https://doi.org/10.1016/j.jallcom.2022.165235

Makoana, N. W., Yadroitsava, I., Moller, H., and Yadroitsev, I. (2018) 'Characterization of 17-4PH single tracks produced at different parametric conditions towards increased productivity of LPBF systems—the effect of laser power and spot size upscaling', *Journal of Materials Processing Technology*. Available at: https://doi.org/10.3390/met8070475

Mahtabi, M.B., Yadollahi, A., Morgan-Barnes, C., Priddy, M.W., and Rhee, H. (2024) 'effects of powder reuse and particle size distribution on structural integrity of Ti-6Al-4V processed via laser beam directed energy deposition', *Journal of Manufacturing and Materials Processing*, 8(5). Available at: https://doi.org/10.3390/jmmp8050209

Majumdar, T., Bazin, T., Ribeiro, E.M.C., Frith, J.E., and Birbilis, N. (2019) 'Understanding the effects of PBF process parameter interplay on Ti-6Al-4V surface properties', *PLoS ONE*, 14(8), pp. 1–24. Available at: https://doi.org/10.1371/journal.pone.0221198

Mäkinen, M., Jauhiainen, E., Matilainen, V.P., Riihimäki, J., Ritvanen, J., Piili, H., and Salminen, A. (2015) 'Preliminary comparison of properties between Ni-electroplated stainless steel parts fabricated with laser additive manufacturing and conventional machining', *Physics Procedia*, 78(December), pp. 337–346. Available at: https://doi.org/10.1016/j.phpro.2015.11.048

Martucci, A., Aversa, A. and Lombardi, M. (2023) 'Ongoing challenges of laser-based powder bed fusion processing of Al alloys and potential solutions from the literature—A review', *Materials*, 16(3). Available at: https://doi.org/10.3390/ma16031084

Masiagutova, E., Cabanettes, F., Sova, A., Cici, M., Bidron, G., and Bertrand, P. (2021) 'Side surface topography generation during laser powder bed fusion of AlSi10Mg', *Additive Manufacturing*, 47(June), p. 102230. Available at: https://doi.org/10.1016/j.addma.2021.102230

Sahay, C. and Ghosh, S. (2018) 'Understanding surface quality: Beyond average roughness (Ra)', in *Proceedings of the 2018 ASEE Annual Conference & Exposition*. American Society for Engineering Education. Available at: https://doi.org/10.18260/1-2--31176

Mehrpouya, M., Vosooghnia, A., Dehghanghadikolaei, A., and Fotovvati, B. (2021) *The benefits of additive manufacturing for sustainable design and production*, *Sustainable Manufacturing*. Available at: https://doi.org/10.1016/B978-0-12-818115-7.00009-2

Mitutoyo (2010) 'Quick guide to surface roughness measurement: Reference guide for laboratory and workshop.', *Mitutoyo America Corporation*, 1(2229), pp. 1–8.

Moghadasi, K., Yadollahi, A., and Rhee, H. (2022) 'A review on biomedical implant materials and the effect of friction stir based techniques on their mechanical and tribological properties', *Journal of Materials Research and Technology*, 17, pp. 1054–1121. Available at: https://doi.org/10.1016/j.jmrt.2022.01.050

Mugwagwa, L., Yadollahi, A., and Rhee, H. (2021) *Residual stress in laser powder* *bed fusion*, *Fundamentals of Laser Powder Bed Fusion of Metals*. Available at: https://doi.org/10.1016/B978-0-12-824090-8.00014-7

Murr, L.E., Esquivel, E.V., Quinones, S.A., Gaytan, S.M., Lopez, M.I., Martinez, E.Y., Medina, F., Hernandez, D.H., Martinez, E., Martinez, J.L., and Wicker, R.B. (2009) ‘Microstructure and mechanical behavior of Ti-6Al-4V produced by rapid-layer manufacturing, for biomedical applications’, *Journal of the Mechanical Behavior of Biomedical Materials*, 2(1), pp. 20–32. Available at: https://doi.org/10.1016/j.jmbbm.2008.05.004

Mussatto, A., Yadollahi, A., and Rhee, H. (2021) ‘Influences of powder morphology and spreading parameters on the powder bed topography uniformity in powder bed fusion metal additive manufacturing’, *Additive Manufacturing*, (November 2020), p38. 101807. Available at: https://doi.org/10.1016/j.addma.2020.101807

Nagalingam, A.P., Vohra, M.S., Kapur, P., and Yeo, S.H. (2021) ‘Effect of cut-off, evaluation length, and measurement area in profile and areal surface texture characterization of as-built metal additive manufactured components’, *Applied Sciences (Switzerland)*, 11(11). Available at: https://doi.org/10.3390/app11115089

Nasir, N.S.M., Razab, M.K.A., Mamat, S., and Ahmad, M.I. (2016) ‘Review on welding residual stress’, *ARPN Journal of Engineering and Applied Sciences*, 11(9), pp. 6166–6175.

Ngo, T.D., Kashani, A., Imbalzano, G., Nguyen, K.T.Q., and Hui, D. (2018) ‘Additive manufacturing (3D printing): A review of materials, methods, applications and challenges’, *Composites Part B: Engineering*, 143(December 2017), pp. 172–196. Available at: https://doi.org/10.1016/j.compositesb.2018.02.012

Nicolas-Silvente, A.I., González-González, I., González-González, M., and González-González, J. (2020) ‘Influence of the titanium implant surface treatment on the surface roughness and chemical composition’, *Materials*, 13(2), pp. 1–13. Available at: https://doi.org/10.3390/ma13020314

Niinomi, M. (2008) ‘Biologically and mechanically biocompatible titanium alloys’, *Materials Transactions*, 49(10), pp. 2170–2178. Available at: https://doi.org/10.2320/matertrans.L-MRA2008828

Nsengimana, J. (2015) ‘An Investigation Into Surface Finish Improvement of Small Plastic Parts Manufactured Through Additive Manufacturing', Magister Technologiae: Engineering: Mechanical’, (September).

Nicolas-Silvente, A.I., González-González, I., González-González, M., and González-González, J.Pal, S. *et al.* (2021) ‘The effects of locations on the build tray on the quality of specimens in powder bed additive manufacturing’, *International Journal of Advanced Manufacturing Technology*, 112(3–4), pp. 1159–1170. Available at: https://doi.org/10.1007/s00170-020-06563-5

Paraschiv, A., Matache, G., Condruz, M.R., Frigioescu, T.F., and Pambaguian, L. (2022) ‘Laser powder bed fusion process parameters’ optimization for fabrication of dense IN 625’, *Materials*, 15(16). Available at: https://doi.org/10.3390/ma15165777

Pauzon, C., Raza, A., Hryha, E., and Forêt, P. (2019) ‘Effect of argon and nitrogen atmospheres on the properties of stainless steel 316 L parts produced by laser-powder bed fusion’, *Materials and Design*, 179. Available at: https://doi.org/10.1016/j.matdes.2019.107873

Pegues, J., Suresh, S., and Suresh, S. (2018) ‘Surface roughness effects on the fatigue strength of additively manufactured Ti-6Al-4V’, *International Journal of Fatigue*, 116(April), pp. 543–552. Available at: https://doi.org/10.1016/j.ijfatigue.2018.07.013

du Plessis, A. and Beretta, S. (2020) ‘Killer notches: The effect of as-built surface roughness on fatigue failure in AlSi10Mg produced by laser powder bed fusion’, *Additive Manufacturing*, 35, p. 101424. Available at: https://doi.org/10.1016/j.addma.2020.101424

Ponnusamy, P., Masood, S.H., Ruan, D., Palanisamy, S., and Rashid, R.A. (2021) ‘Investigating the effects of post-heat treatment on residual stress in AlSi12 parts processed with Selective Laser Melting’, *IOP Conference Series: Materials Science and Engineering*, 1067(1), p. 012117. Available at: https://doi.org/10.1088/1757-899x/1067/1/012117

Surface Roughness Terminology and Parameters, (2013) Parameter Definitions. Available at https://www.predev.com/pdffiles/surface_roughness_terminology_and_parameters.pdf

Rahmani, R., Lopes, S. I., and Prashanth, K. G. (2023) ‘Selective Laser Melting and Spark Plasma Sintering: A perspective on functional biomaterials’, *Journal of Functional Biomaterials*, 14(10), pp. 521. Available at: https://doi.org/10.3390/jfb14100521

Raji, S.A., Sahu, S., Bansal, R., and Varma, S. (2020) ‘Characteristic effects of alloying elements on β solidifying titanium aluminides: A review’, *Heliyon*, 6(7), p. e04463. Available at: https://doi.org/10.1016/j.heliyon.2020.e04463

Rashid, A. and Gopaluni, A. (2023) ‘A review of residual stress and deformation modeling for metal additive manufacturing processes’, *Chinese Journal of Mechanical Engineering: Additive Manufacturing Frontiers*, 2(4), p. 100102. Available at: https://doi.org/10.1016/j.cjmeam.2023.100102

Rausch, A.M., Schembecker, G., and Schmidt, M. (2017) ‘Predictive simulation of process windows for powder bed fusion additive manufacturing: influence of the powder bulk density’, *Materials*, 10(10). Available at: https://doi.org/10.3390/ma10101117

Rech, J. and Grzesik, W. (2023) ‘New trends in hybrid finishing processes of metallic additively fabricated parts – a short review’, *Journal of Machine Engineering*, 23(1), pp. 36–46. Available at: https://doi.org/10.36897/jme/162284

Ren, Z., Zhang, Z., Li, J., and Li, X. (2019) ‘Co–Cr–Mo alloys: Improved wear resistance through low-temperature gas-phase nitro-carburization’, *Surface and Coatings Technology*, 378(August), p. 124943. Available at: https://doi.org/10.1016/j.surfcoat.2019.124943

Riemer, A., Van der Stelt, J., Kessler, O., and Verleysen, P. (2014) ‘On the fatigue crack growth behavior in 316L stainless steel manufactured by selective laser melting’, *Engineering Fracture Mechanics*, 120, pp. 15–25. Available at: https://doi.org/10.1016/j.engfracmech.2014.03.008

Rodríguez, A., García, L., and Sánchez, M. (2012) ‘Surface improvement of shafts by the deep ball-burnishing technique’, *Surface and Coatings Technology*, 206(11–12), pp. 2817–2824. Available at: https://doi.org/10.1016/j.surfcoat.2011.11.045

Rosa, M.B., Medeiros, J.R., Ribeiro, F.V., and de Souza, J.C.M. (2012) ‘The influence of surface treatment on the implant roughness pattern’, *Journal of Applied Oral Science*, 20(5), pp. 550–555. Available at: https://doi.org/10.1590/S1678-77572012000500010

Rouf, S., Islam, S.M., Al-Shaer, M., and Ahmed, R. (2022) ‘Additive manufacturing technologies: Industrial and medical applications’, *Sustainable Operations and Computers*, 3(January), pp. 258–274. Available at: https://doi.org/10.1016/j.susoc.2022.05.001

Yang, Y., Chen, Z., Liu, Z., Wang, H., Zhang, Y., Wang K. and Wang, Di. (2019) ‘Influence of shielding gas flow consistency on parts quality consistency during large scale laser powder bed fusion’,pp.1-4. Available at: https://doi.org/10.1016/j.optlastec.2022.108899

Sahay, C. and Ghosh, S. (2018) ‘Understanding Surface Quality: Beyond Average Roughness (Ra)’, *ASEE Annual Conference and Exposition, Conference Proceedings*, 2018-June. Available at: https://doi.org/10.18260/1-2--31176

Saini, M. (2015) ‘Implant biomaterials: A comprehensive review’, *World Journal of Clinical Cases*, 3(1), p. 52. Available at: https://doi.org/10.12998/wjcc.v3.i1.52

Săndulescu, M., Sîrbu, V.D. and Popovici, I.A. (2023) ‘Bacterial species associated with peri-implant disease – a literature review’, *Germs*, 13(4), pp. 352–361. Available at: https://doi.org/10.18683/germs.2023.1405

Sansone, V., Pagani, D. and Melato, M. (2013) ‘The effects on bone cells of metal ions released from orthopaedic implants. A review’, *Clinical Cases in Mineral and Bone Metabolism*, 10(1), pp. 34–40. Available at: https://doi.org/10.11138/ccmbm/2013.10.1.034

Sarraf, M. *et al.* (2022) ‘A state-of-the-art review of the fabrication and characteristics of titanium and its alloys for biomedical applications’, *Bio-Design and Manufacturing*, 5(2), pp. 371–395. Available at: https://doi.org/10.1007/s42242-021-00170-3

Sedlaček, M., Podgornik, B. and Vižintin, J. (2009) ‘Influence of surface preparation on roughness parameters, friction and wear', *Wear*, 266(3–4), pp. 482–487. Available at: https://doi.org/10.1016/j.wear.2008.04.017

Sendino, S., García-Ruiz, J., Jiménez, J., and López, H. (2023) 'Effect of powder particle size distribution on the surface finish of components manufactured by laser powder bed fusion', *International Journal of Advanced Manufacturing Technology*, 124(3–4), pp. 789–799. Available at: https://doi.org/10.1007/s00170-022-10423-9

Shange, M., Yadroitsava, I., and du Preez, A. (2019) 'Surface morphology characterisation for parts produced by the high speed selective laser melting', *IOP Conference Series: Materials Science and Engineering*, 655(1). Available at: https://doi.org/10.1088/1757-899X/655/1/012045

Shange, M., Yadroitsava, I., and du Preez, A. (2022) 'Roughness and near-surface porosity of unsupported overhangs produced by high-speed laser powder bed fusion', *3D Printing and Additive Manufacturing*, 9(4), pp. 288–300. Available at: https://doi.org/10.1089/3dp.2020.0097

Shange, M., Yadroitsava, I., Pityana, S.P.I.Y., Yadroitsev, I., and du Plessis, A. (2019) 'Determining the Effect of Surface Roughness and Porosity At Different', *RAPDASA 2019 Conference Proceedings*, pp. 40–51.

Shen, H., Liu, Y., Zhang, Z., and Li, W. (2020) 'Influence of gas flow speed on laser plume attenuation and powder bed particle pickup in laser powder bed fusion', *JOM*, 72(3), pp. 1039–1051. Available at: https://doi.org/10.1007/s11837-020-04020-y

Shrestha, S. and Chou, K. (2022) 'Residual heat effect on the melt pool geometry during the laser powder bed fusion process', *Journal of Manufacturing and Materials Processing*, 6(6). Available at: https://doi.org/10.3390/jmmp6060153

Sibanda, P.S., Muir, J., and Matenga, B. (2019) 'State of the art in surface finish of metal additive manufactured parts', *Advances in Transdisciplinary Engineering*, 9(November), pp. 221–225. Available at: https://doi.org/10.3233/ATDE190039

Simson, D. and Subbu, S.K. (2022) 'Effect of process parameters on surface integrity of LPBF Ti6Al4V', *Procedia CIRP*, 108, pp. 716–721. Available at: https://doi.org/10.1016/j.procir.2022.03.111

Song, J.F. and Vorburger, T. V. (1991) 'Standard reference specimens in quality control of engineering surfaces', *Journal of Research of the National Institute of Standards and Technology*, 96(3), pp. 271–289. Available at: https://doi.org/10.6028/jres.096.015

Spierings, A.B., Herres, N. and Levy, G. (2010) 'Influence of the Particle Size Distribution on Surface Quality and Mechanical Properties in Additive Manufactured Stainless Steel Parts', *21st Annual International Solid Freeform Fabrication Symposium - An Additive Manufacturing Conference, SFF 2010*, pp. 397–406.

Smith, J., and Brown, A. (2021) 'Investigations on the Effect of Layers ' Thickness and Orientations in the Machining of Additively Manufactured', *Materials* [Preprint].

Subhedar, P. (2018) ‘Additive Manufacturing: A next gen fabrication’, *International Journal of Current Engineering and Technology*, 8(01). Available at: https://doi.org/10.14741/ijcet.v8i01.10893

Szczęsny, G., Ławniczak, M., and Majcherek, A. (2022) ‘A Review on biomaterials for orthopaedic surgery and traumatology: From past to present’, *Materials*, 15(10). Available at: https://doi.org/10.3390/ma15103622

Taghian, M., Ali, H., and Zhang, Y. (2023) ‘Laser powder bed fusion of metallic components: Latest progress in productivity, quality, and cost perspectives’, *Journal of Materials Research and Technology*, 27(September), pp. 6484–6500. Available at: https://doi.org/10.1016/j.jmrt.2023.11.049

Tamayo, J.A., González, F., and Rodríguez, J. (2021) ‘Additive manufacturing of Ti6Al4V alloy via electron beam melting for the development of implants for the biomedical industry’, *Heliyon*, 7(5). Available at: https://doi.org/10.1016/j.heliyon.2021.e06892

Tayebi, N. and Polycarpou, A.A. (2004) ‘Modeling the effect of skewness and kurtosis on the static friction coefficient of rough surfaces’, *Tribology International*, 37(6), pp. 491–505. Available at: https://doi.org/10.1016/j.triboint.2003.11.010

Tonietto, L., Oliveira, R. and Silva, F. (2019) ‘New method for evaluating surface roughness parameters acquired by laser scanning’, *Scientific Reports*, 9(1), pp. 1–16. Available at: https://doi.org/10.1038/s41598-019-51545-7

Yousefi, M. (2024). *The role of post surface finishing on the surface quality and fatigue behavior of Ti-6Al-4V alloy produced via Laser Powder Bed Fusion Additive Manufacturing process*. Politecnico di Torino. Available at: http://webthesis.biblio.polito.it/id/eprint/32634

Traore, S., Kermiche, M., Ebrahimi, F., and El-Mahdy, M. (2021) ‘Influence of gas atmosphere (Ar or He) on the laser powder bed fusion of a Ni-based alloy’, *Journal of Materials Processing Technology*, 288(May 2020), p. 116851. Available at: https://doi.org/10.1016/j.jmatprotec.2020.116851

Trevisan, F., Pavan, L., Taffarel, M., and Pereira, F. (2018) ‘Additive manufacturing of titanium alloys in the biomedical field: processes, properties and applications’, *Journal of Applied Biomaterials and Functional Materials*, 16(2), pp. 57–67. Available at: https://doi.org/10.5301/jabfm.5000371

Uhlmann, E., Moser, A., and Riemer, A. (2017) ‘Dynamical fatigue behavior of additive manufactured products for a fundamental life cycle approach’, *Procedia CIRP*, 61, pp. 588–593. Available at: https://doi.org/10.1016/j.procir.2016.11.138

Ullah, A., Ahmad, S., Ali, S., and Kim, S.S. (2022) ‘The influence of laser power and scanning speed on the microstructure and surface morphology of Cu2O parts in SLM’, *Rapid Prototyping Journal*, 28(9), pp. 1796–1807. Available at: https://doi.org/10.1108/RPJ-12-2021-0342

Ulusoy, U. (2023) ‘A review of particle shape effects on material properties for various engineering applications: from macro to nanoscale’, *Minerals*, 13(1). Available at: https://doi.org/10.3390/min13010091

Vaicelyte, A., Svarcova, A., Juvonen, R., and Yliniemi, S. (2020) ‘Cobalt–chromium dental alloys: Metal exposures, toxicological risks, CMR classification, and EU regulatory framework’, *Crystals*, 10(12), pp. 1–16. Available at: https://doi.org/10.3390/cryst10121151

Vrancken, B., Yasa, E., and Wauthle, R. (2012) ‘Heat treatment of Ti6Al4V produced by Selective Laser Melting: Microstructure and mechanical properties’, *Journal of Alloys and Compounds*, 541(0), pp. 177–185. Available at: https://doi.org/10.1016/j.jallcom.2012.07.022

Vukkum, V.B. and Gupta, R.K. (2022) ‘Review on corrosion performance of laser powder-bed fusion printed 316L stainless steel: Effect of processing parameters, manufacturing defects, post-processing, feedstock, and microstructure’, *Materials and Design*, 221, p. 110874. Available at: https://doi.org/10.1016/j.matdes.2022.110874

Wang, J., Zhang, S., and Wang, Y. (2023) ‘Understanding melt pool characteristics in laser powder bed fusion: An overview of single- and multi-track melt pools for process optimization’, *Advanced Powder Materials*, 2(4). Available at: https://doi.org/10.1016/j.apmate.2023.100137

Wang, Q., Zhang, Y., and Liu, Z. (2020) ‘Multi-scale surface treatments of titanium implants for rapid osseointegration: A review’, *Nanomaterials*, 10(6), pp. 1–27. Available at: https://doi.org/10.3390/nano10061244

Wang, Y., Zhang, Y., Li, X., and Zhu, H. (2023) ‘Residual stress reduction and surface quality improvement of dual-laser powder bed fusion’, *Additive Manufacturing*, 71(April), p. 103565. Available at: https://doi.org/10.1016/j.addma.2023.103565

Wang, Z., Yan, W., Liu, W.K. and Liu, M. (2019) ‘Powder-scale multi-physics modeling of multi-layer multi-track selective laser melting with sharp interface capturing method’, *Computational Mechanics*, 63(4), pp. 649–661. Available at: https://doi.org/10.1007/s00466-018-1614-5

Weaver, J., Schlenoff, A., Deisenroth, D. C. and Moylan, S. P. (2021) 'Inert gas flow speed measurements in laser powder bed fusion additive manufacturing', *NIST Advanced Manufacturing Series*, (100-43), p. 24. Available at: https://doi.org/10.6028/NIST.AMS.100-43

Wegner, N., Klein, M., Scholz, R., Kotzem, D., Macias Barrientos, M. and Walther, F. (2022) ‘Mechanical in vitro fatigue testing of implant materials and components using advanced characterization techniques’, *Journal of Biomedical Materials Research - Part B Applied Biomaterials*, 110(4), pp. 898–909. Available at: https://doi.org/10.1002/jbm.b.34970

Wennerberg, A. and Albrektsson, T. (2009) ‘Effects of titanium surface topography on bone integration: A systematic review’, *Clinical Oral Implants Research*, 20(SUPPL.

4), pp. 172–184. Available at: https://doi.org/10.1111/j.1600-0501.2009.01775.x

Yadroitsev, I., Bertrand, P. and Smurov, I. (2007) ‘Parametric analysis of the selective laser melting process’, *Applied Surface Science*, 253(19), pp. 8064–8069. Available at: https://doi.org/10.1016/j.apsusc.2007.02.088

Yadroitsev, I., Krakhmalev, P. and Yadroitsava, I. (2014) ‘Selective laser melting of Ti6Al4V alloy for biomedical applications: Temperature monitoring and microstructural evolution’, *Journal of Alloys and Compounds*, 583, pp. 404–409. Available at: https://doi.org/10.1016/j.jallcom.2013.08.183

Yadroitsev, I., du Plessis, A. and Yadroitsava, I. (2021) ‘Basics of laser powder bed fusion’, *Fundamentals of Laser Powder Bed Fusion of Metals*, (July), pp. 15–38. Available at: https://doi.org/10.1016/B978-0-12-824090-8.00024-X

Yánez, A., Fiorucci, M.P., Martel, O. and Cuadrado, A. (2022) ‘The influence of dimensions and powder recycling on the roughness and mechanical properties of Ti-6Al-4V parts fabricated by laser powder bed fusion’, *Materials*, 15(16). Available at: https://doi.org/10.3390/ma15165787

Yang, Y., Chen, Z., Liu, Z., Wang, H., Zhang, Y. and Wang, D. (2023) ‘Influence of shielding gas flow consistency on parts quality consistency during large-scale laser powder bed fusion’, *Optics and Laser Technology*, 158(PA), p. 108899. Available at: https://doi.org/10.1016/j.optlastec.2022.108899

Yildiz, R.A., Popa, A.A. and Malekan, M. (2024) ‘On the effect of small laser spot size on the mechanical behaviour of 316L stainless steel fabricated by L-PBF additive manufacturing’, *Materials Today Communications*, 38(January), p. 108168. Available at: https://doi.org/10.1016/j.mtcomm.2024.108168

Zhang, H., Vallabh, C.K.P. and Zhao, X. (2023) 'Influence of spattering on in-process layer surface roughness during laser powder bed fusion', *Journal of Manufacturing Processes*, 104, pp. 289–306. Available at: https://doi.org/10.1016/j.jmapro.2023.08.058

Zhang, T. and Liu, C.T. (2022) ‘Design of titanium alloys by additive manufacturing: A critical review’, *Advanced Powder Materials*, 1(1), p. 100014. Available at: https://doi.org/10.1016/j.apmate.2021.11.001

van Zyl, I., Yadroitsava, I. and Yadroitsev, I. (2016) ‘Residual stress in TI6AL4V objects produced by direct metal laser sintering’, *South African Journal of Industrial Engineering*, 27(4), pp. 134–141. Available at: https://doi.org/10.7166/27-4-1468

Appendix 1: Surface roughness parameters

Surface roughness parameters serve as quantitative indicators that characterize the texture of surfaces. These metrics are essential across multiple disciplines including manufacturing, engineering, and materials science. They offer critical insights into the quality, performance, and functionality of surfaces (Song *et al*., 1991). Any surface exhibiting peaks and valleys possesses a texture. The distinctions between peaks (upper amplitudes) and valleys (lower amplitudes) pertain to their elevation and the horizontal distance between them. Such variations arise from the processes involved in the surface's production or use (Bhushan, 2000).

A1.1. Sampling length (l)

This conceptual wavelength distinguishes between roughness and waviness, commonly referred to as cutoff Length or cutoff (Nagalingam et al., 2021).

A1.2. Evaluation length (L)

As depicted in Figure 79, this parameter (L) represents the cumulative length of five sampling segments, though any quantity of sampling lengths can be utilized. It is also referred to as evaluating length (Nagalingam *et al*., 2021).

A1.3. Mean line (M)

The parameter (M) depicted in Figure 79 serves as the reference line for identifying deviations in the profile. Generally, the mean line of the roughness profile is established using either digital or analog filters, which are terminated in accordance with the roughness sampling length (Precision Devices, 2013).

A1.4. Profile peak

This term refers to the highest point above the mean line (M) located between two intersections of the profile with the mean line in a segment that lies above it. (Precision Devices, 2013).

A1.5. Profile valley

This parameter denotes the lowest point relative to the mean line (M), situated between two crossings of the profile with the mean line.

A1.6. Roughness average (Ra)

Roughness average (Ra) shown in Figure 79 represents the average of the absolute values of the profile heights from the mean line. This parameter provides a solid overall description of height variation (Brown, 2012).

A1.7. RMS roughness (Rq)

RMS roughness (Rq) as depicted in Figure 79 is defined as the root mean square average of the profile heights within the analyzed area. This parameter reflects the deviations in surface height distribution, as shown Figure 79. It is notably more sensitive than the arithmetic average height (Sahay *et al.*, 2018). Serves as a crucial metric for quantifying surface irregularity through statistical approaches.

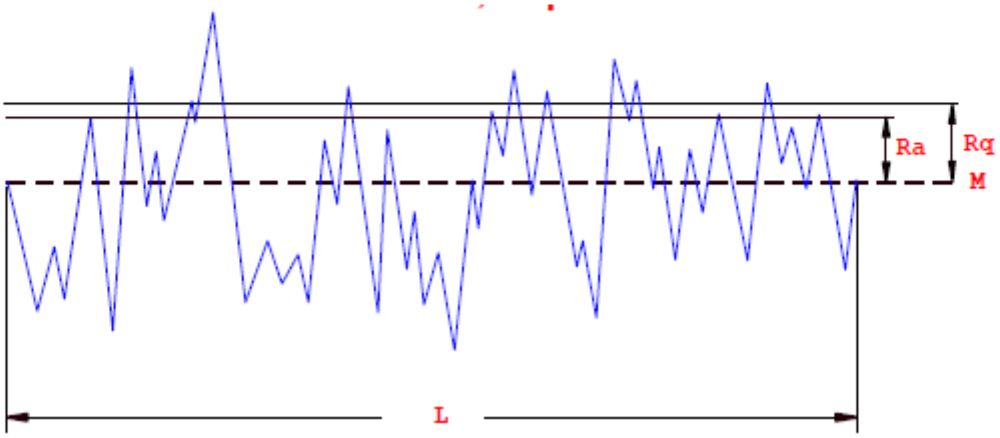

Figure 79 Length, mean line, arithmetic roughness, and root means square parameters (Keyence, 2001)

A1.8. Maximum profile peak height (Rp)

This parameter (Rp), as depicted in Figure 80, measures the vertical distance from the highest point of the profile to the mean line (Keyence, 2001).

A1.9. Maximum profile valley depth (Rv)

The parameter (Rv), as depicted in Figure 80, quantifies the vertical distance between the lowest point of the profile and the mean line (Keyence, 2001).

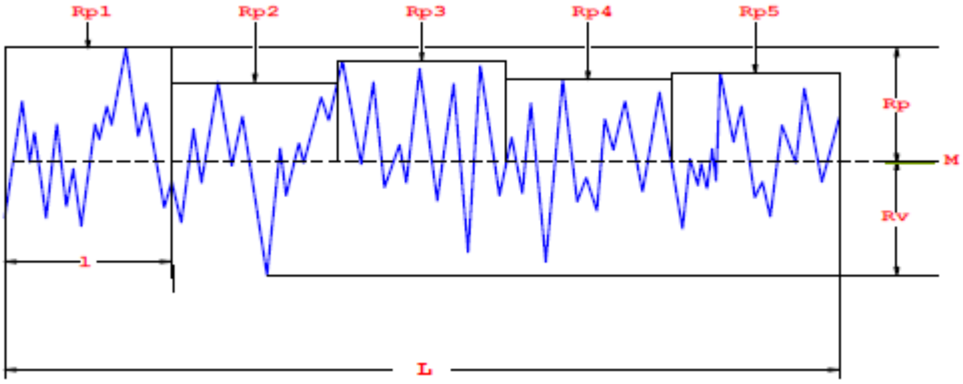

Figure 80 Maximum profile peak and valley (Keyence, 2001)

A1.10. Maximum height of the profile (Rt)

This parameter (Rt), as depicted in Figure 81, represents the vertical distance from the lowest point below the mean line to the highest point above it. This measurement is regarded as the maximum roughness of the profile (Gadelmawla *et al.*, 2002).

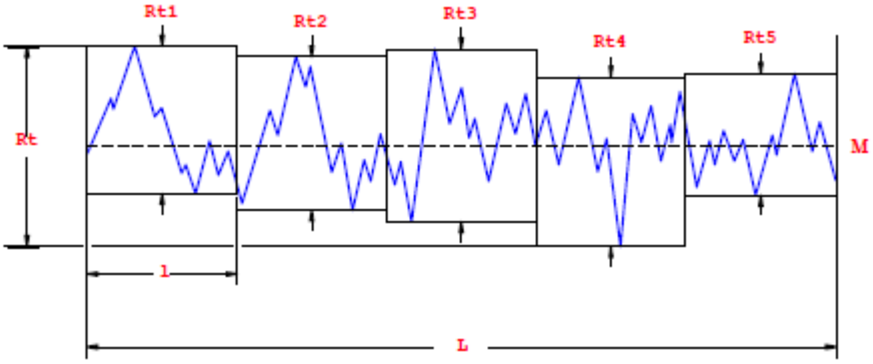

Figure 81 Maximum height of the profile (Keyence, 2001)

A1.11. Average maximum height of the profile (Rz),

Known as the ten-point height, this parameter (Rz) assesses the height of the tallest peaks and the depth of the lowest valleys in the profiles.

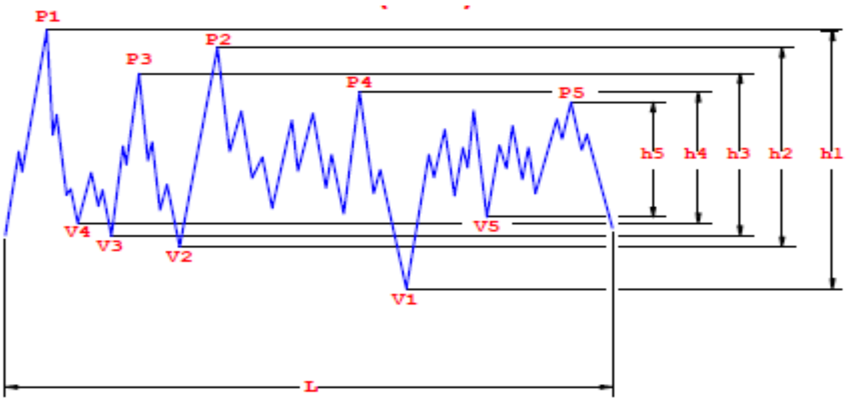

Figure 82 Average maximum height of the profile (Keyence, 2001)

A1.12. Core roughness (Rk)

This parameter signifies the primary height of the profile along the Y-axis of the BAC graph, which is generated by drawing a 40% line on the curve at the point of minimum gradient and extending the lines to 0% and 100% (Brown, 2012).

A1.13. Reduced peak height (Rpk)

This parameter defines the Y-axis height of a triangle comparable to the BAC curve from the 0% point to the Mr1 point (Tonietto *et al.*, 2019).

A1.14. Reduced valley depth (Rvk)

This parameter indicates the Y-axis height of a triangle that corresponds to the area of the BAC curve between Mr2 and 100% (Dimkovski, 2006).

A1.15. Peak height (Rpk)

This parameter denotes the distance from the highest profile peak to the intersection line of the surface ratio Mr1 (Dimkovski, 2006).

A1.16. Skewness (Rsk)

Skewness serves as a measure of the profile's asymmetry relative to the mean line. A negative skewness indicates a greater percentage of heights above the mean line, while a positive skewness suggests a higher percentage below it (Mitutoyo, 2010).

Ssk<0: Height distribution is skewed above the mean plane, as shown in Figure 83 (Mechanics and Processes, 2018).

Ssk = 0 Height distribution is symmetrical concerning the mean plane, as shown in Figure 83 (Mechanics and Processes, 2018).

Ssk > 0 Height distribution is skewed below the mean plane, as shown in Figure 83 (Mechanics and Processes, 2018).

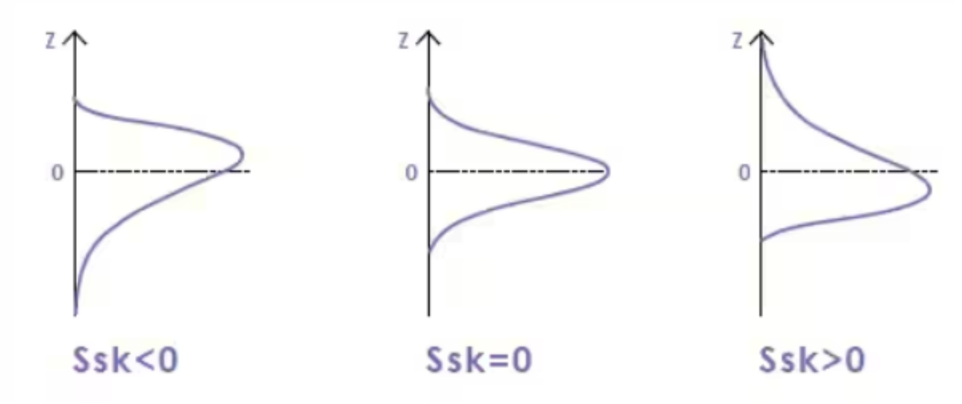

Figure 83 Skewness of the roughness

(https://www.keyence.com/ss/products/microscope/roughness/surface/ssk-skewness.jsp)

A1.17. Kurtosis (Sku, Pku, Wku)

Kurtosis values are utilized to assess the sharpness of the roughness (Hansson *et al*, 2011).

Sku < 3: The height distribution is skewed above the mean plane, Figure 84a (Sedlaček *et al.*, 2009).

Sku=3: Represents a normal height distribution with both sharp and indented sections (Sedlaček *et al*., 2009).

Sku>3: Indicates a spiked height distribution, see Figure 84b (Tayebi *et al*., 2004).

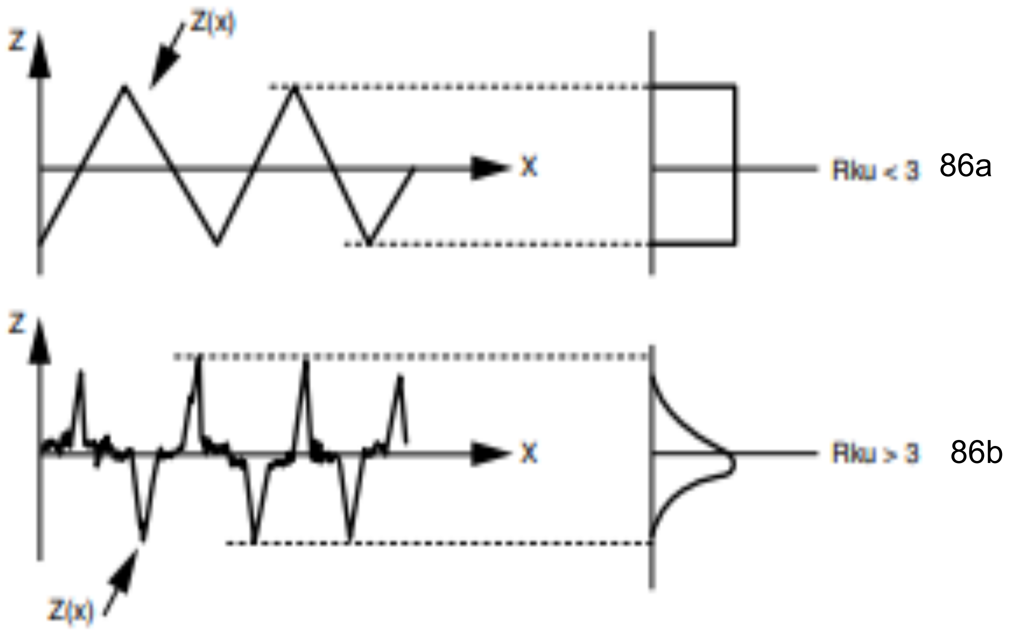

Figure 84: Kurtosis (Mechanics and Processes, 2018)

A1.18. Waviness parameters

As depicted in Figure 85, waviness refers to surface irregularities that occur over longer intervals than roughness, defined as deviations from an ideal surface that recur at greater depths. Factors contributing to surface waviness may include tool or workpiece deflection, excessive temperature leading to deformation, uneven lubrication, improper manufacturing processes, vibration, and machine tool flexibility (Mechanics and Processes, 2018).

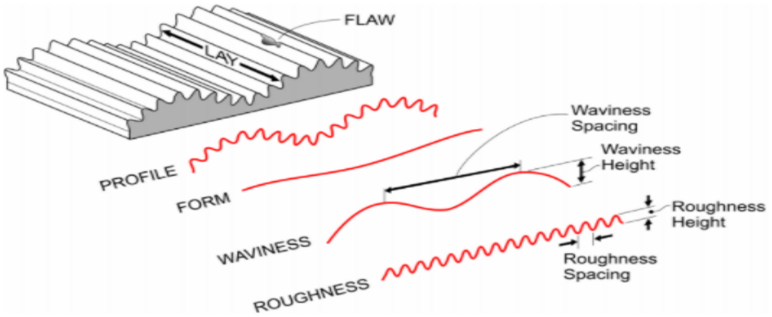

Figure 85 Waviness profile (Mechanics and Processes, 2018)

When analyzing the surface roughness of laser powder bed fusion (LPBF)-fabricated Ti6Al4V implants, two key parameters in roughness measurement are: sampling length and evaluation length. Both parameters are crucial for obtaining accurate and representative roughness data for biomedical applications, where surface texture affects osseointegration, mechanical properties, and wear resistance.

Typical sampling and evaluation lengths for Ti6Al4V implants

Surface type	**Sampling length (L_r)**	**Evaluation length (L_e)**	**Reference**
As-built LPBF surface	0.8 mm–2.5 mm	4 mm–12 mm	ISO 4288
Post-processed (Polished)	0.25 mm–0.8 mm	1.25 mm–4 mm	ASTM F42
Textured for osseointegration	2.5 mm–4 mm	10 mm–20 mm	Journal of Biomedical Materials Research

Appendix 2. Surface finishing methods

A2.1. Manual finishing (Sibanda *et al.*, 2019)

It is a method for enhancing the surface quality of metal parts produced through AM; manual finishing employs techniques such as sanding, filing, or polishing carried out by skilled workers using hand tools or portable machinery. Although this method is labour-intensive and requires a significant time investment, it presents notable benefits for small or intricately designed components that demand precise finishes.

Benefits

- Particularly effective for complex features or locations inaccessible to automated machinery
- Allows for a high level of control throughout the finishing process
- Well-suited for prototype components or custom applications where uniformity is not a critical factor

Limitations

- Elevated labour costs due to the manual nature of the work involved
- Quality can be inconsistent, relying heavily on the skill level of the operator
- Not practical for mass production scenarios

A2.2. Mass finishing (Sibanda *et al.*, 2019)

Mass finishing is a technique that processes numerous parts at once within a container filled with abrasive materials. The abrasive media, in conjunction with mechanical movements such as vibratory, centrifugal, or tumbling actions, interacts with the components to refine surfaces, eliminate burrs, and enhance overall texture.

Benefits:

- Suitable for batch processing, rendering it economical for large-scale production
- Capable of handling a diverse range of materials and component shapes

Limitations:

- Less effective on complex or internal geometries
- Surface textures may differ based on the type of media used and the orientation of the parts

A2.3. Burnishing (Rodríguez *et al.*, 2012)

Burnishing is a technique used to smooth and solidify a piece of work's surface. It is commonly used to remove the minuscule peaks and valleys from the surface of a workpiece that has already been fabricated (Charfeddine *et al.*, 2021). This process improves surface quality by applying pressure to deform the material's exterior plastically. Compressing surface imperfections results in a finish that is smoother, harder, and more polished. This method is an economical non-material-removing approach utilized in various industries to enhance both the functional and visual properties of components. A rigid and smooth burnishing instrument, such as a hard roller ball or roller, is utilized on the surface of a component (Figure 86). As the tool traverses the surface, it exerts pressure, leading to localized plastic deformation. The high points of the surface material are displaced into the low points resulting in a more polished finish without the removal of any material.

Benefits:

- Minimizes surface roughness down to micro or even nano-scale dimensions
- Increases surface hardness through the process of strain hardening
- Fills in surface micro-cracks, thereby lowering the risk of corrosion
- Eliminates surface stress concentrations that can lead to crack formation, improving the durability of components
- Maintains material integrity since the process does not involve any material removal

Limitations:

- Requires materials capable of plastic deformation without breaking
- Difficult to implement effectively on complex geometries
- Needs a pre-machined surface with a moderate degree of roughness to achieve the best results

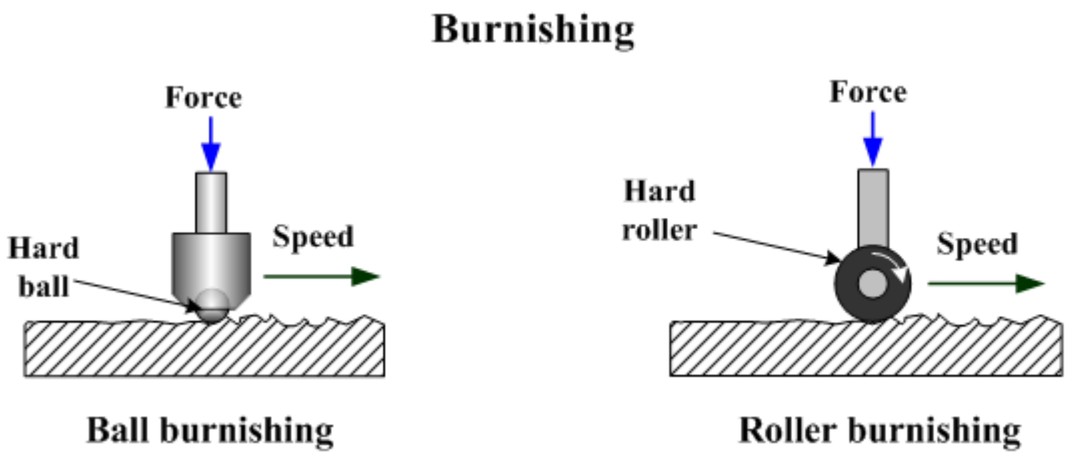

Figure 86 Demonstration of burnishing (Rodríguez *et al.*, 2012)

A2.4 Media blasting (Sibanda *et al.*, 2019)

Media blasting is a mechanical post-processing method used to enhance the surface finish of components created through AM. This technique involves shooting abrasive particles at high velocities onto the surface of the part, which helps eliminate imperfections, decrease roughness, and enhance overall appearance. It is especially beneficial for AM parts with external surfaces, as it proficiently addresses surface irregularities that arise from the layer-by-layer printing process.

Limitations:

- Less effective for internal features or those with complex shapes

Benefits:

- Minimizes surface roughness while improving both the aesthetic and functional

A2.5 Peening (Sibanda *et al.*, 2019)

Shot peening is a mechanical finishing technique designed to improve the surface characteristics of a material by inducing compressive residual stresses. This is accomplished by propelling small particles commonly made of metal, glass, or ceramic at high speeds onto the material's surface. The process enhances fatigue resistance, reduces the likelihood of stress corrosion cracking, and boosts wear resistance.

Benefits:

- The introduction of compressive stresses aids in preventing the initiation and growth of cracks
- Lowers the chances of stress corrosion cracking in environments prone to corrosion
- Strengthens the surface making it less susceptible to wear and abrasion
- Utilizing different types and sizes of particles allows for the achievement of various surface finishes

Limitations:

- The peening process may elevate surface roughness, necessitating further finishing processes if a smooth finish is essential
- Requires meticulous control over various parameters (such as shot velocity and coverage) to guarantee consistent outcomes
- Most effective on ductile materials that can undergo plastic?

A2.6 CNC finishing (Sibanda *et al.*, 2019)

This type of finishing is mainly used in the process of precision machining, which is done in order to improve the surface quality of a part after it has been initially manufactured. CNC machines are very efficient in removing irregularities on the surface as well as accurate in terms of dimensions, especially on plane or curved surfaces. These machines are applied for the post-processing of AM components, especially for the external characteristics or surfaces that need to meet certain tolerance values.

Limitations:

CNC finishing is not ideal for intricate internal geometries or lattice structures, which are often encountered in state-of-the-art AM components.

A2.7 Chemical polishing (Sibanda *et al.*, 2019)

Chemical polishing is one of the finishing processes that are employed in AM manufacturing. This surfaces method of involves acids such as HNO_3, HF, HCl and H_2SO_4

Benefits

- Provides a consistent surface finish, especially in challenging areas such as internal channels and complex designs
- Generates minimal mechanical stress when compared to abrasive methods
- Effectively diminishes surface roughness, aligning with high-quality requirements, particularly in sectors such as aerospace and medical

Limitations

- Requires careful regulation of chemical solutions and process parameters to prevent over-removal of material or inconsistencies in the finish
- Involves potential environmental and safety issues related to the management of chemical waste

A2.8 Electrochemical polishing (Sibanda *et al.*, 2019)

Electropolishing is a surface treatment method that involves the removal of a thin layer of metal by an electrochemical process. This process enhances the finish of the surface by polishing it to a smooth and glossy finish as well as increasing its resistance to corrosion. Due to its capability of providing a very effective and smooth surface finish, electropolishing is widely used where there is a need for high accuracy and hygiene. In this process, the metal component acts as an anode, as shown in Figure 87, placed inside an electrolytic cell (usually an acidic solution) along with a nearby conductive cathode. When a direct current (DC) is supplied, the surface material is removed from the anode. This dissolution takes place at different rates, with the peaks of the surface being removed at a faster rate than the valleys, leading to the formation of a smooth and polished surface.

Benefits

- Achieves a reduction in roughness to sub-micron levels and imparts a reflective surface
- The process eliminates surface impurities, thereby enhancing resistance to oxidation and corrosion
- Produces a clean, passivated surface that is ideal for use in the food, medical, and pharmaceutical industries
- As a non-contact process, it avoids introducing any mechanical stresses or deformations
- Results in a bright mirror-like finish

Limitations

- This technique is limited to metals that are electrically conductive and chemically compatible, including stainless steel, aluminium, and titanium
- The process necessitates specialized equipment and chemicals, which can lead to high initial costs
- Challenges may arise when dealing with large components or complex internal geometries

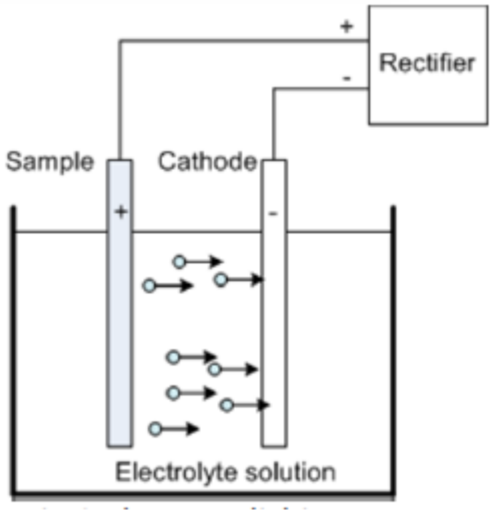

Figure 87: Schematic of electropolishing process (Schupbach et al., 2005)

A2.9 Chemical abrasive flow (Sibanda *et al.*, 2019)

This method integrates both chemical and abrasive processes to achieve a smooth and polished finish on a component. This method utilizes a mixture of abrasive particles dispersed in a thick fluid that flows across the component's surface. The movement of the fluid facilitates material removal, while the chemical agents work to dissolve or soften any surface flaws. The abrasives aid in the physical refinement of the surface, while the chemical agents help in removing any lingering imperfections.

Benefits

- It effectively reaches hard-to-access regions and internal shapes, making it particularly useful for components with complex designs or internal passages
- This method greatly reduces surface roughness while minimizing thermal stress, making it beneficial for components that need a precise finish without the danger of heat-related damage
- It is notably effective when used in conjunction with other finishing methods to achieve superior surface characteristics in intricate geometries

A2.10 Electrical discharge machining (Sibanda *et al.*, 2019)

Electrical discharge machining (EDM) utilizes electrical discharges or sparks generated between an electrode and the workpiece to remove surface imperfections through a process of melting and erosion. The standard procedure for EDM includes positioning a conductive workpiece near an electrode, which is typically made from materials such as copper, graphite, or tungsten. Both elements are submerged in a dielectric fluid, often oil or deionized water. A series of electrical discharges take place between the electrode and the workpiece producing localized heat that melts the material at the point of discharge. The high temperature resulting from the spark causes the surrounding material to melt and vapourize. The dielectric fluid serves to eliminate the eroded particles preventing debris from interfering with the machining operation. Material is gradually removed in layers allowing for precise control over surface texture and achieving smoother finishes compared to traditional machining methods. However, this process can lead to the formation of heat-affected zones (HAZ), which may modify surface properties if not effectively managed. To achieve the desired surface quality, additional post-processing techniques such as polishing or further EDM cycles may be necessary. Surface quality additional post-processing methods such as polishing or further EDM cycles may be employed.

A2.11 Thermal deburring (Sibanda *et al.*, 2019)

Thermal deburring is a technique used to remove burrs and surface irregularities from difficult-to-access areas of a workpiece, especially within complex geometries. This method employs heated gases to rapidly raise the temperature of the burrs or unwanted materials to a combustion level resulting in a smooth surface finish. However, the process may leave a thin oxide layer or recast layer on the component and could induce residual tensile stress due to the rapid heating and cooling cycles. Typically, this technique involves a swift burst of hot gas produced by a combustion reaction directed at the workpiece. The thermal energy effectively eliminates burrs without requiring direct contact, making it particularly suitable for fragile or intricate components.

Benefits

- Thermal deburring is particularly effective for finishing components made from tough materials and for cleaning internal channels or geometries that are not easily accessed with mechanical tools

A2.12 Laser polishing (Sibanda *et al.*, 2019)

Laser polishing is a surface finishing technique that uses thermal energy to improve the quality of metallic components, especially those produced through AM. This method involves selectively melting and re-solidifying the surface layer, effectively reducing roughness and enhancing gloss.

Benefits

- This technique can significantly decrease surface roughness resulting in a smoother and more reflective finish compared to the original condition
- It allows for selective polishing of specific areas of a part which is especially beneficial for complex geometries or small features where traditional mechanical polishing may be difficult

- As a non-contact process, it prevents mechanical wear and deformation of the component, making it suitable for delicate or intricate designs

Limitations

- The rapid heating and cooling cycles associated with laser polishing may create residual tensile stresses in the material, potentially affecting the mechanical properties of the component
- The equipment needed for laser polishing can be expensive, and the process itself is generally costlier than conventional mechanical finishing methods

Appendix 3. Surface roughness data

Parameter	ISO 427:1997
Average roughness	Ra
Root means square	Rq
Ten point height	Rz
Number of measurements	N

- For all vertical and horizontal samples in an as-built state and after surface finishing, the measurements were taken three times (N=3)
- For all the semisphere samples in an as-built state and after surface finishing, the measurements were taken five times (N=5)
- All surface roughness data is shown in µm, average value ± standard deviation

As-built surface roughness data

Sample 1 (vertical, Zone 3)

Parameter	Top surface	Side A surface	Side B surface
Ra	8,8 ± 3,06	8,3 ± 1,07	8,9 ± 0,42
Rq	10,9 ± 3,50	10,1 ± 1,24	10,5 ± 0,29
Rz	49,9 ± 0,15	47,0 ± 5,89	47,7 ± 0,86

Sample 2 (semisphere, Zone 3)

Parameter	Side surface
Ra	7,1 ± 0,57
Rq	8,8 ± 0,71
Rz	41,9 ± 0,91

Sample 3 (horizontal, Zone 6)

Parameter	Top surface	Side A surface	Side B surface
Ra	9,9 ± 1,04	11,1 ± 1,78	8.0 ± 0,07
Rq	12,3 ± 0,36	13,5 ± 2,20	9,8 ± 0,20
Rz	59,6 ± 0.68	59,5 ± 4,49	44,1 ± 1,06

Sample 4 (vertical, Zone 6)

	Top surface	Side A surface	Side B surface
Parameter	Average ± S.D.	Average ± S.D.	Average ± S.D.
Ra	9,5 ± 1,05	12,2 ± 1,17	8,6 ± 0,47
Rq	12,6 ± 0,82	15,3 ±1,26	10,7 ± 0,45
Rz	51,1 ± 12,94	68,3 ± 1,89	49,2 ± 1,30

Sample 5 (horizontal, Zone 9)

	Top surface	Side A surface	Side B surface
Parameter	Average ± S.D.	Average ± S.D.	Average ± S.D.
Ra	9,9 ± 1,07	9,7 ± 0,23	8,2 ± 0,12
Rq	12,0 ± 0,02	12,1 ± 0,17	10,0 ± 0,29
Rz	52,7 ± 0.94	56,1 ± 3,79	43,4 ± 2,20

Sample 6 (semisphere, Zone 9)

	Side surface
Parameter	Average ± S.D.
Ra	9,0
Rq	11,4
Rz	60,5

Sample 7 (semisphere, Zone 3)

	Side surface
Parameter	Average ± S.D.
Ra	8,9 ± 1,64
Rq	11,1 ± 2,01
Rz	55,9 ± 5,52

Sample 8 (horizontal, Zone 3)

	Top surface	Side A surface	Side B surface
Parameter	Average ± S.D.	Average ± S.D.	Average ± S.D.
Ra	9,3 ± 0,36	9,4 ± 0,28	8,4 ± 0,53
Rq	12,6 ± 0,71	11,7 ± 0,39	10,4 ± 0,63
Rz	58,3 ±0.35	57,0 ± 10,73	44,9 ± 1,81

Sample 9 (semisphere, Zone 6)

	Side surface
Parameter	Average ± S.D.
Ra	9,5 ± 1,01
Rq	11,5 ± 0,98
Rz	55,8 ± 2,18

Sample 10 (semisphere, Zone 6)

	Side surface
Parameter	Average ± S.D.
Ra	9,7 ± 0,87
Rq	11,7 ± 1,06
Rz	52,7 ± 3,37

Sample 11 (semisphere, Zone 9)

	Side surface
Parameter	Average ± S.D.
Ra	10,9 ± 0,57
Rq	13,2 ± 0,71
Rz	59,8 ± 0,91

Sample 12 (vertical, Zone 9)

	Top surface	Side A surface	Side B surface
Parameter	Average ± S.D.	Average ± S.D.	Average ± S.D.
Ra	10,8 ± 0,44	12,4 ± 1,43	11,8 ± 0,62
Rq	13,6 ± 1,26	15,4 ± 1,98	14,3 ± 0,62
Rz	59,3 ± 1,36	68,7 ± 10,10	61,4 ± 0,94

Sample 13 (horizontal, Zone 2)

	Top surface	Side A surface	Side B surface
Parameter	Average ± S.D.	Average ± S.D.	Average ± S.D.
Ra	10,0 ± 1,04	8,4 ± 0,70	9,9 ± 0,41
Rq	11,8 ± 1,00	10,4 ± 1,11	11,9 ± 0,68
Rz	65,1 ± 0,17	48,1 ± 6,18	52,4 ± 5,33

Sample 14 (vertical, Zone 2)

	Top surface	Side A surface	Side B surface
Parameter	Average ± S.D.	Average ± S.D.	Average±S.D.
Ra	10,8 ± 0,47	9,0 ± 0,55	9,4 ± 0,57
Rq	13,1 ± 1,57	11,0 ± 0,44	11,6 ± 0,70
Rz	58,0 ± 0,93	49,4 ± 2,57	52,5 ± 4,79

Sample 15 (horizontal, Zone 5)

	Top surface	Side A surface	Side B surface
Parameter	Average ± S.D.	Average ± S.D.	Average ± S.D.
Ra	10,4 ± 0,46	8,7 ± 0,84	9,4 ± 0,25
Rq	13,6 ± 0,30	10,8 ± 1,03	11,3 ± 0,27
Rz	59,1 ± 0,32	63,5 ± 7,00	52,4 ± 5,33

Sample 16 (horizontal, Zone 5)

	Top surface	Side A surface	Side B surface
Parameter	Average ± S.D.	Average ± S.D.	Average±S.D.
Ra	10,1 ± 0,11	8,8 ± 0,28	10,5 ± 1,07
Rq	13,6 ± 0,78	10,9 ± 0,54	12,8 ± 1,08
Rz	56,8 ± 1,11	49,5 ± 3,51	54,8 ± 3,52

Sample 17 (vertical, Zone 8)

	Top surface	Side A surface	Side B surface
Parameter	Average ± S.D.	Average ± S.D.	Average ± S.D.
Ra	12,5 ± 3,28	11,3 ± 0,72	11,8 ± 1,59
Rq	15,3 ± 4,24	14,1 ± 0,79	14,5 ± 1,88
Rz	65,8 ± 7,18	66,4 ± 4,50	65,6 ± 4,97

Sample 18 (semisphere, Zone 8)

	Side surface
Parameter	Average ± S.D.
Ra	11,046
Rq	13,86167
Rz	71,60233

Sample 19 (vertical, Zone 2)

	Top surface	Side A surface	Side B surface
Parameter	Average ± S.D.	Average ± S.D.	Average ± S.D.
Ra	10,6 ± 0,10	9,5 ± 1,29	10,5 ± 1,22
Rq	15,3 ± 4,24	14,1 ± 0,79	14,5 ± 1,88
Rz	65,8 ± 7,18	66,4 ± 4,50	65,6 ± 4,97

Sample 20 (horizontal, Zone 2)

	Top surface	Side A surface	Side B surface
Parameter	Average ± S.D.	Average ± S.D.	Average ± S.D.
Ra	10,0 ± 1,20	8,7 ± 1,02	8,4 ± 0,69
Rq	12,5 ± 0,58	10,7 ± 1,44	10,3 ± 0,91
Rz	57,9 ± 1,15	47,7 ± 6,95	44,5 ± 3,91

Sample 21 (vertical, Zone 5)

	Top surface	Side A surface	Side B surface
Parameter	Average ± S.D.	Average ± S.D.	Average±S.D.
Ra	10,5 ± 0,19	9,1 ± 1,31	10,6 ± 0,51
Rq	13,6 ± 1,24	12,2 ± 1,20	13,1 ± 0,75
Rz	60,4 ± 3,18	55,8 ± 8,02	57,3 ± 4,40

Sample 22 (semisphere, Zone 8)

	Side surface
Parameter	Average ± S.D.
Ra	10,8 ± 0,57
Rq	13,2 ± 0,71
Rz	66,0 ±0,91

Sample 23 (horizontal, Zone 8)

	Top surface	Side A surface	Side B surface
Parameter	Average ± S.D.	Average ± S.D.	Average ± S.D.
Ra	10,2 ± 0,24	11,9 ± 1,87	11,6 ± 1,11
Rq	12,5 ± 0,60	14,4 ± 2,15	14,5 ± 0,93
Rz	51.5 ± 0,51	59,5 ± 8,10	52,4 ± 5,33

Sample 24 (semisphere, Zone 2)

	Side surface
Parameter	Average ± S.D.
Ra	9,2 ±0,57
Rq	11,3 ± 0,71
Rz	62,7 ± 0,91

Sample 25 (vertical, Zone 2)

	Top surface	Side A surface	Side B surface
Parameter	Average ± S.D.	Average ± S.D.	Average ± S.D.
Ra	10,4 ± 0,11	9,931,40?	10,1 ± 0,67
Rq	12,8 ± 0,57	12.0 ± 1,59	12,3 ± 0,68
Rz	55,9 ± 4,52	51,1 ± 3,52	50,0 ± 1,53

Sample 26 (semisphere, Zone 5)

	Side surface
Parameter	Average ±S.D.
Ra	11,0 ± 0,17
Rq	13,9 ± 2,10
Rz	71,6 ± 10,18

Sample 27 (horizontal, Zone 5)

	Top surface	Side A surface	Side B surface
Parameter	Average ± S.D.	Average ± S.D.	Average ± S.D.
Ra	12,0 ± 1,09	9,6 ± 0,22	9,3 ± 0,49
Rq	14,9 ± 1,14	11,9 ± 0,34	11,3 ± 0,59
Rz	65,3 ± 0,33	51,7 ± 3,97	46,9 ± 3,37

Sample 28 (vertical, Zone 8)

	Top surface	Side A surface	Side B surface
Parameter	Average ± S.D.	Average ± S.D.	Average ± S.D.
Ra	11,0 ± 0,39	11,2 ± 1,47	11,3 ± 0,54
Rq	14,2 ± 2,36	14,1 ± 1,97	13,9 ± 0,67
Rz	63,1 ± 7,95	63,5 ± 7,00	50,0 ± 1,53

Sample 29 (vertical, Zone 2)

	Top surface	Side A surface	Side B surface
Parameter	Average ± S.D.	Average ± S.D.	Average ± S.D.
Ra	11,6 ± 0,10	10,3 ± 0,63	10,8 ± 0,79
Rq	14,5 ± 2,73	12,6 ± 0,86	13,3 ± 0,96
Rz	65,3 ± 11,83	55,7 ± 2,44	60,5 ± 6,60

Sample 30 (semisphere, Zone 2)

	Side surface
Parameter	Average ± S.D.
Ra	8,9 ± 0,57
Rq	10,9 ± 0,71
Rz	50,0 ± 0,91

Sample 31(horizontal, Zone 5)

	Top surface	Side A surface	Side B surface
Parameter	Average ± S.D.	Average ± S.D.	Average ± S.D.
Ra	10,1 ± 0,09	9,1 ± 1,31	11,3 ± 1,64
Rq	13,2 ± 0,30	11,1 ± 1,36	13,8 ± 1,70
Rz	79,0 ± 0,12	47,5 ± 2,48	58,4 ± 6,40

Sample 32 (semisphere, Zone 5)

	Side surface
Parameter	Average ± S.D.
Ra	10,3 ± 1,87
Rq	11,4 ± 2,43
Rz	54,5 ± 12,10

Sample 33 (horizontal, Zone 8)

	Top surface	Side A surface	Side B surface
Parameter	Average ± S.D.	Average ± S.D.	Average ± S.D.
Ra	10,7 ± 0,79	10,3 ± 2,16	11,2 ± 0,21
Rq	13,2 ± 0,33	10,9 ± 1,09	13,6 ± 0,52
Rz	61,0 ± 0,02	53,2 ± 12,87	56,4 ± 2,32

Sample 34 (semisphere, Zone 8)

	Side surface
Parameter	Average ± S.D.
Ra	11,1 ± 0,0,87
Rq	13,3 ± 0,83
Rz	58,2 ± 0,41

Sample 35 (horizontal, Zone 1)

	Top surface	Side A surface	Side B surface
Parameter	Average ± S.D.	Average ± S.D.	Average ± S.D.
Ra	12,5 ± 0,61	9,4 ± 0,39	10,1 ± 1,70
Rq	12,3 ± 0,31	11,3 ± 1,22	12,4 ± 1,65
Rz	57,2,0 ± 0,27	48,5 ± 2,01	59,1 ± 5,11

Sample 36 (vertical, Zone 1)

	Top surface	Side A surface	Side B surface
Parameter	Average ± S.D.	Average ± S.D.	Average S.D.
Ra	11,5 ± 0,91	9,86 ± 1,32	11,55 ± 0,87
Rq	13,1 ± 0,67	12,00 ± 1,39	14,27 ± 0,89
Rz	55,9 ± 4,51	53,19 ± 4,00	59,97 ± 2,38

Sample 37 (semisphere, Zone 4)

	Side surface
Parameter	Average ± S.D.
Ra	10,5
Rq	13,0
Rz	68,01

Sample 38 (semisphere, Zone 7)

	Side surface
Parameter	Average ± S.D.
Ra	11,7
Rq	14,2
Rz	71,9

Sample 39 (vertical, Zone 7)

	Top surface	Side A surface	Side B surface
Parameter	Average ± S.D.	Average ± S.D.	Average ± S.D.
Ra	10,6 ± 0,10	9,5 ± 1,29	10,5 ± 1,22
Rq	13,0 ± 0,51	11,6 ± 1,40	12,1 ± 0,65
Rz	57,9 ± 1,22	51,1 ± 3,52	50,0 ± 1,53

Sample 40 (vertical, Zone 1)

	Top surface	Side A surface	Side B surface
Parameter	Average ± S.D.	Average ± S.D.	Average ± S.D.
Ra	10,6 ± 0,09	10,3 ± 0,65	13,3 ± 0,13
Rq	12,9 ± 0,51	12,7 ± 0,62	16,0 ± 0,16
Rz	58,5 ± 0,04	54,9 ± 1,84	65,1 ± 1,90

Sample 41(horizontal, Zone 1)

	Top surface	Side A surface	Side B surface
Parameter	Average ± S.D.	Average ± S.D.	Average ± S.D.
Ra	11,2 ± 0,19	9,0 ± 1,54	11,7 ± 0,81
Rq	14,0 ± 0,01	13,2 ± 0,91	14,3 ± 0,98
Rz	66,1 ± 0,14	64,4 ± 19,44	58,9 ± 3,63

Sample 42 (vertical, Zone 4)

	Top surface	Side A surface	Side B surface
Parameter	Average ± S.D.	Average ± S.D.	Average ± S.D.
Ra	11,0 ± 0,44	10,8 ± 0,38	13,7 ± 0,42
Rq	13,8 ± 1,68	13,3 ± 0,52	16,6 ± 0,40
Rz	64,1 ± 9,63	62,5 ± 3,25	71,6 ± 2,38

Sample 43 (horizontal, Zone 4)

	Top surface	Side A surface	Side B surface
Parameter	Average ± S.D.	Average ± S.D.	Average ± S.D.
Ra	11,2 ± 0,45	10,6 ± 0,85	10.0 ± 0,39
Rq	13,1 ± 0,06	13,2 ± 1,09	12,3 ± 0,35
Rz	59,8 ± 0,93	60,1 ± 2,64	53.0 ± 1,74

Sample 44 (vertical, Zone 7)

	Top surface	Side A surface	Side B surface
Parameter	Average ± S.D.	Average ± S.D.	Average ± S.D.
Ra	11,4 ± 0,05	12,1 ± 0,87	13,4 ± 0,81
Rq	13,7 ± 1,45	14,8 ± 0,89	16,6 ± 0,83
Rz	60,2 ± 2,97	66,7 ± 6,14	73,7 ± 4,09

Sample 45 (horizontal, Zone 7)

	Top surface	Side A surface	Side B surface
Parameter	Average ± S.D.	Average ± S.D.	Average ± S.D.
Ra	11,1 ± 0,15	10,5 ± 0,66	10,5 ± 1,26
Rq	13,9 ± 0,99	13.0 ± 0,69	13,2 ± 1,57
Rz	56,7 ± 0,88	62,4 ± 8,39	59,8 ± 5,72

Surface roughness data after dry electropolishing

N=3						
Horizontal samples				**Vertical samples**		
Ra				**Ra**		
Zones	30 minutes of polishing	60 minutes of polishing	120 minutes of polishing	30 minutes of polishing	60 minutes of polishing	120 minutes of polishing
Zone	Average±S.D.	Average±S.D.	Average±S.D.	Average±S.D.	Average±S.D.	Average±S.D.
1	9,4±0,31	9,1±0,18	8,3±0,21	9,5±0,38	9,3±0,23	8,5±0,32
3	8,8±0,16	8,2±0,08	6,8±0,29	8,6±1,2	8,3±0,03	7,4±0,37
5	8,3±0,14	8±0,39	6,6±0,30	10,3±0,57	9,6±0,45	7,9±0,75
7	10,5±0,24	9,3±0,38	8,05±0,54	10,3±0,76	9,2±0,86	8,8±0,51
9	12,3±0,40	11±0,46	8,65±0,23	9,8±0,18	8,6±0,26	8,2±0,47
Rq				**Rq**		
1	12,4±0,19	11,5±0,44	9,3±0,40	11,4±0,65	11,2±0,32	10,5±0,09
3	11,3±0,50	10,87±0,77	9,6±0,36	10,2±0,11	10,3±0,26	9,6±0,70
5	11,5±0,05	10,8±0,32	9,5±0,31	12,5±0,37	12,4±0,56	10,5±0,73
7	12,3±0,57	10,5±1,10	9,2±0,54	12,8±0,54	11,2±0,28	10,6±0,66
9	11,7±0,65	11,3±1,42	9,9±0,33	12,0±0,99	11,3±0,53	10±0,46
Rz				**Rz**		
1	63,6±1,10	54,9±0,95	50,3±1,66	52,1±0,94	50,5±0,88	48,6±0,82
3	48,0±0,98	44,2±1,37	43,2±1,22	45,3±1,55	43,7±0,82	38,5±0,82
5	44,2±1,07	41,1±0,96	40,8±0,84	54,2±0,88	51,3±0,47	48,8±2,20
7	52,45±1,00	47,2±2,09	45,2±1,43	59,0±0,51	53,6±0,97	51,3±0,72
9	54,13±1,52	50,4±2,19	48,4±1,17	53,8±0,82	48,6±0,49	47,2±1,59

N=5			
Semisphere samples			
Ra			
Zones	30 minutes of polishing	60 minutes of polishing	120 minutes of polishing
Zone	Average ± S.D.	Average ± S.D.	Average ± S.D.
3	6,9 ± 0,52	6,2 ± 0,45	5,2 ± 0,32
5	8,1 ± 0,89	7,7 ± 0,80	6,8 ± 1,04
7	8,7 ± 1,29	7,5 ± 0,64	6,2 ± 0,40
Rq			
3	8,6 ± 0,57	8,4 ± 0,72	8,2 ± 0,41
5	10,8 ± 0,54	10,2 ± 0,64	9,5 ± 0,48
7	11,1 ± 0,42	10,5 ± 0,26	8,3 ± 0,78
Rz			
3	41,7 ± 2,32	40,6 ± 1,18	39,8 ± 1,50
5	55,3 ± 1,60	55,0 ± 2,11	53,5 ± 1,95
7	55,0 ± 0,58	54,1 ± 0,44	53,4 ± 1,20

Surface roughness data after dry electropolishing followed by chemical polishing

	After 5 minutes of chemical polishing			After 10 minutes of chemical polishing			After 20 minutes of chemical polishing		
	Ra	**Rq**	**Rz**	**Ra**	**Rq**	**Rz**	**Ra**	**Rq**	**Rz**
Samples	**Zone 3**			**Zone 3**			**Zone 3**		
V	8,0±0,35	8,2±2,17	36,6±0,45	4,7±0,40	5,9±0,98	26,0±1,03	3,4±0,86	4,1±0,56	16,2±1,04
H	6,5±0,31	8,3±0,62	37,0±0,82	6,1±0,85	7,6±1,20	35,2±0,76	3,3±0,65	4,0±0,87	15,6±2,34
S	5,1±1,05	6,7±0,73	33,7±1,03	4,3±0,48	5,7±0,87	35,4±0,95	2,6±0,99	3,2±0,97	14,7±0,87
	Zone 5			**Zone 5**			**Zone 5**		
V	6,6±0,25	8,2±1,37	36,9±0,87	5,8±0,96	7,5±0,95	36,2±0,58	3,9±0,65	4,8±0,13	18,7±1,30
H	6,5±0,36	8,4±0,73	36,2±0,58	5,5±1,05	7,1±0,56	30,3±0,88	3,7±1,06	4,4±1,02	16,6±0,87
S	6,8±0,68	8,6±0,76	36,6±0,50	5,7±0,88	7,0±1,12	27,7±1,03	3,2±0,87	4,1±0,90	18,5±1,27
	Zone 7			**Zone 7**			**Zone 7**		
V	8,2±0,64	10,2±1,35	44,4±0,96	4,4±2,06	5,6±0,55	20,5±1,39	3,8±0,10	4,6±0,97	18,0±0,84
H	7,8±0,57	9,5±0,86	41,8±0,60	5,9±0,48	7,2±0,90	32,4±0,57	3,9±0,10	4,8±1,05	18,2±0,88
S	8,2±0,59	10,7±0,96	48,9±0,76	5,1±0,68	6,6±1,10	30,9±1,05	2,9±0,65	3,9±0,99	19,6±1,01

Appendix 4. Mass before and after chemical polishing (in grams)

Zone 3			
Before chemical polishing			
Samples	5 minutes	10 minutes	20 minutes
V	2,444	2,446	2,432
H	3,629	3,745	3,635
S	11,047	10,042	9,957
After chemical polishing			
Samples	5 minutes	10 minutes	20 minutes
V	2,345	2,236	2,047
H	3,567	3,163	2,256
S	10,857	9,711	8,573
Zone 5			
Before chemical polishing			
Samples	5 minutes	10 minutes	20 minutes
V	2,975	2,859	2,957
H	3,967	3,987	4,104
S	10,128	9,997	9,364
After chemical polishing			
Samples	5 minutes	10 minutes	20 minutes
V	2,7	2,512	2,452
H	3,654	3,61	3,632
S	9,777	9,342	8,482
Zone 7			
Before CP			
Samples	5 minutes	10 minutes	20 minutes
V	2,345	2,945	2,374
H	3,629	3,521	3,746
S	9,969	10,116	10,084
After chemical polishing			
Samples	5 minutes	10 minutes	20 minutes
V	2,011	2,254	1,685
H	3,221	2,947	2,467
S	9,427	9,235	8,894